Nanowire Solar Cells

Quiroz Monnens, Simon V.

Award date:
2023

Technical University Eindhoven

Master's Thesis

Nanowire Solar Cells

Author
Quiroz Monnens, S.V. (1237028)

Department of Applied Physics
Advanced Nanomaterials and Devices

Supervisors
dr. J.E.M. Haverkort
E.A. Bochicchio, MSc.

This thesis follows the TU/e code of scientific integrity.
Master's Environomical Pathways for Sustainable Energy Systems (SELECT, EIT Innoenergy)
August 19, 2023

Abstract

Nanowire solar cells are a promising technology for improving the efficiency and cost-effectiveness of solar cells. This thesis investigates the thermodynamic losses of nanowire solar cells and explores ways to improve their efficiency.
The first part of the thesis reviews the thermodynamics of solar cells, focusing on the four main losses: Carnot loss, photon cooling, étendue loss, and photoluminescence efficiency. It also performs a theoretical analysis of different configurations of nanowire solar cells, showing how micro lenses on top of the nanowire solar cells would theoretically change the open circuit voltage.
The second part of the thesis describes the experimental work that was carried out, including the fabrication of nanowire solar cells and the characterization of their performance. The experimental results show that the calculated external photoluminescence efficiency by measuring the open circuit voltage at different excitation powers does not match the measured photoluminescence efficiency. This suggests that there are other losses that are not accounted for in the theoretical model.
The third part of the thesis presents a bottom-up cost analysis for the large-scale production of 4-inch nanowire solar cells. The cost analysis shows that for nanowire solar cells with an efficiency of 33%, the cost per Watt is estimated to be €1.54/W with a Levelized Cost Of Energy (LCOE) of €0.1572/W.
The results of this research show that nanowire solar cells have the potential to achieve high efficiencies and be cost-effective. However, further research is needed to understand the underlying causes of the differences between the theoretical and experimental results. The thermodynamic analysis provides a deeper understanding of the fundamental losses in solar cells, which can be used to design more efficient devices. The experimental work demonstrates the potential of nanowire solar cells to achieve high efficiencies, and the cost analysis provides a preliminary roadmap for the commercialization of this technology.

List of Abbreviations

ALD - Atomic Layer Deposition

AL2O3 - Aluminium oxide

AND - Advanced Nanomaterials and Devices

Au - Gold

B - Exergy

BCB - Benzocyclobutene

BOS - Balance of System

CAPEX - Capital Expenditure

CHF3 - Fluoroform

CRP - Cleanroom Personnel

DNI - Direct Normal Irradiance

DOS - Density of States

EBL - Electron Beam Lithography

EQE - External Quantum Efficiency

GaAs - Gallium Arsenide

H3PO4 - Phosphoric Acid

HF - Hydrofluoric Acid

ICP - Inductively Coupled Plasma

InP - Indium Phosphide

IPA - Isopropyl Alcohol

ITO - Indium Tin Oxide

I-V - Current Voltage

J_{sc} - Short Circuit Current Density

J_0 - Dark Saturation Current Density

LCOE - Levelized Cost of Energy

LED - Light Emitting Diode

MIBK - Methyl Isobutyl Ketone

MOVPE - Metal-Organic Vapor Phase Epitaxy

n - Ideality Factor

NA - Numerical Aperture

N-RIE - Nitride Reactive Ion Etching

NH3 - Ammonia

NREL - National Renewable Energy Laboratory

NW - Nanowire

OPT - Oxford Instruments Plasma Technology

OPEX - Operational Expenditure

P-RIE - Polymer Reactive Ion Etching

PECVD - Plasma Enhanced Chemical Vapor Deposition

PH3 - Phosphine

POx - Phosphorus Oxide

PMMA - Polymethylmethacrylate

RIE - Reactive Ion Etching

rpm - Revolutions per Minute

R_s - Series Resistance

R_{sh} - Shunt Resistance

SEM - Scanning Electron Microscope

Si - Silicon

SiNx - Silicon Nitride

SiOx - Silicon Oxide

sr - Steradian

SRH - Shockley-Read-Hall

STC - Standard Test Conditions

T - Temperature

UPW - Ultra Pure Water

V_{oc} - Open-Circuit Voltage

V_{oc}^{rad} - Open-Circuit Voltage in Radiative Limit

$V_{oc}^{ultimate}$ - Highest Open-Circuit Voltage Possible

X - Concentration Factor

Contents

Chapter 1

Introduction

The 2030 Agenda for Sustainable Development, adopted by all United Nations Member States in 2015, provides a shared blueprint for peace and prosperity for people and the planet, now and into the future [1]. At its heart are the 17 Sustainable Development Goals (SDGs), which are an urgent call for action by all countries - developed and developing - in a global partnership. They recognize that ending poverty and other deprivations must go hand-in-hand with strategies that improve health and education, reduce inequality, and spur economic growth – all while tackling climate change and working to preserve our oceans and forests. Sustainable Energy Goal number 7 (SDG 7) states "ensure access to affordable, reliable, sustainable and modern energy for all". In the Global Roadmap for Accelerated SDG 7 ambitious goals are set for the future such as; electrifying all healthcare facilities and schools worldwide by 2030 and tripling global renewable power capacity[2].

According to the International Energy Agency (IEA) [3], solar PV's installed power capacity is poised to surpass that of coal by 2027, becoming the largest in the world, putting the technology on track with the 2030 milestones under the Net Zero Scenario. Power generation from solar PV increased by a record 270 TWh in 2022, up by 26% on 2021. Solar PV accounted for 4.5% of total global electricity generation, and it remains the third largest renewable electricity technology behind hydropower and wind. Nonetheless, the installed PV capacity almost needs to quadruple in 2030 to stay in line with the goals. This shows the expected exponential growth of solar power. To install all the required solar capacity, large plots of land need to be filled with solar panels. However, in the growing world of today, large land areas are hard and expensive to obtain and local people put up more and more resistance to solar farms (everywhere else, but not in our own backyard) [4] [5] [6]. This shows to need for higher-efficiency and cost-effective solar cells which reduce the required land area.

Standard silicon solar cells typically achieve a power conversion efficiency of around 20% [7]. The efficiency of a solar cell is directly related to the open-circuit voltage (V_{oc}) and the short-circuit current (I_{sc}). Substantial efforts have been devoted to optimizing these parameters, often placing emphasis on the latter [8]. The conversion of solar energy into electrical energy encounters limitations due to various thermodynamic processes. These processes were described in detail by William Shockley and Hans Queisser in 1961 [9]. In their work, they established that a single-junction solar cell, under typical sunlight conditions, can achieve maximum efficiency of 33.7%. When operating at this efficiency, the solar cell is said to be at the radiative limit. In this scenario, the sole loss mechanism is assumed to be radiative recombination, where thus in open circuit conditions each incident photon is also reemitted, and the solar cell acts as a Light Emitting Diode (LED). Furthermore, Shockley and Queisser also determined the ultimate limit of solar cell efficiency, which considers the four main thermodynamic losses related to the open circuit voltage. The first loss is the Carnot loss, which is analogous to the efficiency of a perfect heat engine. The second loss is the photon cooling loss, which occurs when a solar photon is absorbed by a solar cell and its energy is transferred to the cell's electrons. The electrons then lose some of their energy to the cell's lattice, which reduces the cell's open circuit voltage. The third loss is the photoluminescence efficiency, which is a measure of how much of the incident light is re-emitted by the solar cell as photons. The ideal solar cell would re-emit all of the incident light, but in practice, some of the light is lost to non-radiative recombination. Finally, there is a loss associated with the geometric shape of the incident and emitted light beams. In the ideal case, a parallel beam of light that enters a solar cell would also exit as a parallel beam. However, in reality, the light emitted from a bulk solar cell is emitted at a 4π solid angle, which

means that it diverges. This process of going from a parallel to a diverging light beam is called étendue expansion. The étendue (ε) is a measure of the geometric constraints of the light beam.

An analysis of the thermodynamical losses in a solar cell gives us better knowledge of how to increase its efficiency. The next-generation solar cells are now mainly focused to reach the ultimate efficiency. This is done by optimizing the fabrication techniques and design of the solar cell itself. The topic of nanophotonic engineering has brought some interesting designs, such as nanowire solar cells (1.1), which show promises for achieving efficiencies near the Shockley-Queisser limit more easily [10]. The geometrical shape of a nanowire ensures light emission under a more confined angle as compared to a bulk solar cell, reducing one of the thermodynamic losses by simply changing the design of the solar cell. In the last few years, a considerable amount of work has been done on optimizing the external radiative efficiency and the design itself in the hope of reaching the fundamental limit [8]. This has resulted in an Indium Phosphide (InP) nanowire solar cell with a record efficiency of 19.2% [11]. As seen from the current record a lot of improvements can still be made. To increase its efficiency even further micro lenses can be placed on top of the nanowire, focusing the light on a single nanowire as can be seen in figure 1.2. However, to optimally profit from the micro lenses the non-illuminated wires need to be removed as shown in figure 1.1. The experimental work still needs to be further improved such that the ultimate limit can be reached. The methods for fabrication are done mostly on a lab scale and are still too expensive for commercial purposes. While keeping an eye towards the future it is also important to estimate the cost of the production of the new generation solar cells, such that smart designs are not only efficiency optimized but also cost-effectively optimized. Furthermore, the thermodynamic and entropy-generating processes that reduce the V_{oc} and efficiency in nanowire solar cells are not widely understood and need to be researched further, such that a thermodynamic theory can be established around solar cells which is accepted by all.

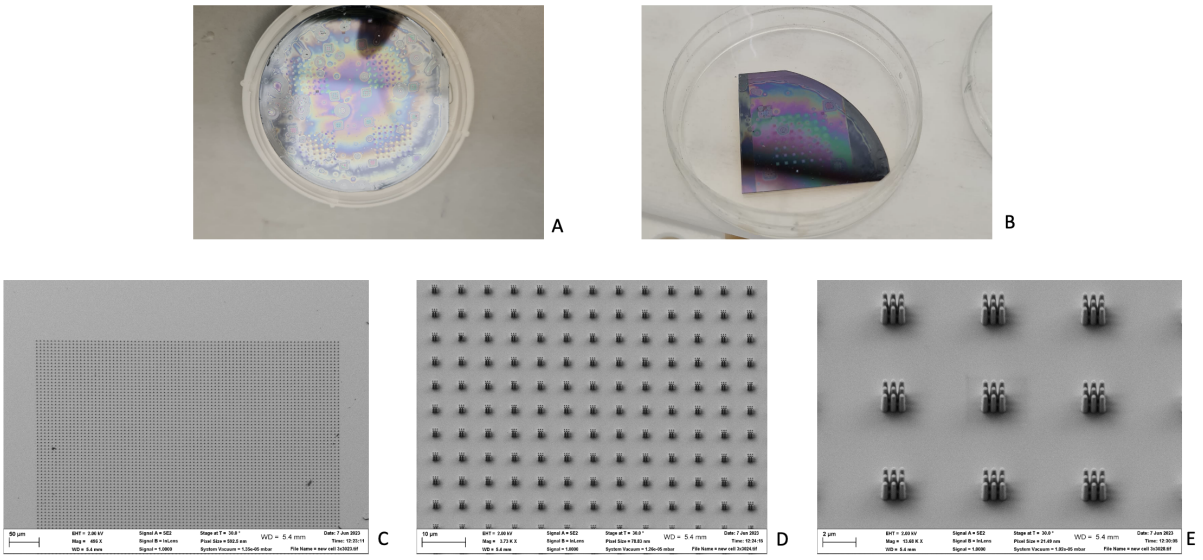

Figure 1.1: Nanowire solar cells, A) 2-inch wafer with nanowire solar cells B) quarter of 2-inch wafer with 49 cells C) Scanning Electron Microscope (SEM) picture of one cell, D) zoomed SEM picture of a cell, the groups of wires become visible E) zoomed SEM picture of a cell, the individual wires become visible.

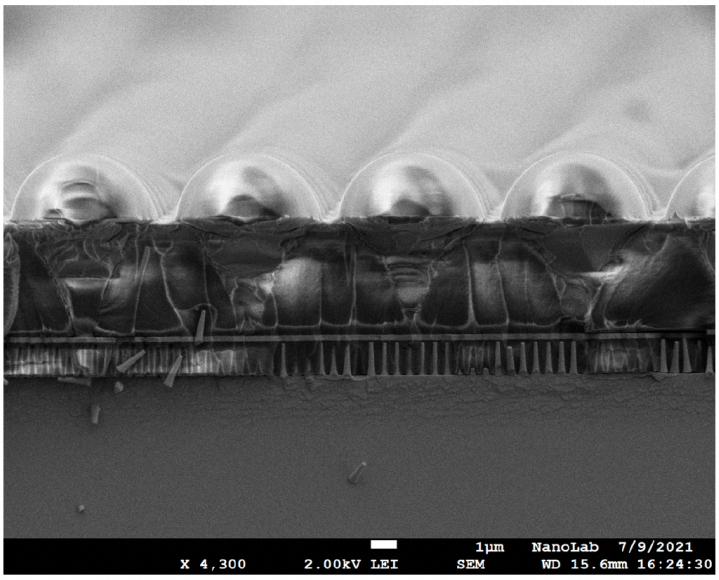

Figure 1.2: SEM picture of nanowire solar cell with microlens on top. The picture is made by a previous master's student. [12]

Outline

This thesis aims to better understand the thermodynamic losses of a solar cell. Additionally, an attempt is made to improve the open circuit voltage of nanowire solar cells by implementing micro lenses on top of nanowires while removing the non-illuminated nanowires. Moreover, the excitation dependence on various solar cell parameters is explored, with a special emphasis on photoluminescence efficiency. Furthermore, a bottom-up cost analysis is conducted, aimed at assessing the economic viability of establishing a potential fabrication facility. In Chapter 2 the relevant background theory is given, starting with the general description of a solar cell in section 2.1, followed by a general description of the open circuit voltage in section 2.2. In sections 2.3 and 2.4 the étendue expansion and photoluminescence efficiency loss terms are elaborated. In section 2.5 a theoretical description of different nanowire solar cells configurations is given. In the last section 2.6 a more in-depth thermodynamic view is given related to solar cells and their losses. In this section, a derivation is made for the loss terms and an alternative exergy description is given. The reader will still be able to understand the full report when skipping this section. In Chapter 3 the method for the experiments and fabrication is given. In section 3.2 the different manufacturing steps are summarized in the text boxes while the details and tips and tricks are given in the text outside the text boxes, the reader can skip the text outside the text box and still understand the whole fabrication method. In Chapter 4 the result of the experiments is shown. In Chapter 5 a detailed bottom-up cost analysis is given for two different production volumes of nanowire solar cells, note that here a different fabrication method is used than described in section 3.2. Finally, in Chapter 6 the main findings and conclusions are summarized and an outlook for further optimization and research is given.

Chapter 2

Theoretical Background

2.1 Solar Cell

The sun irradiates approximately 1000 W/m^2 of sunlight on the earth's surface. This energy could be used to solve the world's energy problems. To convert the photon energy into useful electrical energy in a solar cell the photovoltaic effect is used. Solar cells are made from semiconductor material, where Silicon (Si) is the most used due to its abundance, favorable bandgap, and long lifetime. However, also other semiconductor materials are used to produce solar cells, such as Indium Phosphide (InP) and Gallium Arsenide (GaAs), both III/V semiconductors. Due to their direct bandgap large absorption probabilities are observed, which allows for thinner solar cells. Another benefit is their slightly larger bandgap giving them a theoretically higher efficiency than Si-solar cells. However, due to the higher cost of III/V materials, they have not yet been able to enter the solar cell market. Currently, extensive research is focused on fourth-generation solar cells with these expensive materials, which aim to enhance solar cell efficiency through intelligent engineering and innovative designs.

2.1.1 P-N junction

The main components of a solar cell are the negatively doped semiconductor (emitter) and the positively doped semiconductor (base), which are stacked on top of each other to form the device. This configuration creates a built-in potential due to the difference in doping levels, leading to the formation of a depletion region. When a photon with sufficient energy is absorbed within the depletion region, it generates an electron-hole pair. The built-in electric field then causes the electron and hole to separate and move in opposite directions. The electron migrates to the front contact of the cell, while the hole travels to the back contact, where it can flow through the load and perform work 2.1.

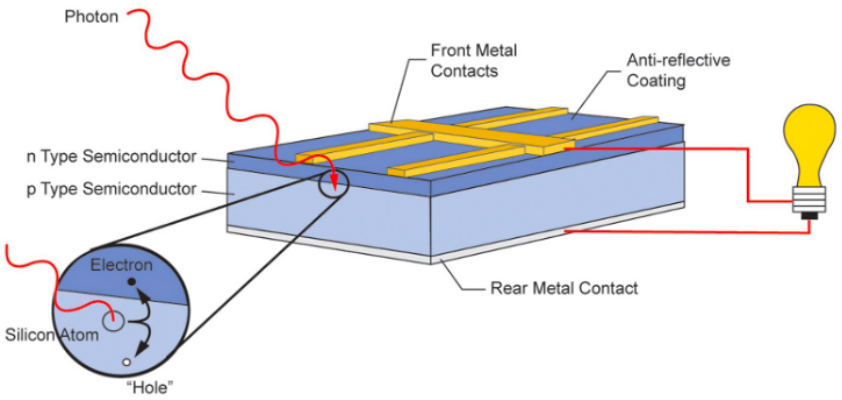

Figure 2.1: Schematic representation of a conventional silicon solar cell, showcasing the distinct components. The top contact is highlighted in yellow, the emitter in dark blue, the base in light blue, and the bottom contact in white. The critical interface between the emitter and the base is referred to as the p-n junction, effectively segregating the charge carriers.[13]

The working mechanism of a solar cell can be described by considering the p-n junction 2.2, which

exhibits a built-in electric field. This field allows current to flow in one direction, functioning as a diode. The solar cell can be represented schematically as a current source with a parallel diode (p-n junction), parallel resistance (shunt resistance), and series resistance. This representation captures the essential characteristics of the solar cell's behavior. In figure 2.2, the potential barrier for the charge carrier is shown as qV_{bi}, which is the sum of the two differences between the intrinsic fermi and the quasi fermi levels in the p- and n-type region, which are indicated as $q\Phi_{Fp}$ and $q\Phi_{Fn}$
Under normal operating conditions, without light, the p-n junction is in a state of equilibrium. The p-type region has a higher concentration of holes, while the n-type region has a higher concentration of electrons, resulting in the formation of a depletion region with a built-in electric field. When sunlight, composed of photons, illuminates the solar cell, the absorbed photons transfer their energy to the electrons, enabling them to undergo an interband transition. In the higher energy conduction band, the electrons are free to move and are pushed toward the n region and the hole towards the p region due to the built-in electric field. The charge carriers also diffuse across the P-N junction due to a concentration gradient however, this opposing field is small under 1 sun illumination.
To extract the generated charges and convert them into useful electrical current, metal contacts are placed on the top and bottom of the solar cell. These contacts facilitate the collection of electrons from the n-side and the collection of holes from the p-side. The flow of electrons and holes through an external circuit constitutes the electrical current, which can be utilized to power electronic devices or stored for later use.

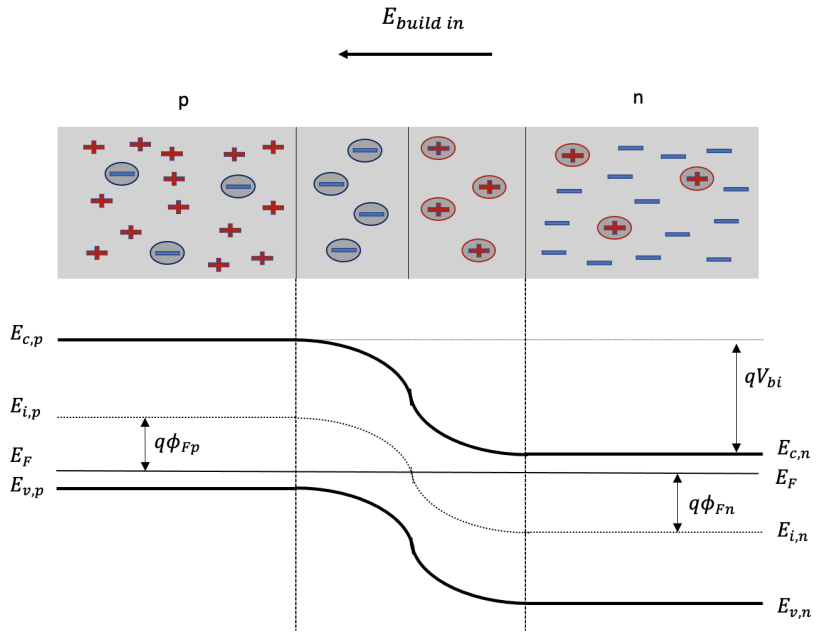

Figure 2.2: Schematic picture of the P-N junction in a solar cell under illumination.

In summary, the P-N junction in a solar cell plays a vital role in the device's operation. It establishes a built-in electric field that separates the generated electron-hole pairs, allowing for the collection of charges and the conversion of sunlight into electrical energy. Metal contacts enable the extraction of electrons and holes, enabling the flow of current and the utilization of solar energy.

2.1.2 Current-Voltage Characteristics and Efficiency

A solar cell can be represented as an electrical circuit comprising a current source, a parallel diode, a parallel resistance, and a series resistance 2.3. The current source represents the diffusion current of the photogenerated charge carriers, the diode symbolizes the p-n junction, and the two resistances represent the shunt and series resistance. The current flowing across the p-n junction follows Shockley's ideal diode equation[14].
The photogenerated current, denoted as I_{ph}, is weakly dependent on voltage and temperature, but for the purposes of this thesis, it can be assumed negligible[15]. The current through the diode is expressed by Shockley's ideal diode equation:

$$I_D = I_0(e^{\frac{qV}{k_b T}} - 1)$$

Here, I_0 represents the dark saturation current, k_b is the Boltzmann constant, q represents the charge of an electron, T denotes the temperature, and V represents the voltage across the diode. The term I_0 accounts for the diode's leakage current in the absence of light and can be measured to assess recombination within the solar cell. It is influenced by temperature, various recombination mechanisms, and material properties, although it is typically considered constant[16].

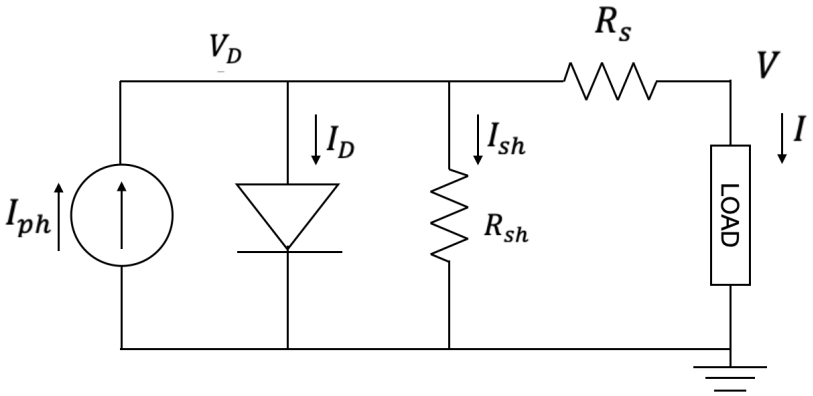

Figure 2.3: Equivalent electrical circuit of a solar cell. The single diode model.

The current for a cell under illumination is given by equation 2.1 (ignoring the series and shunt resistance for now).

$$I = I_{ph} - I_D = I_{ph} - I_0(e^{\frac{qV}{k_b T}} - 1) \tag{2.1}$$

With I_{ph} the light-generated current. The open circuit voltage (V_{oc}) and the short circuit current (I_{sc}) can be extracted from equation 2.1 by setting $I = I_{sc}, V = 0 \rightarrow I_{sc} = I_{ph}$ and $I = 0, V = V_{oc} \rightarrow V_{oc} = \frac{k_b T}{q} ln(\frac{I_{sc}}{I_0} + 1)$.
The characteristic I-V curve can be obtained by applying a voltage over an illuminated solar cell and measuring the current it supplies. It is common to simplify the equation (due to exp $\frac{qV}{k_b T} \gg 1$) which gives:

$$I = I_D - I_0 e^{\frac{qV}{k_b T}}$$

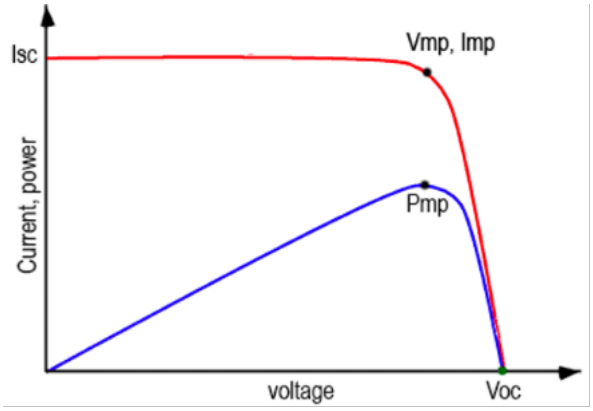

Figure 2.4: The figure illustrates the current-voltage curve (red) and power-voltage curve (blue) of a solar cell, indicating key parameters such as the Point of Maximum Power (PMP), voltage of maximum power (Vmp), current of maximum power (Imp), open-circuit voltage (Voc), and short-circuit current (Isc).

The power output is given by multiplying the voltage with the current. The squareness of the I-V curves gives an indication of the efficiency of the solar cell. As can be seen from figure 2.4 the I-V curve is not perfectly square, which means that the solar cell cannot operate at the V_{oc} and I_{sc} at the same time. The

deviation from the theoretical maximum power comes from the resistances, recombination, and leakage current in the cell circuit. The fill factor (FF) is a measure of the squareness of the graph and is given by.

$$FF = \frac{V_{mpp} I_{mpp}}{V_{oc} I_{sc}}$$

With V_{mpp} the voltage at the maximum power point and I_{mpp} the current at the maximum power point. Which gives the maximum power output as.

$$P_{out}^{max} = V_{oc} I_{sc} FF$$

The efficiency of the solar cell is given by.

$$\eta = \frac{P_{out}^{max}}{P_{in}}$$

With P_{in} the total solar energy on the solar cell surface. The solar spectrum resembles a blackbody spectrum at a temperature of $5778K$. It is common in test conditions to use $P_{in} = 1000W/m^2$ under AM1.5G conditions AM1.5 stands for Air Mass coefficient of 1.5 which corresponds to a light path through 1.5 times the thickness of the atmosphere. As the light travels through the atmosphere certain wavelengths are absorbed, mainly by O_2, H_2O, CO_2, and O_3 molecules. The longer the light path the more of these specific wavelengths are absorbed. The effect of the atmosphere on the incident solar light can be seen in figure 2.5.

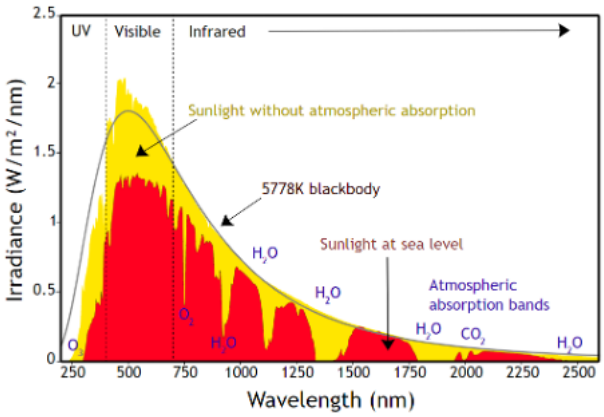

Figure 2.5: The solar spectrum before it enters the atmosphere is depicted in yellow and the spectrum incident on the solar cell, modified by the absorption of molecules in the atmosphere is shown in red.

2.1.3 Diode Model

The most basic diode model can be seen in figure 2.3. Here the total current loss I_{loss} due to the resistances can be expressed by.

$$I_{loss} = \frac{V}{R_{sh}} + \frac{IR_s}{R_{sh}}$$

where the first term represents parallel losses or alternative pathways for the current (e.g. non-radiative recombination at defects [17],[15],[18]) and the second term contains series losses due to electrical resistance of the solar cell. With R_s the series resistance and R_{sh} the shunt resistance. Considering the resistances the total current can be expressed as.

$$I = I_{ph} - I_D - I_{loss} = I_{ph} - I_0(e^{\frac{q(V+IR_s}{k_b T}} - 1) - \frac{V + IR_s}{R_{sh}}$$

An increase in R_s or a decrease in R_{sh} results in a decrease in net current and/or voltage, this is visualized by figure 2.6.

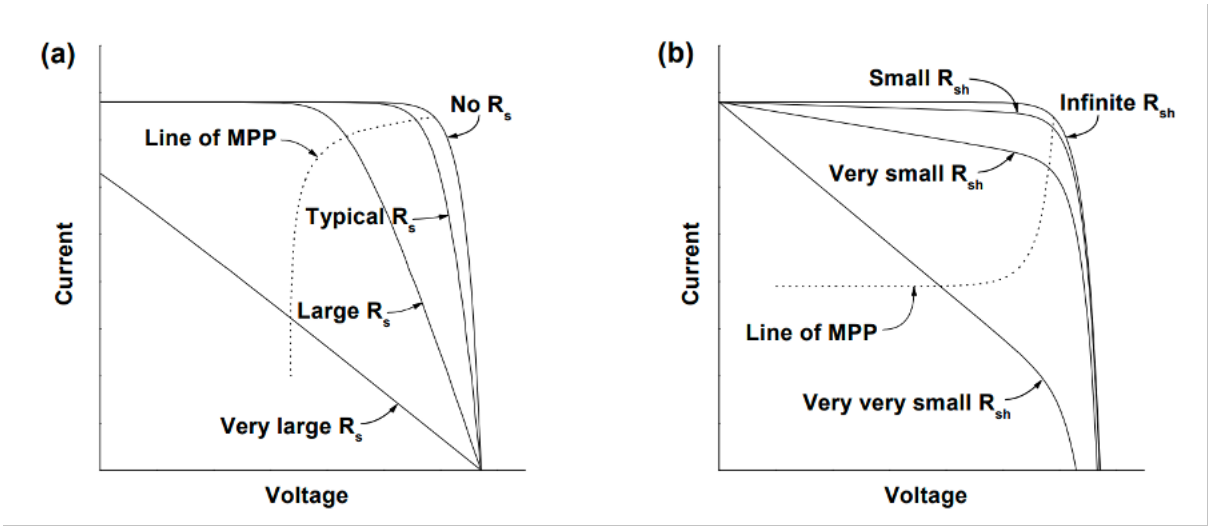

Figure 2.6: IV-curves illustrating the effect of a) series resistance (R_s) and b) shunt resistance (R_{sh}) on the solar cell performance.

In the low current situation, the electrons will flow in the lowest resistance path, however, when the illumination intensity increases the charge carriers will fill up the low resistance path and increase the losses of the solar cell. Local charge densities can vary due to defects, recombination, and local resistances. The charge built-up induces a potential gradient, which promotes lateral movement of the charge carriers across the base material, thus redistributing them as they reach the p-n junction. The redistribution will reduce the resistance felt by the charge carriers however, it makes the path taken by the charge carriers longer which leads to more recombination. In bulk solar cells the series resistance reduction out weights the series resistance increase, thus lowering the overall series resistance [19]. The shunt resistance accounts for the leakage of charge carriers when they are not injected out of the p-n junction. The leakage can occur due to defects in the p-n junction, and around heavily doped junctions, where they can tunnel from one side to the other [18][19].
The current through the diode represents the losses due to diffusion and recombination in the quasi-neutral regions of the diode, as well as the Shockley-Read-Hall (SRH) recombination in the n- and p-doped regions at low injection levels [20][21].
Until now the diode is assumed to be a perfect diode where recombination occurs via minority carrier limited band-to-band recombination or SRH recombination, however, a diode is not perfect. To also account for second-order effects (e.g. surface recombination or SRH recombination in the depletion region at high carrier injection) an ideality factor is included in the diode equation.

$$I_D = I_0(e^{\frac{q(V+IR_s)}{k_b T n}} - 1)$$

With $1 \leq n \leq 2$, however, it is common to separate the exponents into two distinct diodes giving rise to the two-diode model. Where the total current can be calculated with 2.2. In figure 2.7, the equivalent circuit is shown.

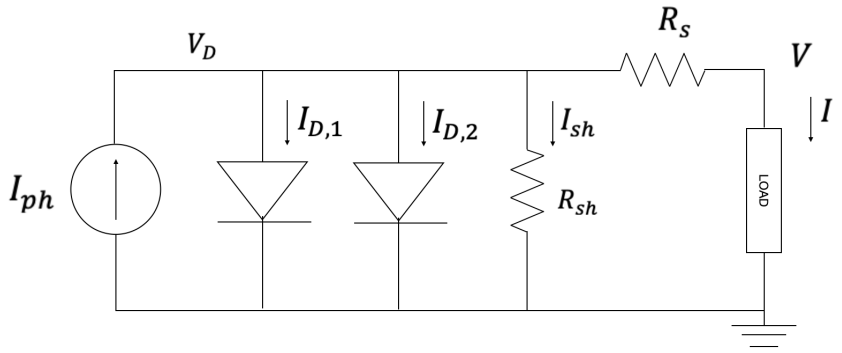

Figure 2.7: Electrical circuit of the two diode solar cell model.

$$I = I_{ph} - I_{0,1}(e^{\frac{q(V+IR_s)}{k_bTn_1}} - 1) - I_{0,2}(e^{\frac{q(V+IR_s)}{k_bTn_2}} - 1) - \frac{V + IR_s}{R_{sh}} \tag{2.2}$$

The parameters I_{ph}, $I_{0,1}$, $I_{0,2}$, n_1, n_2, R_s, and R_{sh} are unknown and can be determined using various parameter estimation methods [22][23]. Typically, n_1 is set to 1 and n_2 is set to 2 to represent ideal diodes. The resistances R_{sh} and R_s, as well as the dark saturation currents $I_{0,1}$ and $I_{0,2}$, can be estimated using one of these methods.
The photocurrent I_{ph} can then be calculated using the equation:

$$I_{ph} = (I_{c,stc} + K_i\Delta T)\frac{G}{G_{stc}}$$

where $I_{sc,stc}$ is the short-circuit current at standard test conditions (STC), K_i is the short-circuit temperature coefficient, G is the solar irradiance, and G_{STC} is the solar irradiance at STC.
There are various methods and variations available for parameter estimation, as described in references [18][20][24]
The two-diode model can easily be expanded to the three-diode model by including another diode. The third diode accounts for additional recombination effects such as recombination in the defect regions, on grain sites, and other defects in the solar cells [20][25]. Steingrube et al. [26] showed that non-linear shunt paths originated from disturbed regions with high defect concentrations. This would add an additional diode with an ideality factor of $n_3 > 2$. The total current of the three-diode model can be calculated with.

$$I = I_{ph} - I_{0,1}(e^{\frac{q(V+IR_s)}{k_bTn_1}} - 1) - I_{0,2}(e^{\frac{q(V+IR_s)}{k_bTn_2}} - 1) - I_{0,3}(e^{\frac{q(V+IR_s)}{k_bTn_3}} - 1) - \frac{V + IR_s}{R_{sh}}$$

However, the addition of the third diode is for most applications unnecessary and will only make the model more complicated.

2.2 Open Circuit Voltage

In most research on solar cells, the short circuit current is optimized, however, the open circuit voltage plays also a crucial role in the efficiency of a solar cell. The V_{oc} is directly related to the extractable work per converted photon. To optimize the efficiency the V_{oc} needs to be maximized. Shockley and Queisser showed by use of the detailed balance and Kirchhoff's radiation law that the V_{oc} in the radiative limit is determined by 2.3 [9].

$$V_{oc}^{rad} = \frac{k_bT}{q}\ln\frac{R_{sun}}{R_{blackbody}} = \frac{k_bT}{q}\ln\frac{\varepsilon_{in}\int a(E)\phi_{sun}(T,E)dE}{\varepsilon_{out}\int a(E)\phi_{blackbody}(T,E)dE} \approx \frac{k_bT}{q}\ln\frac{J_{sc}}{J_0} \tag{2.3}$$

With V_{oc}^{rad} the open circuit voltage in the radiative limit (when all incident photons are also reemitted), R_{sun} the solar generation rate, $R_{blackbody}$ the blackbody generation rate due to thermal radiation, $a(E)$ the dimensionless absorbance for a photon with energy E, $\phi(T,E)$ the photon flux per unit area of the sun or emitted by the solar cell at temperature T, J_0 the black body recombination current and, ε the étendue of the incoming or emitted light, which characterizes how "spread out" the light beam is in area and angle. This equation shows that the V_{oc}^{rad} is increased when the short circuit current J_{sc} increases with a constant black body recombination current J_0 and, that under open-circuit conditions, a perfect solar cell should function as a perfect LED when we have $R_{sun} = R_{ext}$ where R_{ext} is the external radiative generation rate. Every charge carrier photo-generated or injected should also be emitted. Unfortunately, this process is not without loss. A measure of absorption is the External Quantum Efficiency (EQE) 2.4, while the emitted photons are measured with the external radiative efficiency 2.5.

$$EQE = \frac{I_{generated}}{\phi_{sun}(T,E)} \tag{2.4}$$

$$\eta_{ext}^{PL} = \frac{R_{ext}}{R_{ext} + R_{n,rad}} \tag{2.5}$$

Where $I_{generated}$ is the total number of photo-generated electrons, R_{ext} and $R_{n,rad}$ are the external radiative emission rate and the non-radiative recombination rate, respectively. To improve the V_{oc} the external photoluminescence efficiency needs to be maximized. As can be seen in figure 2.8 many solar cells in the literature are suffering from a low external radiative efficiency.

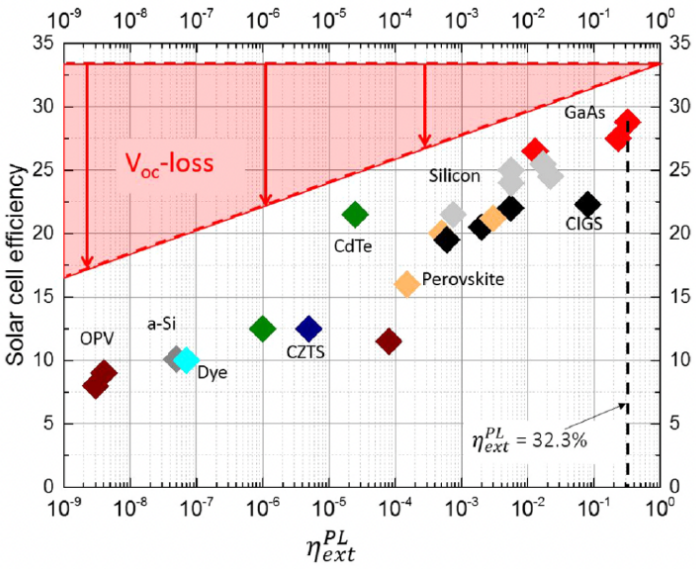

Figure 2.8: Plot of energy conversion efficiency as a function of external radiative efficiency (η_{ext}^{PL}), with the red triangle indicating losses in efficiency attributed to the open-circuit voltage (V_{oc}) calculated with 2.7.

2.5 can be rewritten in terms of radiative and non-radiative recombination lifetimes. The efficiency for the external emission of internally generated photoluminescence, η_{ext}^{PL} can be separated into the internal radiative efficiency η_{int}^{PL} and an angle-averaged light extraction efficiency, $\overline{P_{esc}}$ [27][28].

$$\eta_{ext}^{PL} = \frac{\eta_{int}^{PL}\overline{P_{esc}}}{1-\eta_{int}^{PL}(1-\overline{P_{esc}})} \approx \eta_{int}^{PL}\overline{P_{esc}} = \frac{\tau_{rad}^{-1}}{\tau_{rad}^{-1}+\tau_{nrad}^{-1}} \tag{2.6}$$

The radiative and nonradiative recombination lifetimes are denoted by τ_{rad} and τ_{nrad}^{-1}, respectively. It is worth mentioning that a previous master's student did extensive research on the angle-averaged light extraction efficiency related to the tapering angle of the nanowires [29].
The voltage over each nanowire is identical due to the parallel arrangement of the nanowires. The V_{oc} can also be calculated using a different approach using reciprocity. According to Ross et. al. [30] the V_{oc} can be calculated with equation 2.7. Where equation 2.3 is used and the term $\frac{k_bT}{q}\ln\left(\frac{\varepsilon_{in}}{\varepsilon_{out}}\right)$ is factored out. From this, we see that it directly converts to equation 2.7, where thermodynamic losses are subtracted from the ultimate voltage.

$$V_{oc} = V_{oc}^{ultimate} - \left|\frac{k_bT}{q}\ln\frac{\varepsilon_{in}}{\varepsilon_{out}}\right| - \left|\frac{k_bT}{q}\ln\eta_{ext}^{PL}\right| = V_{oc}^{rad} - \left|\frac{k_bT}{q}\ln\eta_{ext}^{PL}\right| \tag{2.7}$$

Where $V_{oc}^{ultimate}$ is the maximum open circuit voltage, V_{oc}^{rad} is given in equation 2.3, η_{ext}^{PL} the external radiative efficiency, and ε the étendue of the incoming or outgoing beam. From this equation, it is shown that the maximum V_{oc} is obtained when the incoming étendue is the same as the outgoing, and when $\eta_{ext}^{PL} = 1$. The external radiative efficiency becomes 1 in the radiative limit when all the incoming photons are also reemitted by the solar cell. In Section 2.6, the derivation of equation 2.7 is presented using a thermodynamic approach. Here below, a brief explanation is provided.

2.2.1 Thermodynamic Losses

The losses in a solar cell can also be described from a thermodynamic point of view, which stems from the generation of entropy within the device. These losses are inevitable due to the fundamental nature of a solar cell as a thermodynamic engine composed of semiconductor material. Nevertheless, with innovative solar cell designs, it is possible to decrease or even eliminate these losses.
The losses are represented in figure 2.9

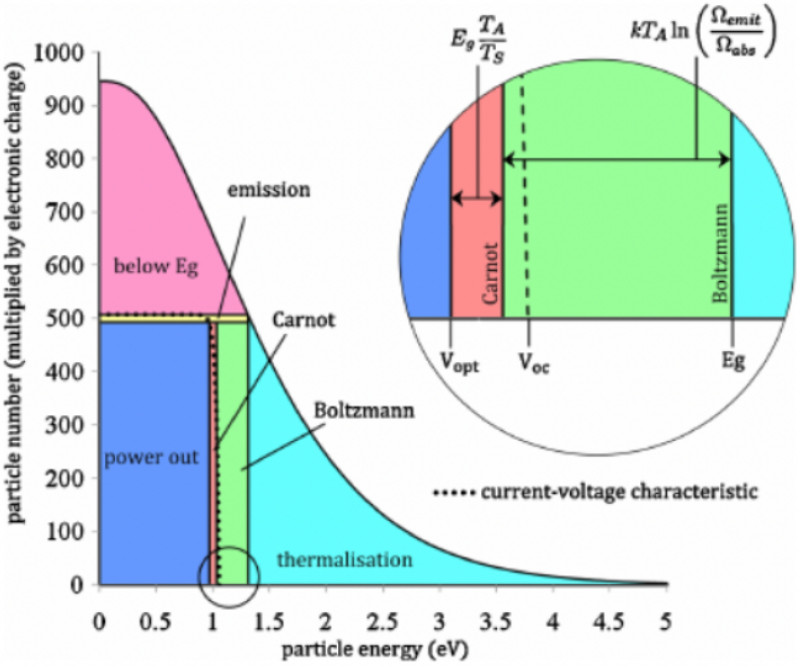

Figure 2.9: Schematic representation illustrating the intrinsic thermodynamic losses in a solar cell. The I-V curve is depicted with a dotted line, while the spectrum of the incoming solar light is represented by the black curve. The various colors in the diagram correspond to different loss mechanisms [31].

Carnot loss

A solar cell operates as a heat engine that utilizes high-quality heat from the sun as its high-temperature reservoir to produce work, while simultaneously discharging low-quality heat into a low-temperature reservoir. The Carnot efficiency determines the maximum conversion efficiency, and it is given by the expression:

$$qV_{oc} = E\left(1 - \frac{T_c}{T_s}\right)$$

where T_c represents the temperature of the solar cell and T_s represents the temperature of the sun. This equation is valid under the radiative limit for monochromatic radiation with energy $E = E_g$ [32]. The maximum theoretical energy that can be obtained is thus related to the temperature of the sun and the solar cell and the bandgap of the material used, which indirectly determines the potential. To account for the entire spectrum, the average energy per photon of the solar spectrum above the bandgap energy is considered. This leads to the Carnot limit for the open-circuit voltage, which is represented by the yellow curve in figure 2.9 and written as:

$$V_{oc}^{Carnot} = \frac{E_{sun}^{avg}}{q}\left(1 - \frac{T_c}{T_s}\right)$$

Spectral mismatch

Spectral mismatch can be categorized into two groups - photons with insufficient energy and photons with excessive energy. The conversion efficiency of solar cells significantly reduces due to photons with energy levels lower than the semiconductor bandgap, which cannot excite electrons to the conduction band and hence cannot participate in the energy conversion process. These losses are indicated by the pink area in Figure 2.9. Although these photons do not affect the open-circuit voltage (V_{oc}) of the solar cell since they are not absorbed, they limit the total number of absorbed photons, leading to a negative impact on the short-circuit current (J_{sc}) [32][33].
When electrons are excited with energy greater than the bandgap energy, they occupy higher states in the conduction band. Subsequently, they cool down to the bottom of the conduction band, a process known as thermalization and shown in cyan in figure 2.9. This irreversible process, which requires phonon assistance, results in energy conversion to heat and a subsequent decrease in the open-circuit voltage. To

mitigate these losses, a solar stack with multiple materials having different bandgaps can be used. This approach facilitates the absorption of photons with lower energy by a material with a smaller bandgap, and those with higher energy by a material with a larger bandgap, thus reducing thermalization losses. Alternatively, thermalization losses can be almost completely eliminated by using a solar stack with an infinite number of semiconductors, each with a slightly different bandgap, creating a continuous bandgap across the solar spectrum. However, there will still be a thermodynamical loss associated with the cooling of the photon gas incident from the sun to photon gas emitted by the cell. Studies have shown that the effect of thermalization on the V_{oc} is [31][34][35].

$$V_{oc}^{therm} = \frac{E_g}{q}(1 - \frac{T_c}{T_s}) + \frac{k_b T_c}{q} \ln \frac{T_s[2(k_B T_s)^2 + 2k_B T_s E_g + E_g^2]}{T_c[2(k_b T_c)^2 + 2k_B T_c E_g + E_g^2]}$$
$$\approx \frac{E_g}{q}(1 - \frac{T_c}{T_s}) + \frac{k_b T_c}{q} \ln \frac{T_s}{T_c} \tag{2.8}$$

Where T_s is the temperature of the sun and T_c is the solar cell temperature. The first term in equation 2.8 is not the Carnot limit, instead, it is a different term that incorporates both photon cooling (difference in "thermal energy" of the photons) and the Carnot limit. The second term represents a heat recovery system for the thermal energy that is rejected by the photon, the absorbed photon at temperature T_s is cooled to the solar cell temperature T_c [36]. The rejected thermal energy is absorbed by the solar cell and is transferred to the carriers. The increment of thermal energy of the carriers increases the apparent band gap due to a shift of the fermi-dirac distribution. For InP, the bandgap energy is 1.34 eV, and the approximation in the second equation is valid since $k_b T_c \gg h\nu$, and $k_b T_c$ is approximately $25mV$ [37]. This expression for the open-circuit voltage is commonly known as the ultimate limit $V_{oc}^{ultimate}$, representing the theoretical maximum V_{oc} for a single p-n junction solar cell.

Photoluminescence Efficiency

In the context of solar cells, radiative efficiency loss refers to the inefficiency in converting absorbed photons into radiative recombination at open circuit conditions. It is crucial to understand this loss and its implications in terms of entropy generation and thermodynamic considerations.
From a thermodynamic point of view, this loss can be understood as "information" loss. Minimal entropy loss at open circuit conditions is thus obtained when absorbed photons are reemitted again as photons and the system is thus reversible. When an excited electron nonradiative recombines there is an entropy loss related to the transformation of photon energy to heat. In other words, when photons are absorbed in a solar cell, they can either undergo radiative recombination, contributing to the extractable work (V_{oc}), or non-radiative processes, such as heat dissipation or non-radiative recombination, which do not fully contribute to the desired output. The external radiative efficiency (η_{ext}^{PL}) quantifies the fraction of absorbed photons that undergo radiative recombination.
The entropy generation associated with non-radiative recombination processes contributes to a decrease in the maximum extractable work and subsequently lowers the V_{oc}. To account for this loss, the entropy loss can be written in terms of potential:

$$V_{oc}^{PL} = \frac{k_b T_c}{q} \ln(\eta_{ext}^{PL})$$

It is important to emphasize that a high radiative efficiency reduces entropy generation by ensuring that a larger fraction of absorbed photons contribute to radiative recombination.
Part of this thesis aims to investigate the correlation between excitation power and radiative efficiency. To gain deeper insights into this relationship, section 2.4.1 provides an in-depth exploration of the different recombination mechanisms involved, along with an analysis of the anticipated power law relationship between these two variables 2.4.2.

Étendue expansion loss

Étendue is a measure of the geometrical characteristics of a light beam. A large, diverging beam has a larger étendue than a small, parallel beam [38]. Whereas the incoming beam has a small étendue ε_{sun}, the outgoing beam has a large étendue ε_{out}. The decrease in directional order, or the increase in directional disorder, contributes to a net entropy generation inside the solar cell, decreasing the maximum extractable work as represented in green in figure 2.9 [39][33].

This is an irreversible process, which decreases the open-circuit voltage of the solar cell according to:

$$V_{oc}^{étendue} = \frac{k_B T_c}{q} \ln\left(\frac{\varepsilon_{in}}{\varepsilon_{out}}\right)$$

where $V_{oc}^{étendue}$ is equal to the open-circuit voltage in the ultimate limit for the case of $\varepsilon_{sun} = \varepsilon_{out}$[9].
From a thermodynamic aspect, a solar cell can be considered a black-box system. As long as the étendue of the light exiting the box is the same as the étendue of the light entering the box, the étendue expansion loss is equal to zero and the details of the processes inside the box can be disregarded. However, if the light exiting the box has a larger étendue than the incoming light, a reduction in the V_{oc} will be observed. Taking all the discussed terms together, and using $V_{oc}^{max} = V_{oc}^{ultimate}$, gives the relatively well-known equation for the open-circuit voltage of the solar cell:

$$V_{oc} = \frac{E_g}{q}\left(1 - \frac{T_c}{T_s}\right) + \frac{k_B T_c}{q} \ln\left(\frac{T_s}{T_c}\right) + \frac{k_B T_c}{q} \ln\left(\frac{\varepsilon_{\text{in}}}{\varepsilon_{out}}\right) + \frac{k_B T_c}{q} \ln(\eta_{ext}^{PL}) \tag{2.9}$$

To better understand the parameters involved in the equation, the étendue and photoluminescence are explored in the next two sections, where the temperature terms are elaborated in section 2.6.2. A more in-depth thermodynamical analysis and derivation is provided in section 2.6.

2.3 Étendue

Étendue, a crucial parameter in light beams and optical systems, is a purely geometric quantity that measures the ability of an optical system or beam to gather or contain a flux of light [40]. It is determined by the product of the area A of the source or aperture emitting or collecting the light and the solid angle Ω with which the beam leaves or enters the source or aperture. To account for apertures of all shapes and sizes, this is applied to infinitesimally small elements of area δA and solid angle $\delta\Omega$. Additionally, the refractive index n of the medium and the angle of incidence between the source and the receiver of the light need to be taken into account. Hence, étendue is defined as:

$$\delta\varepsilon = n^2 cos(\theta)\delta\Omega\delta A$$

This quantity has the unit of area per steradian [38]. Thus, étendue can be increased by either increasing the area or the angular spread of the beam. A fundamental aspect of étendue is its conservation as it travels through a perfect medium or optical systems with perfect reflections or refractions. This manifests in the fact that a light beam traveling through a perfect medium undergoing refractions and reflections can be brought back to its exact original geometry using the reverse set of reflections and refractions. However, non-ideal media and optical elements that introduce scattering, absorption, and emission do not preserve étendue [38] [36].
This understanding of étendue allows us to reevaluate the limitations imposed by optics and statistical mechanics on the concentration of sunlight within a statistical framework. Considering a pencil of direct sunlight with an angular spread Ω_s incident on the entrance aperture of area A_{in}, resulting in $\varepsilon_{in} = \Omega_s A_{in}$. The concentrated light is emitted from the exit aperture within the full hemisphere, leading to $\varepsilon_{out} = \pi A_{out}$, where A_{out} is the area of the exit aperture. Assuming conservation of the number of photons and introducing the concentration ratio $X = \frac{A_{out}}{A_{in}}$, we can deduce the maximum light concentration for a conventional solar cell from $\varepsilon_{in} \leq \varepsilon_{out}$:

$$X \leq \frac{\pi}{\Omega_{sun}} \approx 46000$$

with $\Omega_{sun} = 6.85 \times 10^{-5}$ sr. For our nanowires, it has been shown that a maximal concentration ratio of 3260 is required to obtain full concentration and fully quench étendue expansion [12].
The second law of thermodynamics indicates that it is impossible to concentrate diffuse sunlight. Completely diffused sunlight is characterized by isotropic incidence, where $\varepsilon_{in} = \pi A_{in}$, and a similar argument yields $X \leq 1$. In other words, no concentration is possible. The concentration of diffuse sunlight would entail a decrease in entropy by an amount equal to $\Delta S = k_B \ln X$ [40]. However, in the present isolated optical system, where photons do not interact with other photons or any material substance, this decrease in entropy is impossible.
Nonetheless, we can introduce a concentration factor in the étendue term, resulting in a change in the étendue of the incoming ray. For example, when a lens is added to the system with an étendue ε_{lens} as in figure 2.10.

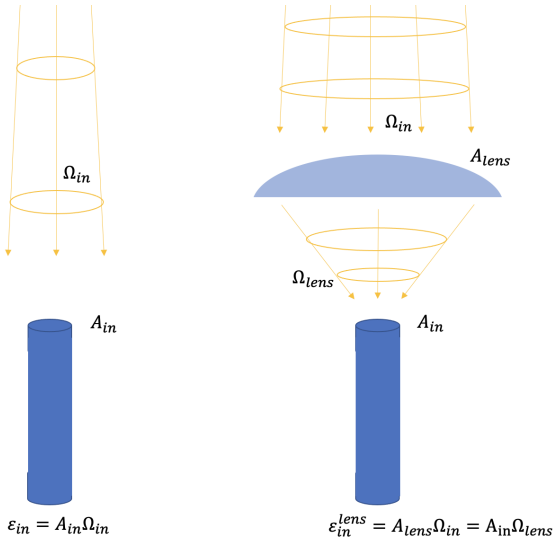

Figure 2.10: Schematic representation of the étendue, in the figure on the left solar light is incident on a nanowire on the right solar light is incident on a lens which focuses the light in a nanowire.

On the left, a nanowire solar cell is depicted which absorbs solar photons under solid angle Ω_{in} with absorption area A_{in}, giving it étendue ε_{in}. When a lens is introduced and the conservation of étendue is considered we can write:

$$\varepsilon_{in}^{lens} = A_{lens}\Omega_{in} = A_{in}\Omega_{lens}$$

Rewriting in terms of Ω_{lens}

$$\Omega_{lens} = \frac{A_{lens}}{A_{in}}\Omega_{in} = X\Omega_{in}$$

This shows that $\varepsilon_{in}^{lens} = XA_{in}\Omega_{in} = X\varepsilon_{in}$. In other words, the "effective" étendue depends on the concentration factor induced by the lens.

2.4 Photoluminescence

The V_{oc} depends on the photoluminescence efficiency as can be seen in equation 2.9. The other factors can be considered as a system constant and we can write this equation as:

$$V_{oc} = V_{oc}^{rad} - \left|\frac{k_b T}{q} \ln \eta_{ext}^{PL}\right| \tag{2.10}$$

To improve the V_{oc} clearly, we need a perfect reversible solar cell, where each incoming photon is also re-emitted ($\eta_{ext}^{PL} = 1$). To understand how the so-called radiative limit can be reached a deeper understanding of the different recombination mechanisms and their relation with excitation power is needed.

2.4.1 Recombination

Recombination processes play a vital role in determining the performance of solar cells. These processes involve the loss of charge carriers (electrons and holes) and have a significant impact on the overall efficiency of the solar cell. It is crucial to understand the different recombination mechanisms, including both radiative and non-radiative processes, in order to improve device performance and optimize solar cell designs. By gaining insights into these mechanisms, it is possible to develop strategies to minimize recombination losses and enhance the overall efficiency of solar cells.

Radiative Recombination

Radiative recombination mechanisms in semiconductor materials play a crucial role in determining the efficiency of solar cells. Unlike non-radiative recombination, radiative recombination processes involve

the emission of photons during charge carrier recombination. These mechanisms can be broadly classified into direct band-to-band radiative recombination, Donor-Acceptor Recombination, and stimulated emission, however, there are more known mechanisms. Understanding and controlling these radiative recombination mechanisms are crucial for optimizing the performance of solar cells.

Direct Band-to-Band recombination
In this mechanism, an electron and a hole directly recombine in the semiconductor's conduction and valence bands, respectively. This process occurs when the energy levels of the electron and hole match, resulting in the emission of a photon with energy equal to the bandgap. Direct radiative recombination is highly desirable in solar cells as it contributes to the efficient conversion of photon energy into potential energy.

Donor-Acceptor Recombination
This mechanism occurs when an electron and a hole recombine with the assistance of donor and acceptor states within the bandgap. Donor and acceptor states are energy levels within the bandgap caused by impurities or defects in the semiconductor material. The electron and hole are captured by these donor and acceptor states, and subsequent recombination results in photon emission with photons of lower energy than the bandgap energy. Donor-acceptor recombination is considered an inefficient process as it involves non-radiative energy losses associated with the donor and acceptor states. It is also possible to have recombination from the bottom of the conduction band or the top of the valance band with an acceptor or donor, respectively.

Stimulated Emission
Stimulated emission is a fundamental process in radiative recombination that occurs when an excited electron, occupying a higher energy level, undergoes recombination by emitting a photon due to the presence of photons with similar energy. This process is based on the principle of population inversion, where the number of electrons in the excited state is greater than the number in the ground state. When an incoming photon interacts with an excited electron, it stimulates the electron to transition to the lower energy state, emitting a photon of the same energy, phase, and direction as the stimulating photon. Stimulated emission is a key component in laser operation, where it amplifies and produces coherent light. This mechanism is expected to be small in a solar cell.

Nonradiative Recombination

The non-radiative recombination accounts for when charge carriers recombine without the emission of a photon. There are multiple non-radiative recombination mechanisms and are roughly divided into two groups, the Auger recombination, and Shockley-Read-Hall recombination. During non-radiative recombination, the excess energy is released as heat with the help of phonons.

Auger recombination
With Auger recombination three particles are involved. When a electron and a hole recombine the released energy will be transferred to a second electron, exciting it to a higher energy in the conduction band. The excited electron emits phonons to release energy and move back to the bottom of the conduction band. When there is a high carrier concentration this recombination mechanism becomes more important, due to more nearby second electrons. High carrier concentration can be achieved through high doping and high injection level (e.g. concentrated photovoltaics)[41][42][43].

Shockley-Read-Hall recombination
Shockley-Read-Hall (SRH) recombination is a non-radiative recombination process that involves electrons and holes combining through an intermediate energy state created by a defect or impurity in the crystal lattice. Phonons transfer energy during this process. SRH recombination is the primary form of recombination in solar cells. At higher injection levels, the trap states can become saturated where other recombination will take over.

Surface recombination
Surface recombination is another type of defect-related recombination that occurs at the abrupt end of a material, where defects in the crystal lattice lead to high recombination rates. Due to the locally low concentration of minority carriers caused by the high recombination rate, a current is generated towards the surface, leading to even more recombination. The rate of surface recombination is limited by the

speed at which carriers move toward the surface. Therefore, a solar cell with a high diffusion length or carrier lifetime, which are both critical for efficient carrier collection at the contacts, this can significantly increase the surface recombination velocity.
For nanowire solar cells, which have a significantly larger surface area and less average distance for the carriers to the surface, surface recombination must be prevented as it can significantly reduce the solar cell's performance. This is achieved by decreasing the number of dangling bonds through the growth of a passivation layer such as a sulfur layer, which is typically covered with a thin layer of SiO_2 to prevent sulfur degradation.
The non-radiative recombination channels, including surface recombination, are conventionally included in one external radiative efficiency factor η_{ext}^{PL}. This factor is equal to unity in the radiative limit and smaller than one when accounting for non-radiative recombination, leading to a sequential decrease in the V_{oc} with a factor of $\frac{k_b T}{q} \ln \eta_{ext}^{PL}$. η_{ext}^{PL} is also understood as the probability that an incident photon is absorbed and emitted at open-circuit conditions. Additionally, η_{ext}^{PL} is the product of the internal radiative efficiency η_{int}^{PL} and the angle-averaged light extraction efficiency P_{esc}, both of which can be individually optimized.

2.4.2 Photoluminescence Efficiency and Excitation Power

It is expected that the photoluminescence efficiency follows a power law relation with respect to the excitation power. The power law can be derived using the analysis conducted by Yoo et al. [44]. In their study of a light-emitting diode (LED), they established that the optical generation rate, G, can be expressed as the sum of the radiative recombination rate Bn^2 and the nonradiative recombination rate An:

$$G = An + Bn^2$$

With n the carriers concentration, A and B the non-radiative (Shock-Read-Hall (SRH)) and the radiative recombination (PL) coefficient, respectively. Auger recombination is neglected and is not expected to be relevant in a solar cell. Expressing the externally emitted PL-intensity I_{PL} in terms of the radiative recombination rate, we obtain:

$$I_{PL} = h\nu\overline{P_{esc}}Bn^2 \equiv b \cdot Bn^2$$

Where h is Plancks constant, ν light frequency, $\overline{P_{esc}}$ the angle average photon escape probability and, $b = h\nu\overline{P_{esc}}$ a new constant. Writing this in terms of the carrier concentration n we obtain:

$$n = \sqrt{\frac{I_{PL}}{bB}}$$

Following the paper of Yoo et al.[44], and using a generation rate G that is proportional to the solar radiation intensity I_{sun} in W/cm^2 as:

$$G = xI_{sun} = An + Bn^2$$

Where the constant x contains the reflection loss of the front surface of the cell R as well as the absorptivity a_b through $x = \frac{(1-R)a_b}{h\nu}$.
The generation rate can be written for three distinct cases, when radiative recombination is dominant, when non-radiative recombination is dominant, and an arbitrary combination of radiative and nonradiative recombination.

Case I: Radiative recombination dominant

In the radiative limit, the radiative term will be dominant indicating: $G = Bn^2 \gg An$ or in terms of I_{PL}.

$$G = xI_{sun} = B\frac{I_{PL}}{bB} \rightarrow I_{PL} = C_{PL}^{rad} I_{sun}^1$$

With $C_{PL}^{rad} = x \cdot b$. Showing a linear relation between the externally emitted PL intensity and the incoming solar radiation in the radiative limit.

Case II: Nonradiative recombination dominant

When nonradiative recombination is dominant the optical generation can be described as $G = An \gg Bn^2$. Written in terms of I_{PL} we obtain:

$$G = xI_{sun} = A\sqrt{\frac{I_{PL}}{b \cdot B}} \rightarrow I_{PL} = C_{PL}^{nrad} I_{sun}^2$$

With $C_{PL}^{nrad} = (\frac{x}{A})^2 b \cdot B$. This shows a quadratic relation between the incoming solar intensity and the PL intensity in the non-radiative limit.

Case III: Arbitrary combination of radiative and nonradiative recombination

In the arbitrary case, we observe an exponent β in the power dependence of the integrated photoluminescence intensity. The PL intensity can be expressed as

$$I_{PL} = h\nu\overline{P_{esc}} B I_{sun}^{\beta} \tag{2.11}$$

Which yields an external radiative efficiency of

$$\eta_{ext}^{PL} = \frac{I_{PL}}{I_{sun}} \propto I_{sun}^{\beta-1} \propto X^{\beta-1}$$

With $1 \leq \beta \leq 2$ and, X the light concentration. Now we can write the open circuit voltage as:

$$V_{oc}^{with-lens} = V_{oc}^{rad} - \left| \frac{k_b T}{q} \ln\left(X^{\beta-1} \eta_{ext}^{PL}\right) \right|$$

2.5 Nanowire Solar Cells

Equation 2.9 highlights several thermodynamic factors that lead to the reduction of open circuit voltage and overall efficiency in a solar cell. These losses can be mitigated through smart engineering and design strategies. There are three main loss terms: photon cooling, étendue, and photoluminescence efficiency. To minimize these losses, it is crucial to ensure that the emitted photon beam has the same temperature as the incident photon beam, the incoming étendue matches the emitted étendue, and each incident photon is emitted at open circuit conditions.
Nanowire solar cells provide an example of how some of these losses can be minimized. The distinctive feature of nanowire solar cells lies in the boundary conditions imposed on propagating waves (incoming or emitted light) due to the geometric structure of the nanowire. The electromagnetic waves inside the nanowire are no longer a superposition of plane waves but a combination of transverse modes, similar to an optical fiber. Depending on which field is in the direction of propagation these modes are called transverse electric (TE) modes, transverse magnetic (TM) modes, transverse electromagnetic (TEM) modes, or hybrid electric (HE) modes, which have the electric field, the magnetic field, or both components in the direction of propagation respectively. At open-circuit conditions, it has been shown that for the nanowires used here, approximately 68% of the emitted light will be confined into the fundamental HE11 guided mode [45]. This guided mode is already somewhat directional, decreasing the voltage loss due to more favorable étendue compared to bulk solar cells, as can be seen in figure 2.11A. and 2.11B.

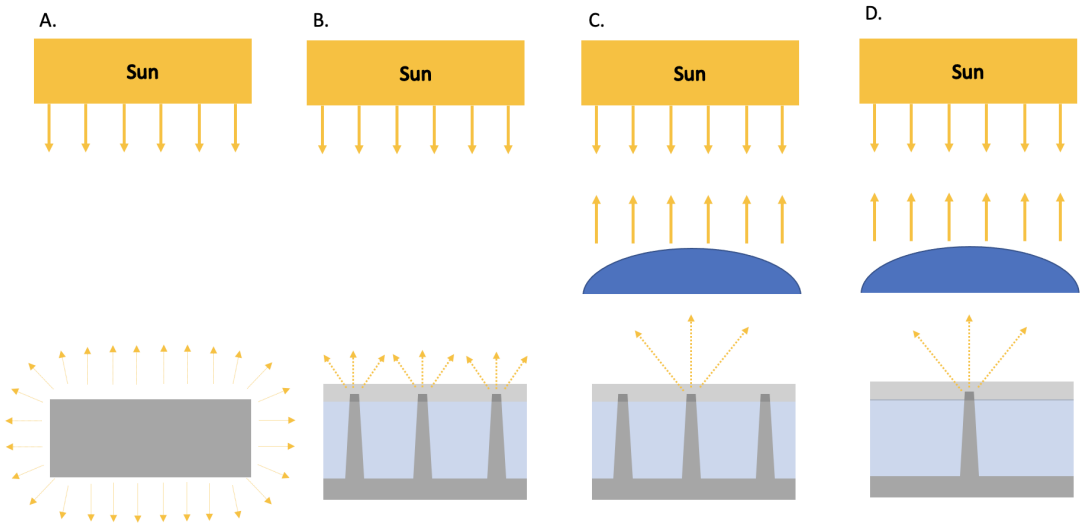

Figure 2.11: Different configurations of solar cells, where the incoming and emitted light beams are shown. A) a bulk solar cell B) a full array nanowire solar cell C) a full array nanowire solar cell with a micro lens on top D) a single nanowire solar cell with a micro lens on top.

To enhance the étendue of the system, a micro lens is introduced, as depicted in figure 2.11C. The lens serves to focus the incoming light onto a single nanowire and collimate the emitted light into a parallel beam, effectively transforming the incoming étendue (ε_{in}) to the concentrator étendue due to the lens (ε_{lens}). The configuration of the nanowire and lens can be seen as a single thermodynamic engine, converting a parallel beam of photons from the sun into a collimated output beam and an output voltage at open-circuit.
In concentrator solar cells, the typical approach involves considering an increased amount of solar illumination reaching the cell, which is proportional to the surface area of the concentrating lens. For a concentrator solar cell in the radiative limit, this leads to an increased open-circuit voltage, expressed with the help of equation 2.3 as [8]:

$$V_{oc}^{rad,conc} = \frac{k_b T}{q} \ln \frac{J_{sc}^{conc}}{J_0}$$

Let's focus on the lensed nanowire solar cell shown in figure 2.11C, where the diameter of the microlenses is chosen to be 12 times larger than the nanowire pitch, which is 500 nm in our case. This decision was made because very small microlenses with a diameter equal to the pitch of the nanowire array are not capable of effectively focusing or collimating the light due to the diffraction limit. A 500 nm diameter microlens will diffract the light in the same way as a 500 nm circular aperture. Previously published simulations have shown that a 4 µm (8 µm) diameter lens is capable of reducing the emission angle from 0.84 sr down to 0.024 sr (0.011 sr), enabling an increase in the open-circuit voltage of 139 mV (159 mV) above the radiative limit for a lossless cell [45]. These simulations emphasize the need to employ relatively large diameter lenses to reduce the effect of diffraction and to effectively collimate the emitted light.
A nanowire solar cell with a pitch of 500 nm and a surface area of 500×500 µm is made up of approximately one million individual nanowire solar cells that are connected in parallel to each other. In our nanowire solar cells with 6 µm diameter lenses on their surface, only a small fraction of the nanowires are exposed to light, as shown in figure 2.11C. We assume N nanowires below each microlens, with 1 illuminated wire and N-1 non-illuminated wires, where N approaches 144. At short-circuit conditions, the current flowing through the non-illuminated nanowires is almost zero, while the concentrated short-circuit current J_{sc}^{conc} in the illuminated nanowire is N times larger (J_{sc}^{conc}=$NJ_{sc}^{no-lens}$) due to the concentration of light. At open-circuit conditions, all wires become forward biased due to the common front and bottom contacts, which connect all nanowires electrically in parallel. The high photogenerated current in the illuminated wires will flow back through all illuminated and non-illuminated nanowire diodes to yield a net zero current as required at open-circuit. We use the equation for $V_{oc}^{rad,conc}$ to calculate the current flowing through each nanowire, with a photogenerated current of $J_{sc}^{non-illuminated} = 0$ for non-illuminated nanowires. This yields at open-circuit conditions:

$$J = J_{sc}^{conc} - NJ_0 e^{\frac{qV_{oc}^{conc}}{k_b T}} = 0$$

This can be compared to the nanowire cell without lenses:

$$J = NJ_{sc}^{no-lens} - NJ_0 e^{\frac{qV_{oc}^{no-lens}}{k_b T}} = 0$$

Using J_{sc}^{conc}=$NJ_{sc}^{no-lens}$, we can show that the addition of microlenses to an arrayed nanowire solar cell does not increase the open-circuit voltage in the radiative limit ($V_{oc}^{conc} = V_{oc}^{no-lens}$). This can be easily understood since both J_{sc} and J_0 increase with the same nano-concentration factor N. However, to benefit from the increase in open-circuit voltage, the non-illuminated nanowires need to be removed, such that J_{sc}^{conc}=$NJ_{sc}^{no-lens}$ and $NJ_0 \rightarrow J_0$, as shown in figure 2.11D. In practice, it will be hard to align the focus point of the micro lens with the top of the nanowire. To simplify the manufacturing process a 3x3 array is made in the focus point of the micro lenses instead of a single nanowire, making it easier to align the focus point with the nanowires.

2.5.1 Modeling the Nanowire Solar Cells

The three different configurations of a nanowire solar cell array are investigated here as shown in figure 2.11.
In the first situation, un-concentrated solar light is incident on a nanowire array of N_{nw} nanowires.
In the second situation, a microlens is placed on top of the same nanowire array, concentrating the solar light onto one nanowire, where the rest is non-illuminated.
In the last configuration, the non-illuminated nanowires are removed, leaving only one nanowire per microlens. To compare the different situations, it is assumed that under one micro lens the number of nanowires is equal to the light concentration $N_{nw} = X = 144$.
In order to get a better understanding of the different systems a two-diode model is made for each situation.

Nanowire Array

Each nanowire can be seen as an individual nano solar cell. The array of N_{nw} nano solar cells are put in parallel. The two-diode model becomes, therefore, an electrical circuit with N_{nw} two-diode models put in parallel as in figure 2.12.

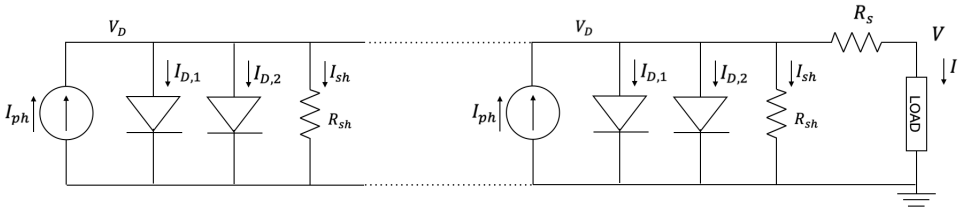

Figure 2.12: Two diode model representation of N_{nw} nanowire solar cell array in parallel.

The total current can therefore be described by.

$$\sum_{i=1}^{N_{nw}} I_{ph}^i - I_{D,1}^i(e^{\frac{q(V+IR_s)}{k_b T n_1}} - 1) - I_{D,2}^i(e^{\frac{q(V+IR_s)}{k_b T n_2}} - 1) - \frac{V + IR_s}{R_{sh}^{tot}}$$

Where R_{sh}^{tot} is the equivalent resistance over the N_{nw} nanowires which can be calculated with equation 2.12, where the simplification is made due to the identically of the nanowires. The current from each nanowire flows through the same pathway, giving the same series resistance for each nanowire which is constant and equal to R_s.

$$\frac{1}{R_{sh}^{tot}} = \sum_{i=1}^{N_{nw}} \frac{1}{R_{sh}^i} \rightarrow R_{sh}^{tot} = \frac{R_{sh}}{N_{nw}} \tag{2.12}$$

Again due to the identical nanowires and due to a large exponential term the current can be approximated by:

$$I \approx N_{nw}\left[I_{ph} - I_{D,1}e^{\frac{q(V+IR_s)}{k_b T n_1}} - I_{D,2}e^{\frac{q(V+IR_s)}{k_b T n_2}} - \frac{V + IR_s}{R_{sh}}\right]$$

This equation shows that both the current induced and the current lost due to the diode and resistances scale linearly with the number of nanowires.
The V_{oc} can be calculated with

$$V_{oc} = V_{oc}^{ultimate} - \left|\frac{k_b T}{q} \ln \frac{\varepsilon_{sun}}{\varepsilon_{nw}}\right| - \left|\frac{k_b T}{q} \ln \left(X^{\beta-1} \eta_{ext}^{PL}\right)\right| = \frac{k_b T}{q} \ln \left(\frac{J_{sc}}{J_0^{rad}}\right) - \left|\frac{k_b T}{q} \ln \eta_{ext}^{PL}\right|$$

Where ε_{nw} is the étendue of the emitted light from the nanowires and, J_0^{rad} is the dark saturation current in the radiative limit. Considering the case where we have a light concentration of $X = 1$. The emitted light has a different étendue than the incident light, indicating a change in étendue and thus a reduction in V_{oc} compared to the ultimate limit. The light is slightly concentrated due to the antenna effect of the nanowire, which absorbs an area 12x larger than the physical cross-section of the nanowire[8]. This configuration is considered our base case.

Nanowire Array with Microlens

In the second case, a lens is placed on top of the nanowire array. The incoming light is concentrated onto one single nanowire such that the top of the nanowire is at the focus point of the lens. This nanowire will generate the photocurrent I_{ph}^{con}, the rest of the nanowires will not generate any current. This system is shown in figure 2.13.

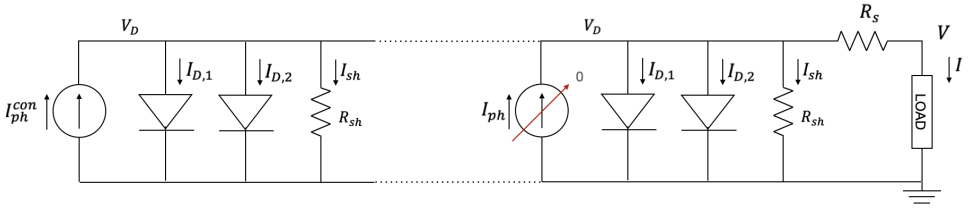

Figure 2.13: Two diode model representation of N_{nw} nanowire solar cell array in parallel, where only one nanowire is illuminated under light concentration $X = 144$.

The total current can be calculated as:

$$I \approx I_{ph}^{conc} - N\left[I_{D,1} e^{\frac{q(V+IR_s)}{k_b T n_1}} + I_{D,2} e^{\frac{q(V+IR_s)}{k_b T n_2}} + \frac{V + IR_s}{R_{sh}}\right]$$

As can be seen from the equation the total leakage current will be equal to the previous situation. Due to the light concentration, a N_{nw} times higher current is induced in a single nanowire compared to the base case($J_{ph}^{con} = J_{ph} N_{nw}$), while the current loss is similar. This result has already been shown in the previous section.
The V_{oc} can be expressed with as.

$$V_{oc} = V_{oc}^{ultimate} - \left|\frac{k_b T}{q} \ln \frac{\varepsilon_{sun}}{\varepsilon_{lens}}\right| - \left|\frac{k_b T}{q} \ln \left(X^{\beta-1} \eta_{ext}^{PL}\right)\right| = \frac{k_b T}{q} \ln \left(\frac{J_{sc}^{conc}}{N_{nw} J_0^{rad}}\right) - \left|\frac{k_b T}{q} \ln \left(X^{\beta-1} \eta_{ext}^{PL}\right)\right|$$

Where ε_{lens} is the étendue of the lens ($\varepsilon_{lens} = X\varepsilon_{nw}$), the equation is rewritten similarly as in equation 2.3. From here we see that the only gain compared with the base case is a higher photoluminescence efficiency due to higher incident light intensity. When the cell is in the radiative limit ($\eta_{ext}^{PL} = 1$) and the nonradiative recombination is saturated the two situations are similar and no difference in V_{oc} or efficiency is expected. The main difference is thus that the second situation is closer to the radiative limit and will have a higher V_{oc} and efficiency compared to the base case unless both situations are already in the radiative limit, here no difference is expected. This is already been demonstrated in [12].

3x3 Nanowire Array with Microlens

In the third situation, only one nanowire is present and is illuminated under concentrated light. This can be described by the standard two-diode model with a photogenerated current under concentrated light conditions 2.14.

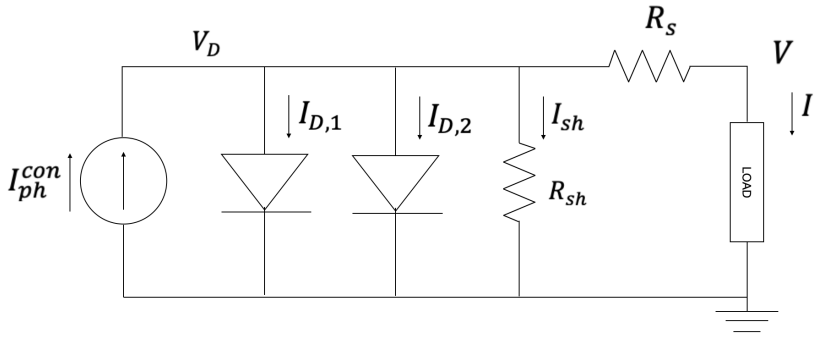

Figure 2.14: Two diode model representation of one nanowire solar cell under concentrated illumination.

The current loss is N_{nw} smaller than in the previous situations due to the lower number of nanowires. The total current can be calculated with:

$$I \approx I_{ph}^{conc} - I_{D,1}e^{\frac{q(V+IR_s)}{k_bTn_1}} - I_{D,2}e^{\frac{q(V+IR_s)}{k_bTn_2}} - \frac{V+IR_s}{R_{sh}}$$

The expression for V_{oc} is given by

$$V_{oc} = V_{oc}^{ultimate} - \left|\frac{k_bT}{q}\ln\frac{\varepsilon_{sun}}{\varepsilon_{lens}}\right| - \left|\frac{k_bT}{q}\ln\left(X^{\beta-1}\eta_{ext}^{PL}\right)\right| = \frac{k_bT}{q}\ln\left(\frac{J_{sc}^{conc}}{J_0^{rad}}\right) - \left|\frac{k_bT}{q}\ln\left(X^{\beta-1}\eta_{ext}^{PL}\right)\right|$$

This equation is similar to the second situation but with N_{nw} less dark saturation current, which indicates that the open circuit voltage is expected to increase with $\frac{k_bT}{q}\ln N_{nw}$ when the non-illuminated parallel pathways (nanowires), are removed from the circuit.
To calculate the V_{oc} increase between the different cases equation 2.13 and 2.7 are used with previously obtained values for $\beta(x)$ [12].

$$\eta_{ext}^{PL}(X) = \begin{cases} \alpha X^{\beta(X)-1}, & \text{if } X = \text{Low illumination} \sim 1 \text{ sun}, \beta(x) = 1.2 \\ \alpha X^{\beta(X)-1}, & \text{if } X = \text{High illumination} \sim 144 \text{ suns}, \beta(x) = 1.5 \end{cases} \tag{2.13}$$

Where α is an experimental constant. The V_{oc} for the different situations can be written as:

$$V_{oc} = \begin{cases} V_{oc} = V_{oc}^{rad} - \left|\frac{k_bT}{q}\ln\eta_{ext,1}^{PL}\right|, & \text{situation 1} \sim 1 \text{ sun} \\ V_{oc} = V_{oc}^{rad} - \left|\frac{k_bT}{q}\ln\eta_{ext,2}^{PL}\right|, & \text{situation 2} \sim 144 \text{ suns} \\ V_{oc} = V_{oc}^{rad,conc} - \left|\frac{k_bT}{q}\ln\eta_{ext,3}^{PL}\right|, & \text{situation 3} \sim 144 \text{ suns} \end{cases}$$

Where $V_{oc}^{rad} = \frac{k_bT}{q}\ln\left(\frac{J_{sc}}{J_0^{rad}}\right)$, $V_{oc}^{rad,conc} = \frac{k_bT}{q}\ln\left(\frac{J_{sc}^{conc}}{J_0^{rad}}\right)$ and, $\eta_{ext,2}^{PL} = \eta_{ext,3}^{PL}$.
From the equations, the expected V_{oc} loss reduction can be calculated. When comparing situations 1 and 2 we see that the difference is only in the photoluminescence efficiency term, and only present outside the radiative limit.

$$\Delta V_{oc} = \frac{k_BT}{q}\left(\ln\eta_{ext,1}^{PL} - \ln\eta_{ext,2}^{PL}\right) = \frac{k_BT}{q}\ln\left(\frac{\eta_{ext,1}^{PL}}{\eta_{ext,2}^{PL}}\right) = \frac{k_BT}{q}\ln\frac{\alpha(X_1)^{1.2-1}}{\alpha(X_2)^{1.5-1}} = \frac{k_BT}{q}\ln\frac{(X_1)^{0.2}}{(X_2)^{0.5}}$$

Filling in $\frac{k_BT}{q} = 25.69 \cdot 10^{-3}V$, $X_1 = 1$ sun and $X_2 = 144$ suns we obtain a voltage difference of $\Delta V_{oc} \approx 0.064V$. This voltage increase will change at different excitation powers until the radiative limit is reached in both situations, where no voltage difference is expected. Comparing the second situation with the third situation we see that the photoluminescence efficiency is similar, however the number of nanowires is reduced. This would lead to a voltage increase of

$$\Delta V_{oc} = V_{oc}^{rad,conc} - V_{oc}^{rad} = \frac{k_b T}{q} \ln\left(\frac{J_{sc}^{conc}}{J_0^{rad}}\right) - \frac{k_b T}{q} \ln\left(\frac{J_{sc}}{J_0^{rad}}\right) = \frac{k_b T}{q} \ln\left(\frac{N_{nw} J_{sc}}{J_{sc}}\right) = \frac{k_b T}{q} \ln\left(N_{nw}\right)$$

With $J_{sc}^{conc} = N_{nw} J_{sc}$, this gives $\Delta V_{oc} \approx 0.128V$. This analysis is assuming perfect solar cells and the calculated values here are optimistic.

2.6 Thermodynamics of a Solar Cell

In this section, a more in-depth analysis of the thermodynamics of a solar cell is given. The reader can skip this section and still read and understand the rest of the report without the knowledge described in this section.

As solar cells strive to achieve higher conversion efficiencies that approach the limits set by thermodynamics, it becomes increasingly important to deepen our understanding of the underlying principles. Without comprehending the origins of thermodynamic losses, it becomes challenging to effectively address and mitigate them. While much of the research in solar cell technology focuses on experimental fabrication, characterization, and numerical simulations, theoretical investigations into solar cells, especially regarding the thermodynamic causes of efficiency or V_{oc} losses, remain a specialized field within solar cell research. This is particularly true for complex structures like nanowire solar cells. To advance our understanding of nanowire solar cells, it is necessary to further explore the thermodynamics of solar cells.
In line with previous treatments of this subject, the methodology described by Markvart [46][47][48][40]adopts the concept of flows involving photons, excited carriers, energy, and entropy. However, in this approach, these flows are defined in a manner consistent with irreversible thermodynamics [49], considering light as a stream of photons rather than a continuous flow of energy and entropy. The general thermodynamic framework that follows is based solely on the examination of energy and entropy balance for photons transferred between the incident and emitted light beams and the absorbed photons. The approach presented in [46][47][48][40]is explained here, which takes a more direct route based on classical thermodynamics. This is made possible by formally separating the two essential aspects of solar cell operation: light absorption followed by the conversion of photons into electron-hole pairs, leading to useful work, or the emission of photons as luminescence.
The conversion process, focused on the transformation of energy, yields results that align with those found in textbooks discussing the thermodynamics of heat engines. The balance of entropy in photon absorption and emission then provides the necessary information to determine the irreversible entropy generation and available useful energy (exergy) and the resulting losses in the conversion process.
By utilizing an ideal gas model for the incident and emitted photon beams, as introduced in [46], a quantitative description of the four main voltage losses in photovoltaic conversion is achieved:

i) Inevitable entropy generation due to the kinetics of the conversion system.

ii) Entropy losses stemming from étendue expansion.

iii) Losses resulting from nonradiative recombination.

iv) Entropy generation caused by the cooling of photons from the solar radiation's temperature (T_s) to the converter's temperature (T_0).

This section focuses on the thermodynamics of the solar cell, aiming to examine the losses that occur under open circuit conditions and determine the available useful work that can be obtained. The entropy generation is calculated here by means of the permutations in a light beam. The next section explains how this is calculated for a light beam.

Defining photon gas

To facilitate the analysis of the photon gas and its impact on entropy and exergy, it is necessary to define it in a way that allows for practical evaluation. In the realm of geometrical optics, a convenient characteristic is the concept of étendue. When considering a narrow beam with an angular spread of $\delta\Omega$ passing through an area element δA, the étendue element is defined as:

$$\delta\varepsilon = n^2 \delta A \delta\Omega cos\theta$$

Geometrical optics provides a valuable perspective for describing light, but further refinements are required to extend its applicability to encompass wave-like propagation. This extension enables the consideration of light as propagating in individual quantum states, rather than as an infinite continuum. A useful analogy that aids our understanding is the parallel between the diffraction limit of geometrical optics and Heisenberg's uncertainty principle.
For instance, let's examine a narrow beam of light passing through a slit of width δx that defines its extent in coordinate space. In the limit of geometrical optics, where diffraction is negligible, there is a constraint on the spread of this beam in k-space, given by:

$$\delta x \delta k_x \geq 1$$

This relationship draws an analogy with particle mechanics by invoking de Broglie's wave-particle duality, which relates wave vector (k) to particle momentum (p) through $p = hk$. Multiplying by Planck's constant (h), we find that this corresponds to the limit:

$$\delta x \delta p_x \geq h$$

In other words, the Heisenberg uncertainty principle. When applied to the six-dimensional phase space of variables x, y, z, p_x, p_y, p_z, the uncertainty relation reveals that only one quantum state can occupy the volume $\delta x \delta y \delta z \delta p_x \delta p_y \delta p_z$.
A similar line of reasoning can be employed to determine the volume of a quantum state in the phase space of rays within geometrical optics. By transforming the étendue element into a suitable form, the outcome becomes immediately apparent. Choosing an appropriate coordinate system, the beam area δA becomes $\delta x \delta y$, where δx and δy represent small increments of the coordinates x and y. Likewise, the corresponding projection of the angular spread corresponds to increments δk_x and δk_y in the components of the wave vector transverse to the direction of propagation. The étendue element can then be expressed as:

$$\delta\varepsilon = \frac{n^2}{k^2} \delta x \delta y \delta k_x \delta k_y$$

Consequently, the volume element $\delta x \delta y \delta k_x \delta k_y$ in the phase space of variables x, y, k_x, k_y is equal to $\frac{k^2 \delta\varepsilon}{n^2}$ and cannot be smaller than unity. Therefore, we can assert that $\frac{k^2 \delta\varepsilon}{n^2}$ represents a single quantum state available for occupancy by photons within the beam.
We are now just a small step away from introducing statistical concepts into geometrical optics.

$$\frac{2k^2}{n^2}\varepsilon = \frac{2\nu^2}{c^2}\varepsilon \tag{2.14}$$

Accounting for two directions of polarization, the integrated quantity can be interpreted as the number of quantum states within a beam with frequency $\nu = \frac{ck}{n}$ and étendue ε. As the wave vector remains constant, the volume of a beam in the phase space of its transverse coordinates remains unchanged during its propagation in a clear, transparent medium. We can thus write a single quantum state available for occupancy by photons within a beam as 2.14

2.6.1 Solar Cell as a Heat Engine

The energy conversion process in a solar cell can be divided into two distinct parts: the absorption and emission of incident radiation, and the conversion of absorbed photons into useful work.
The energy diagram for each absorbed photon of incident radiation, which is converted into useful energy w, is illustrated in figure 2.15A. The incident photon energy u_{in} is analogously depicted as heat absorbed by the cells from a high-temperature reservoir at temperature T_{S}. During the conversion process, heat q_{w} is rejected into a low-temperature reservoir at temperature T_0, which in this case is assumed to be the temperature of the environment. Applying the conservation of energy gives.

$$u_{in} = w + q_w \tag{2.15}$$

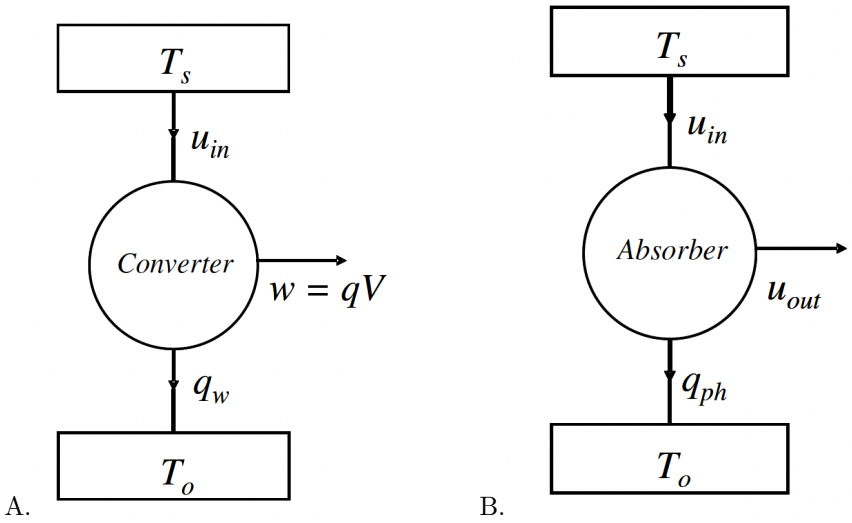

Figure 2.15: Energy flow in a solar cell. A)Energy balance for a photovoltaic converter. B)Energy balance for the absorption and emission of radiation [46].

The conversion process is also subject to an entropy balance. Let s_{in} denote the entropy of the absorbed photon. The entropy emitted into the low-temperature reservoir is $\frac{q_w}{T_0}$, and since there is no entropy associated with the work w, the energy and entropy balance equations can be expressed in the simplified form.

$$s_{in} = \frac{q_w}{T_0} - \sigma_i \tag{2.16}$$

where σ_{i} represents the entropy generated in the conversion process. According to the second law of thermodynamics, $\sigma_{\text{i}} \geq 0$.
In this treatment, the incident photons are regarded as pure heat at temperature T_{S}, leading to $s_{\text{in}} = \frac{u_{\text{in}}}{T_{\text{S}}}$. In the present approach, the absorption and emission of photons are considered as the addition or removal of a photon from the incident/emitted beams. This energy transfer is described uniformly by the expression $u = \mu + T_{\text{S}}$, where μ represents the chemical potential. This expression is also consistent with flux definitions in the framework of irreversible thermodynamics [46]. As we consider the incident flux in the form of direct sunlight, well approximated by black body radiation, we can set $\mu = 0$, and the equation for s_{in} follows accordingly (black body radiation has zero chemical potential due to an unconserved number of photons in a closed system). It is evident that the work w per photon carried out is equal to qV, where q is the charge of an electron, and V is the voltage generated by the solar cell.
Combining equation 2.15 with equation 2.16 and using $s_{\text{in}} = \frac{u_{\text{in}}}{T_{\text{S}}}$, the equations can be rewritten in terms of qV and yields:

$$w = qV = (1 - \frac{T_0}{T_s})u_{in} - T_0\sigma_i \tag{2.17}$$

Hence, the solar cell voltage can be expressed in a standard thermodynamic form, representing the amount of work that can be produced between two reservoirs at temperatures T_{S} and T_0 by extracting energy u_{in} per photon from the high-temperature reservoir, and additional entropy loss terms (σ_i) due to energy conversion. The equation gives the maximal obtainable work of a photon, which is now modeled as pure heat entering a heat engine with additional entropic energy losses due to the conversion process.

Entropy Generation

Beyond the short circuit condition, the solar cell not only absorbs photons but also emits them. We will now examine the energy and entropy balance of the absorption/emission process (2.15B). The absorption of a photon contributes energy u_{in}. Each emitted photon carries energy u_{out}, and during each absorption/emission event, heat q_{ph} is dissipated into the low-temperature reservoir. Considering that the absorbed and emitted photons carry entropy s_{in} and s_{out} respectively, and that the entropy associated with the emission of heat q_{ph} is $\frac{q_{\text{ph}}}{T_0}$, we can establish the following energy and entropy balance for the absorption/emission process:

$$u_{in} = u_{out} + q_{ph}$$

$$s_{in} = s_{out} + \frac{q_{ph}}{T_0} - \sigma_i$$

The entropic energy loss or exergy loss per photon can be written as:

$$T_0\sigma_i = (u_{in} - u_{out}) - T_0(s_{in} - s_{out}) \tag{2.18}$$

The entropy generation resembles the difference of "availability" between the incident and emitted photons for a process which takes place at constant volume. By substituting 2.18 into 2.17 and using $s_{\text{in}} = \frac{u_{\text{in}}}{T_S}$, we obtain $qV = u_{\text{out}} - T_0 s_{\text{out}} = \mu_{\text{out}}$. In other words, the work achieved through the conversion of a photon into electrostatic or chemical energy is equal to the chemical potential of the emitted photons. This result, well-established in the theory of p-n junction solar cells, is derived here based solely on thermodynamic principles. Equations 2.17 and 2.18 encapsulate the fundamental aspects of the thermodynamic description of the operation of a solar cell. Notably, no reference is made to the specific material constituting the converter, as the voltage is expressed in terms of photon transfer between the incident and emitted beams.

Photon Beam Energy and Entropy

Under moderate illumination intensities, the statistics of photons resemble the statistical mechanics of a two-dimensional ideal gas. The two angular coordinates required to specify the beam's direction contribute to the number of dimensions in this analogy. It has been demonstrated [50] that this approximation holds well for solar radiation with concentration ratios up to approximately a hundred suns. In this transition from "photons in a box" to "photons in a beam," the particle count in the volume is replaced by the photon flux, and the volume is replaced by the beam's étendue ε [46]. Assuming the solar cell consists of a material with an energy gap $h\nu_g$, photons are incident from the sun at a rate $\dot{N}_{\text{in}}$ and are reemitted at a rate $\dot{N}_{\text{out}}$. The individual photon energy u and entropy s are determined as follows:

$$u = \left(\frac{\partial \dot{U}}{\partial \dot{N}}\right)_{\varepsilon,T} \tag{2.19}$$

$$s = \left(\frac{\partial \dot{S}}{\partial \dot{N}}\right)_{\varepsilon,T} \tag{2.20}$$

Here, $\dot{N}$, $\dot{U}$ and $\dot{S}$ represent the photon flux, convective energy flux, and entropy flux carried by the beam, respectively, as defined in [51] (or see appendix C). By utilizing the fluxes, the rate of irreversible entropy generation or exergy loss 2.18 can be determined. Just as the energy per particle in an ideal gas is independent of the total number of particles in the volume, the energy per photon remains unaffected by the photon flux and is given by

$$u(T, \varepsilon, \dot{N}) = h\nu_g + k_b T^2 \frac{\gamma^{'}(T)}{\gamma(T)} \approx h\nu_g + k_b T \tag{2.21}$$

The equation is derived in [50] where $\gamma(T)$ is defined in 2.23. From a thermodynamic perspective, the equation shows that the energy flow that effectively participates in the energy conversion, carried by a photon, carries both the photon energy that can be converted and thermal energy. The convertible photon energy is derived by considering the whole frequency range (ν_g, ∞) where $h\nu_g$ is the bandgap energy of the semiconductor. The thermal energy originates from the Bose-Einstein distribution[51],C. It is a measure of the energy quality of the photon when treated as heat, and is determined by the ambient temperature at the point where the photon is created. (Note that the emitted photons have a frequency equal to the bandgap frequency ν_g).
The entropy flux of a light beam is derived with the number of permutations as $S = k_b \ln W$, where W is the number of microstates or permutations. Which can be written as

$$W = \frac{(G+N)!}{G!N!} \approx \frac{(G+N)^{G+N}}{G^G N^N}$$

Where Stirling approximation is used, G is the number of states and N is the photons in the light beam. It has been shown previously [50] and in 2.6 that $G = \frac{2\varepsilon\nu^2}{c^2}$, with ε the étendue, ν the frequency of the light beam and c the speed of light. This would lead to the following expression for the entropy flux of a monochromatic light beam.

$$S = k_b \ln W = k_b \frac{2\nu^2 \varepsilon}{c^2} \{(1+\rho)\ln(1+\rho) - \rho \ln \rho\}$$

With $\rho = \frac{N}{G}$ the mean photon number per mode. The equation translates the number of photon states in a box into the number of states in a beam, including an étendue term. The entropy per added or removed photon in a beam can then be calculated by differentiation with respect to the photon number in the beam as

$$s_i(T, \varepsilon, N) = \frac{\delta S_i}{\delta N_i} = k_b \ln\left(1 + \frac{2\nu_i^2}{c^2}\frac{\varepsilon_i}{N_i}\right) \approx k_b \ln\left(\frac{2\nu_i^2}{c^2}\frac{\varepsilon_i}{N_i}\right)$$

Where the subscript i denotes the incoming or outgoing beam, the equation considers only a single frequency, and the approximation holds for low to medium intensities [48] ($\approx$ 1000suns). However, for a full description of a working solar cell, the thermodynamic variables need to be converted to flows and include all light over the frequency range of the solar spectrum. It has been shown in [47, 48] that this results in

$$s = k_b\{\ln\left(\frac{\varepsilon_i \gamma_i(T)}{\dot{N}_i}\right) + 1\} \approx k_b \ln\left(\frac{\varepsilon_i \gamma_i(T)}{\dot{N}_i}\right) \tag{2.22}$$

Where

$$\gamma_i(T) = \int_{\nu_g}^{\infty} \frac{2\nu^2}{c^2} e^{\frac{h(\nu_g - \nu)}{k_b T}} = \frac{2\nu_g^2 k_b T}{hc^2}(1+\alpha_i) \tag{2.23}$$

With $\alpha_i = 2\frac{k_b T}{h\nu_g} + 2\left(\frac{k_b T}{h\nu_g}\right)^2$ which represents a small correction, where ν_g is the frequency corresponding to the bandgap energy. When $h\nu_i \gg k_b T$ the correction term is negligible which is the case for conventional solar cells.
The chemical potential as $\mu = u - Ts$ can then be written as

$$\mu \approx h\nu_g - k_b T_0 \ln\left(\frac{\dot{N}}{\varepsilon\gamma(T)}\right)$$

Substituting 2.19 and 2.20 in 2.18 (with the correct energy 2.21 and entropy 2.22) the exergy loss per photon can be determined with.

$$\begin{aligned} T_0\sigma_i &= \{u(T_s, \varepsilon_{in}, \dot{N}_{in}) - u(T_0, \varepsilon_{out}, \dot{N}_{out})\} - T_0\{s(T_s, \varepsilon_{in}, \dot{N}_{in}) - s(T_0, \varepsilon_{out}, \dot{N}_{out})\} \\ &= \{u(T_s) - u(T_0)\} - T_0\{s(T_s, \varepsilon_{in}, \dot{N}_{in}) - s(T_0, \varepsilon_{in}, \dot{N}_{in})\} \\ &\quad + \{s(T_0, \varepsilon_{in}, \dot{N}_{in}) - s(T_0, \varepsilon_{out}, \dot{N}_{in})\} \\ &\quad + \{s(T_0, \varepsilon_{out}, \dot{N}_{in}) - s(T_0, \varepsilon_{out}, \dot{N}_{out})\} \end{aligned} \tag{2.24}$$

The equation consists of three distinct terms enclosed in curly brackets. In the following section, a more in-depth explanation of each of these terms is given.

Kinetic Entropy

Let's extract the last term in curly brackets from equation 2.24 and denote it as σ_{kin}. This term represents the entropy generation due to the finite current being extracted from the solar cell, corresponding to the turnover rate of the "engine":

$$\sigma_{kin} = s(T_0, \varepsilon_{out}, \dot{N}_{in}) - s(T_0, \varepsilon_{out}, \dot{N}_{out}) = k_b \ln\left(\frac{\dot{N}_{in}}{\dot{N}_{out}}\right)$$

For now, let's consider an ideal solar cell where all absorbed photons are either emitted or converted into electrical current. Taking into account the equilibrium photon fluxes at temperature T_0 of the converter, denoted by $\dot{N}_{\text{in}}^0$ and $\dot{N}_{\text{out}}^0$, the photon balance can be expressed as:

$$\dot{N}_{in} - \dot{N}_{out} = \dot{N}_{in}^0 - \dot{N}_{out}^0 + \frac{I}{q} \simeq \frac{I}{q}$$

Here, I represents the electrical current extracted from the solar cell. In the second part of the equation, we neglect the difference in equilibrium fluxes. Thus, we have:

$$\sigma_{kin} = k_b \ln\left(\frac{I_{ph} + I_0}{I_{ph} + I_0 - I}\right)$$

where $I_{ph} = q(\dot{N}_{\text{in}} - \dot{N}^0_{\text{out}})$ is the photogenerated current, and $I_0 = q\dot{N}^0_{\text{out}}$ is the dark diode saturation current (blackbody). However, in the presence of non-radiative transitions, the photon balance becomes

$$\dot{N}_{in} = \dot{N}_{out} + \dot{N}_{nr} + \frac{I}{q}$$

where $\dot{N}_{nr}$ is the rate of non-radiative recombination in the system. The kinetic work (σ_{kin}) can then be written as

$$\sigma_{kin} = k_b \ln\left(\frac{\dot{N}_{in}}{\dot{N}_{out}}\right) = k_b \ln\left(\frac{\dot{N}_{in}}{\dot{N}_{in} - \frac{I}{q}}\right) + k_b \ln\left(\frac{\dot{N}_{out} + \dot{N}_{nr}}{\dot{N}_{out}}\right) = k_b \ln\left(\frac{I_l + I_0}{I_l + I_0 - I}\right) - k_b \ln(\eta^{PL}_{ext})$$

where $\eta^{PL}_{ext} = \frac{\dot{N}_{out}}{\dot{N}_{out} + \dot{N}_{nr}}$ the radiative recombination efficiency.

Thermalization

The first term on the right hand side of 2.24 is the entropy generation σ_c which describes the irreversible cooling of the photon beam from the solar temperature T_s to the ambient temperature T_0. This loss represents the "thermalization" process of electron-hole pairs in a semiconductor immediately after light absorption. It is commonly regarded as one of the two fundamental losses in the operation of an ideal solar cell and can be written as [50].

$$T_0\sigma_c = (u(T_s) - u(T_0)) - T_0 k_b \ln\left(\frac{\gamma(T_s)}{\gamma(T_0)}\right) \approx T_0 k_b \left(\frac{T_s}{T_0} - 1\right) - T_0 k_b \ln\left(\frac{T_s}{T_0}\right)$$

The first term on the right side represents the "thermal" photon energy difference between the incoming and emitted light beam ($u = u_{photon} + u_{thermal} = h\nu_g + k_b T$ 2.21). While the second term can be seen as a heat recovery system, where the rejected heat in the conversion process, is absorbed by the carriers. Which results in increased energy of the charge carriers at the band edge due to their increase in thermal energy. Shifting the fermi-dirac distribution and increasing the apparent bandgap.

Étendue

The second term in equation 2.24, σ_{exp}, is a consequence of étendue expansion between the incident and emitted beams, characterized by étendues ε_{in} and ε_{out}. Based on the principle of microscopic reversibility, we have $\varepsilon_{in} \leq \varepsilon_{out}$, which implies that σ_{exp} is always greater than or equal to zero. This term can be expressed as [46][47][48][50]:

$$\sigma_{exp} \approx k_b \ln\left(\frac{\varepsilon_{out}}{\varepsilon_{in}}\right)$$

In terms of the second law of thermodynamics, while entropy does not necessarily need to be conserved, it cannot decrease during the passage of photons through the system ($\Delta S \geq 0$). As long as the number of photons in the beam remains constant, this implies that $\varepsilon_{in} \leq \varepsilon_{out}$.
As explained before in section 2.3 a concentration factor can be introduced which is the consequence of a lens. The entropy loss should change accordingly [36]:

$$\sigma_{exp} \approx k_b \ln\left(\frac{\varepsilon_{out}}{\varepsilon_{lens}}\right) = k_b \ln\left(\frac{\varepsilon_{out}}{\varepsilon_{in} X}\right) \tag{2.25}$$

Special care needs to be taken concerning the concentration factor, which is defined as the ratio of the total lens area divided by the total effective solar cell area. In other words, when a solar cell is illuminated the factor can only be considered when the solar cell also reduces in size, or if the lens area is larger than the solar cell itself thus collecting more light.

Open Circuit

We can now write down the full equation with 2.17 as

$$qV = qV_{oc} - k_b \ln\left(\frac{I_l + I_0}{I_l + I_0 - I}\right)$$

Which is the thermodynamic analog of the Shockley ideal solar cell equation [9]. At open circuit conditions, the current is by definition zero ($I = 0$), which gives the following expression for the open circuit voltage:

$$qV_{oc} = \left(1 - \frac{T_0}{T_s}\right) u_{in} - T_0 \sigma_i(oc)$$

Substituting the different loss terms (σ_i) and 2.21 gives:

$$qV_{oc} = \left(1 - \frac{T_0}{T_s}\right) h\nu_g + k_b T_0 \ln\left(\frac{T_s}{T_0}\right) - k_b T_0 \ln\left(\frac{\varepsilon_{out}}{\varepsilon_{in}}\right) + k_b T_0 \ln\left(\eta_{ext}^{PL}\right)$$

Rewriting it gives the same formula for the V_{oc} presented throughout works on solar cells [8][9], but obtained from thermodynamic considerations instead of detailed balance, giving a complementary, thermodynamic insight on solar cells.

$$qV_{oc} = \left(1 - \frac{T_0}{T_s}\right) h\nu_g + k_b T_0 \ln\left(\frac{T_s}{T_0}\right) + k_b T_0 \ln\left(\frac{\varepsilon_{in}}{\varepsilon_{out}}\right) + k_b T_0 \ln\left(\eta_{ext}^{PL}\right) \tag{2.26}$$

The initial two terms in equations 2.26 are fixed and challenging to modify. However, practical measures can be taken to minimize these losses, such as cooling the solar cells to mitigate their impact. It is also possible to reduce the absorbed heat by matching the incident photon energy to the bandgap energy such that no photons are incident below the bandgap and no surplus energy in the photons is present. However, it is important to consider absorption as well. In practice, semiconductor materials do not exhibit 100% absorption of photons with energy equal to the bandgap, instead, they have higher absorption for a range of photons with energies greater than the bandgap.
The étendue term can be reduced by redirecting the emitted light back toward the sun, matching the étendue of the incident beam. This can be achieved using mirrors, lenses, or other optical components. Additionally, the use of nanowires in solar cells with appropriate geometric structures induces guided modes within the nanowires. As a result, the emitted photons are directed back toward the sun with a specific étendue associated with the guided mode.
The final term incorporates the photoluminescence efficiency, which indicates that minimal entropy loss occurs when all absorbed photons are reemitted at open circuit conditions. This situation is achieved when nonradiative recombination is absent or minimized, leading to the radiative limit.

2.6.2 Exergy and Thermalization Loss

Exergy can be defined as the maximum amount of useful work that can be obtained from a system as it reaches equilibrium with its surroundings. Unlike energy, which is conserved, exergy represents the potential to perform useful work and is subject to losses and degradation in real-world processes.
The concept of exergy is based on the second law of thermodynamics, which states that energy spontaneously flows from regions of higher energy to regions of lower energy until equilibrium is reached. This natural tendency towards equilibrium introduces irreversible processes and energy losses. Exergy helps quantify these losses and evaluate the efficiency of energy conversions.
The exergy balance of a system is defined as [52]:

$$\sum \dot{B}_{in} = \frac{d\dot{B}_{sys}}{dt} + \sum \dot{B}_{out} + \sum \dot{B}_d$$

where $\dot{B}_{in}$ represents the exergy flow going in the system, $\frac{d\dot{B}_{sys}}{dt}$ the exergy change, $\dot{B}_{out}$ exergy flow leaving the system and $\sum \dot{B}_d$ the exergy destroyed.
The exergy of an energy flow in a specific form can be defined by [52]

$$B = U + PV - TS - \sum \mu_i N_i$$

Where U is the internal energy, P the pressure, V the volume, T the temperature, S the total entropy, μ_i the chemical potential of component i and N_i the moles or number of particles of component i. Each term in the equation possesses its own designation: PV is referred to as "available PV work," TS is known as "entropic loss" or "heat loss," and the final term is called "available chemical energy."
In the previously defined system by Markvart [37] the exergy of a solar cell is equal to equation 2.26 which is deduced from 2.17. The entropy generating processes are defined as the heat engine and the change in configurations of the incident and emitted light beam. This is due to their étendue expansion, photon cooling, and radiative recombination efficiency. In the system defined, the photons equal pure heat entering or leaving a heat engine with an entropy generating conversion process, where the maximal available work efficiency equals the Carnot efficiency.
However, one can argue that photons are not equal to pure heat, but are equal to electromagnetic radiation, another form of higher-quality energy. There is thus a difference in radiative energy and heat energy. Assuming the Carnot efficiency is simplifying the problem. When considering photons as heat, another extra conversion process needs to be introduced where photons are first converted to heat, hereafter they can be used in the heat engine, as seen from figure 2.16

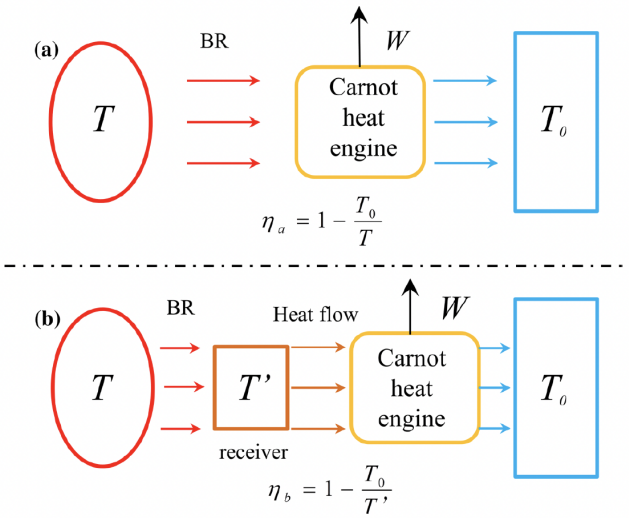

Figure 2.16: The schematic illustrating the generation of work by the Carnot heat engine through radiation (a) where radiation directly enters the heat engine as pure heat, and (b) where radiation is first converted into heat energy before entering the heat engine. [53].

If the blackbody radiation at temperature T converts into thermal energy at temperature $T^{'}$, $T^{'}$ must be less than T; otherwise, radiation heat transfer cannot occur. The thermal energy comes into the Carnot heat engine to perform work, and its efficiency $\eta_{Carnot} = 1 - \frac{T_0}{T}$, with $1 - \frac{T_0}{T'} < 1 - \frac{T_0}{T}$. This indicates that the radiation exergy coefficient must be smaller than the Carnot efficiency.

Exergy of Blackbody

Similar to the model of the Carnot heat engine, a radiation machine model is used to explore the exergy formulation of blackbody radiation [53]. This approach enhances our understanding of the thermodynamics of radiation. As depicted in Figure 2.17, the radiation machine represents an ideal black box converter. The input energy corresponds to the blackbody radiation energy flow E_{in}, characterized by temperature T and entropy flow S_{in}.

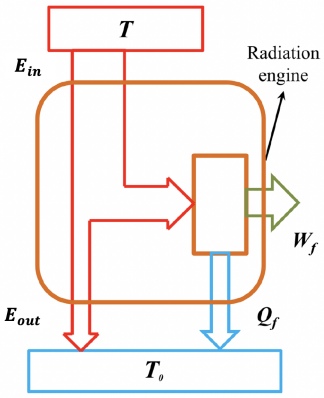

Figure 2.17: The radiation machine model[53].

The output energy is the blackbody radiation energy flow E_{out} with temperature T_0 and entropy flow S_{out}, which is in equilibrium with the ambient conditions. The entire radiation engine process generates a power flow W_f, representing the maximum achievable work. Heat conduction with the environment is denoted as Q_f, accompanied by an entropy flow S.
Based on thermodynamics principles [54], the entropy of blackbody radiation is $\frac{4}{3}\sigma T^3$, where σ denotes the Stefan-Boltzmann constant. Additionally, Wright [55] conducted an extensive investigation of radiation entropy, suggesting that radiation entropy flow can be expressed as $n\frac{Q_f}{T}$. For blackbody radiation, n equals 4/3, thus enabling the expression of radiation entropy flow as $\frac{4}{3}\sigma T^3$. According to the first law of thermodynamics, the energy balance equation is as follows:

$$E_{in} = E_{out} + Q_f + W_f$$

Following the second law of thermodynamics, the entropy balance equation can be formulated as:

$$S_{in} = S_{out} + \Delta S_f + S_f$$

Here, ΔS_f represents entropy production. For a reversible process with maximum conversion efficiency, ΔS_f equals zero. The expressions for the input and output energy and entropy flow and entropy flow of heat conduction with the environment are $E_{\text{in}} = \sigma T^4$, $E_{\text{out}} = \sigma T_0^4$, $S_{\text{in}} = \frac{4}{3}\sigma T^3$, $S_{\text{out}} = \frac{4}{3}\sigma T_0^3$, and $S_f = \frac{Q_f}{T_0}$, respectively. By substituting the entropy expression into the entropy balance equation, we obtain:

$$Q_f = (S_{in} - S_{out})T_0 = \frac{4}{3}\sigma(T^3 - T_0^3)T_0$$

Substituting this in the energy balance:

$$W_f = E_{in} - E_{out} - T_0(S_{in} - S_{out}) = \sigma(T^4 - T_0^4) - \frac{4}{3}\sigma(T^3 - T_0^3)T_0$$
$$= \sigma T^4 - \frac{3}{4}\sigma T^3 T_0 + \frac{1}{3}\sigma T_0^4$$

The so-called energy-to-exergy ratio is then:

$$\eta_B = \frac{W_f}{E_{in}} = \frac{\sigma T^4 - \frac{3}{4}\sigma T^3 T_0 + \frac{1}{3}\sigma T_0^4}{\sigma T^4} = 1 - \frac{3}{4}\frac{T_0}{T} + \frac{1}{3}\left(\frac{T_0}{T}\right)^4$$

Which is known as Petela's exergy equation [54], sometimes referred to as Landsberg efficiency. A similar derivation can be used where the entropy flux is associated with heat entropy with $S = \frac{Q_f}{T} = \sigma T^3$ [53], this would result in the Carnot efficiency, where thus the photons are treated as pure heat.

Exergy of Monochromatic Photons

While blackbody radiation serves as the conventional radiation model, the exploration of non-blackbody radiation is of significant interest in engineering research. To study non-blackbody radiation, it is essential to investigate monochromatic radiation. Monochromatic radiation can be viewed as the summation of monochromatic photons. Therefore, analyzing the characteristics of monochromatic photons is essential before investigating non-blackbody radiation.
The exergy of monochromatic photons has garnered increased attention in the context of photosynthesis. The exergy of organic compounds produced during photosynthesis originates from the exergy of photons absorbed by chlorophyll, which aligns with the principles of the second law of thermodynamics. Consequently, researchers have proposed formulas to calculate the exergy of monochromatic photons [56][57]:

$$B = h\nu\left(1 - \frac{T_0}{T_r}\right)$$

The corresponding coefficient of exergy-to-energy is:

$$\eta_B = 1 - \frac{T_0}{T_r}$$

This formula bears a resemblance to Carnot's efficiency. While the ambient temperature T_0 is commonly acknowledged, there are differing views regarding the definition of T_r. Some researchers consider it as the surface temperature of radiation, such as the surface temperature of the sun in a solar cell or photosynthesis system [58][59]. Others argue that T_r should fall within a specific temperature range [60]. Moreover, Meszéna et al. [61] and Chen and Mo [62], among others, propose that T_r should be an equivalent temperature $T_{(v)}$ expressed in temperature units, which captures the energy quality.
The exergy analysis performed here is based on an equivalent temperature. However, as mentioned before, radiant energy differs from thermal energy, and the Carnot efficiency is not suitable for macroscopic radiation exergy calculations. Consequently, an exergy-to-energy ratio similar to Carnot efficiency may not be reasonable for the exergy calculation of monochromatic photons. This aspect has been overlooked by researchers in the field of radiation photon exergy for many years. Consequently, an infinite-staged Carnot engine model is used [53] [63], utilizing the concept of equivalent temperature to conduct a more comprehensive analysis of the exergy of monochromatic photons see figure 2.18.

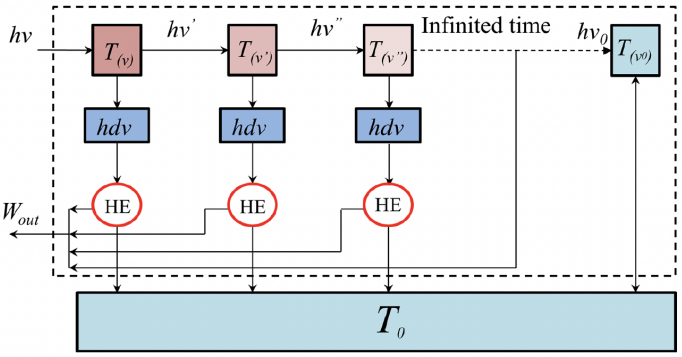

Figure 2.18: The infinite-staged Carnot heat engine model[53].

Considering a bundle of monochromatic light with a fixed frequency ν, each photon carries an energy of $h\nu$ and possesses an equivalent temperature $T_{(v)}$. As illustrated in figure 2.18, an absorption model that absorbs radiation photons' energy $h\nu$ is established. The absorption model subsequently emits a radiation photon with frequency ν' and energy $h\nu'$ while generating thermal energy $hd\nu$. This thermal energy $hd\nu$ performs work through the Carnot heat engine operating at an equivalent temperature $T_{(v)}$. By assuming $d\nu$ to be infinitesimally small, this model will continue the process indefinitely until the frequency reaches a certain value v_0, corresponding to an equivalent temperature $T_{(v_0)}$ that aligns with the ambient temperature T_0. The entire infinite-staged Carnot engine model represents a non-dissipative reversible process, where the output work symbolizes the exergy of monochromatic radiation photons.
Thus, considering the entire infinite-staged Carnot engine model process, the exergy of a photon can be expressed as:

$$W_B = \int_{\nu_0}^{\nu} h\left(1 - \frac{T_0}{T_{(\nu)}}\right) d\nu$$

It is observed that the maximum useful work of a photon should be expressed in integral form rather than simply as hv multiplied by the Carnot efficiency after introducing the concept of equivalent temperature (one can argue that it can also be expressed in terms of a sum rather than an integral due to the quantum nature of phonons and photons). This is because photons fundamentally belong to electromagnetic radiation rather than thermal energy. Therefore, the change in energy quality during the energy conversion process can only be captured in the quasi-equilibrium process, as discussed above.
For a solar cell at open circuit conditions, before it reaches the radiative limit, the nonradiative recombined photons will reach ν_0 at corresponding temperature $T_{(\nu_0)} = T_0$, while radiative recombined photons will reach ν_{out} at $T_{(\nu_{out})}$. Suggesting a higher temperature for the emitted photons than the ambient temperature. While the incident photons are still emitted from a black body and carry the temperature of the sun. Because photons follow a Bose-Einstein distribution the equivalent temperature is suggesting that the emitted monochromatic photons are created at a local ambient temperature of $T_{(\nu_{out})}$.
The study by Z. Zhou et al. [53] demonstrated, using the infinite heat engine concept, that the equivalent temperature can be approximated as:

$$T_{(\nu)}^4 = \frac{f\nu}{c} T^3 \tag{2.27}$$

With $f = 4.5638 * 10^{-3}[m \cdot K]$ when the radiative temperature is higher than the ambient temperature $T > T_0$. Furthermore, they showed that the corresponding exergy-to-energy ratio is similar to Petela's equation for a blackbody, the exergy-to-energy ratio for monochromatic photons is:

$$\eta_B = 1 - \frac{3}{4}\frac{T_0}{T_{(\nu)}} + \frac{1}{3}\left(\frac{T_0}{T_{(\nu)}}\right)^4$$

The derivation of the exergy-to-energy ratio and the equivalent temperate can be found in the appendix D or in the corresponding paper [53]. It is worth mentioning that in the derivation an uncertainty is introduced due to the numerical calculation of the number f. However, the error is less than 2.8% and only decreases for higher temperatures.
Clearly, high-frequency radiation exhibits higher energy quality and a higher equivalent temperature $T_{(\nu)}$. Petela [54] studied the exergy spectrum of blackbody and gray-body surface radiation and found that, at the same radiation temperature, a higher frequency ν leads to a higher exergy-to-energy coefficient η_u and a higher equivalent temperature $T_{(\nu)}$ (see figure 2.19). Therefore, the most reasonable way to use solar energy is to use frequency division utilization to minimize spectral mismatch.

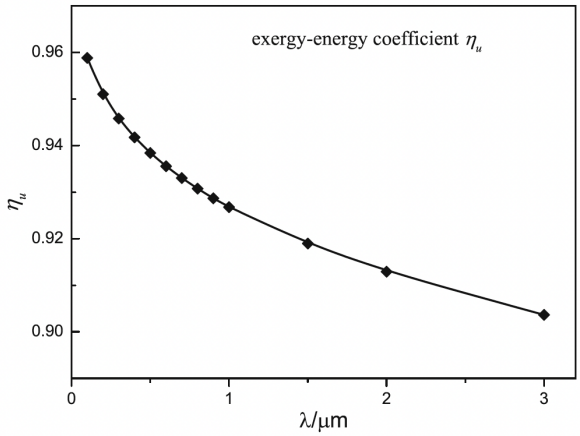

Figure 2.19: The relationship between monochromatic radiation exergy-to-energy coefficient and wavelength λ at the solar radiation temperature $T = 5772K$[53].

Furthermore, Petela demonstrated that different radiant temperatures yield varying exergy-to-energy coefficients of monochromatic radiation, where higher temperature radiation corresponds to higher exergy-to-energy coefficients of monochromatic radiation. This implies that a higher radiation temperature T

results in a higher equivalent temperature $T_{(\nu)}$ for monochromatic radiation.

The difference between Markvart's reasoning and Petela's exergy equation is that Petala's equation considers all the emitted photons and the total entropy generation, while Markvart considers the individual photon energy and entropy. However, the concept of equivalent temperature can be of added value in Markvart's equations. In his derivation the emitted photons are at temperature T_0 using, the concept of equivalent temperature, we see that the emitted photons are related to the ambient temperature by equation 2.27. When the assumption is made that the equation is also valid for radiation induced by radiative recombination of an electron and hole. The purpose of this analysis is to show that the emitted photon temperature does not have to be at ambient temperature but rather at a higher equivalent temperature. The combination of equivalent temperature derived by Z. Zhou with Martvart's equations is not yet described in this way. It serves here more as an example rather than an attempt to change the already established fundamental equations.
The thermodynamical system at open circuit conditions can then be described as figure 2.20.

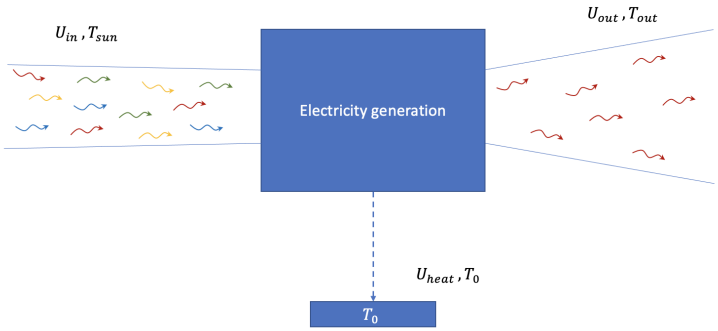

Figure 2.20: Schematic representation of a solar cell cycle at open circuit conditions, where incoming photons generate electricity with $I = 0$ and $V = V_{oc}$. The electricity generated is used to produce photons (the solar acts as a LED).

Where the energy diagram looks like 2.21. The photon energy described by Markvart can be written as:

$$u(T, \varepsilon, \dot{N}) \approx h\nu + k_b T$$

where T is the temperature of the environment. However, in this model, we investigate what happens when the temperature used in the Bose-Einstein distribution for a photon created by an excited electron, is the local temperature at the point and time where the photon is created (the hot carrier temperature). This is because the Bose-Einstein distribution describes the probability of a photon occupying a given energy state, which determines its energy and entropy. The probability of a photon occupying a given energy state depends on the temperature experienced during its creation. In the case of a photon created by an excited electron, the local temperature at the point where the photon is created is higher than the ambient temperature. This is because the excited electron has a higher temperature than the ambient temperature, and this thermal energy is transferred to the photon when the photon is created. Therefore, the temperature that should be used in the Bose-Einstein distribution for a photon created by an excited electron is the local temperature at the point where the photon is created.

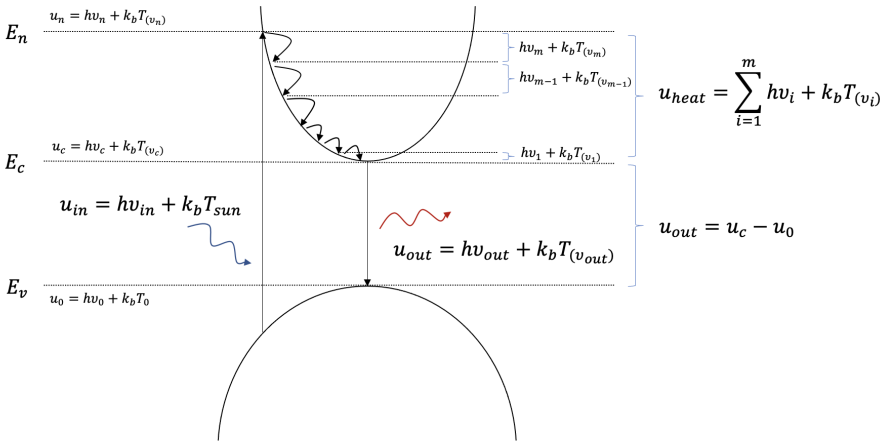

Figure 2.21: Schematic representation of the energy diagram of photon absorption including equivalent temperature.

In order to better understand the concept, the incident photon energy is higher than the bandgap energy and all the energy levels are written in terms of "potential photon energy" as described by Markvart and the concept of the infinite heat engine. However, the integral is now replaced by a sum due to the quantum nature of carrier cooling by phonon emission. Electricity is by definition pure exergy [64] and the conversion from electricity to photon energy is in theory thus without loss.
The incident photon enters the system with energy u_{in} at temperature T_s (black body radiation), the absorbed photon is converted to an excited electron and immediately rejects part of its thermal energy until it reaches its equivalent temperature $T_{(\nu_n)}$ giving the excited electron energy u_n. Hereafter the excited electron cools down by first emitting larger energy optical phonons and subsequently emitting lower energy acoustic phonons until it reaches the bottom of the conduction band with energy u_c, emitting u_{heat} in the process. In the conduction band, the electron can radiatively recombine with a hole to create a photon with energy u_{out} in this process no energy is lost as heat.
In Marktvart's analysis, the emitted photon beam is created at temperature T_0, however as shown by Z. Zhou et al [53], the emitted photons at a single frequency can carry a certain equivalent temperature, suggesting a higher local temperature during the creation of the photon. Implementing this in Marktvarts analysis we can change Marksvarts equations accordingly. Because only the emitted photon temperature changes from T_0 to T_{out} the first term on the right hand side of 2.24 or the thermalization loss changes. Which results in:

$$T_0\sigma_c = (u(T_s) - u(T_{out})) - T_0k_b \ln\left(\frac{\gamma(T_s)}{\gamma(T_{out})}\right) = T_{out}k_b\left(\frac{T_s}{T_{out}} - 1\right) + T_0k_b \ln\left(\frac{T_{out}}{T_s}\right)$$

Which leads to an open circuit voltage as:

$$qV_{oc} = \left(1 - \frac{T_0}{T_s}\right)E_g + k_b(T_{out} - T_0) + k_bT_0 \ln\left(\frac{T_s}{T_{out}}\right) + k_bT_0 \ln\left(\frac{\varepsilon_{in}}{\varepsilon_{out}}\right) + k_bT_0 \ln\left(\eta_{ext}^{PL}\right)$$

In figure 2.22 the effect on the thermalization loss with different emitted effective temperatures is shown. Where maximal thermalization loss corresponds with an emitted photon effective temperature equal to the ambient temperature T_0 and the minimal loss corresponds to an effective temperature T_s.

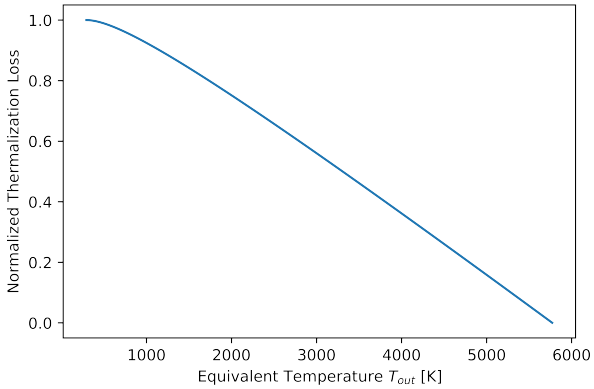

Figure 2.22: Normalized thermalization loss for different emitted photon temperatures. This graph shows that when the emitted photons' temperature increases the entropy loss associated with it decreases due to a more reversible system.

The equivalent temperature for an emitted photon in the InP is calculated with equation 2.27, where the emitted photon has a wavelength corresponding to the bandgap energy; $\lambda = 920$nm, and $T \approx T_0 = 293K$ which results in an equivalent temperature of $T_{out} \approx 594K$. The thermalization loss would reduce by 2.04% compared to an emitted photon beam at a temperature of T_0, due to a higher reversible system. The calculation is now made for a single photon. It can be argued that when illuminating with more photons, the local ambient temperature (T_0) experienced by the excited electron is higher due to (hot) carriers surrounding the excited electron [65] D.1, increasing the equivalent temperature. For example, when only the bottom of the conduction band is fully occupied, the experienced ambient temperature by the carrier can potentially be approximated by the equivalent temperature of a single excited carrier in the bottom of the conduction band and is equal to $T_0 = 594K$, this leads to an equivalent temperature of $T_{out} = 1010K$ and a reduction in thermalization loss of 2.63%, showing that higher excitation reduces the thermalization loss. This theory does not consider the internal kinetics with other particles in the system and is not yet verified.

Chapter 3

Method and Fabrication

3.1 Experimental Setups

3.1.1 Photoluminescence

PL Setup

Figure 3.1 shows the schematic of the PL setup. A continuous wave (CW) laser emitting light at 532 nm (green) is used. The excitation power is controlled by a neutral density (ND) filter, which absorbs a portion of the light. The light is then split into two equal parts using a 50/50 beam-splitter. One part is directed towards a power meter to measure the excitation power, while the other part is focused onto the sample using a lens.
In addition, white light (yellow) is directed to the sample using a different beam-splitter. The emitted and reflected light (red) from the sample is directed back to the 50/50 beam-splitter and then passes through a band-pass filter and a monochromator. The band-pass filter removes short-wavelength light, filtering out the laser light. The monochromator disperses the light before it is collected by a CCD to obtain the emission spectrum. By measuring for a certain time duration (t), the integrated PL spectrum is obtained.
Furthermore, just after the beam-splitter, the light can also be directed towards a camera using a removable mirror. The white light and the camera are utilized to observe the sample, allowing the laser spot to be precisely positioned on the region of interest.

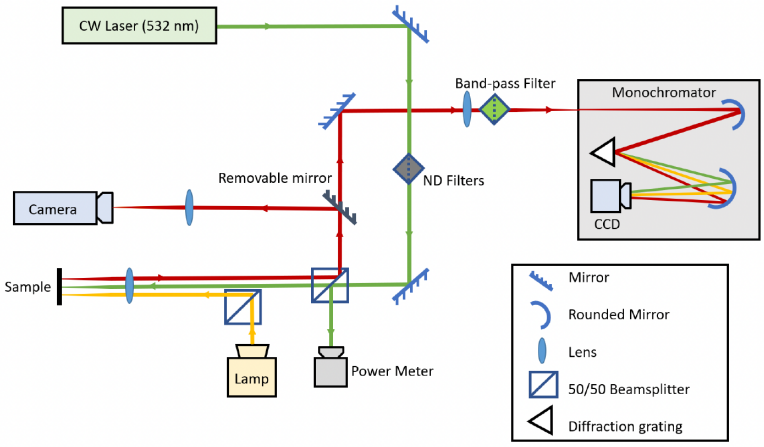

Figure 3.1: Schematic overview of the PL setup. Green represents the laser light, yellow represents the white light from the lamp, and red indicates the reflected and emitted light from the sample. The monochromator captures the emitted light and provides an integrated PL spectrum. The camera and white light assist in aligning the laser spot on the sample.

3.1.2 I-V curve measurement

Solar simulator setup

The experimental setup for measuring the current-voltage (I-V) characteristics of the fabricated solar cells is illustrated in Figure 3.2. The solar cell is positioned on a sample holder and subjected to illumination from a solar simulator, which utilizes a Xenon arc lamp to emit white light at an intensity comparable to that of sunlight. Two contacting pins are employed to create a closed electrical circuit. One pin is connected to the top contact of the cell, while the other is connected to the back contact. Both pins are mounted on mechanical translation stages, enabling precise positioning control. The pins are linked to a Keithley 2601b Sourcemeter, which is controlled by an external computer. The Sourcemeter applies a bias voltage across the cell while simultaneously measuring the current supplied by the cell. By varying the applied voltage and recording the corresponding current, the I-V curve of the solar cell is determined. Due to the presence of a transparent spacer layer of several microns covering the top contacts of the solar cell, electrical contact can only be established by locally removing the spacer layer. This is accomplished by firmly pressing the pins onto the sample and gently moving them sideways, causing the spacer layer to break and be locally eliminated. Care must be taken during this process as the pins' sharp points can potentially damage the cell by breaking the gold contacts or wires underneath. The procedure demands sensitivity and caution to ensure that the gold contacts remain intact and proper contact is established.

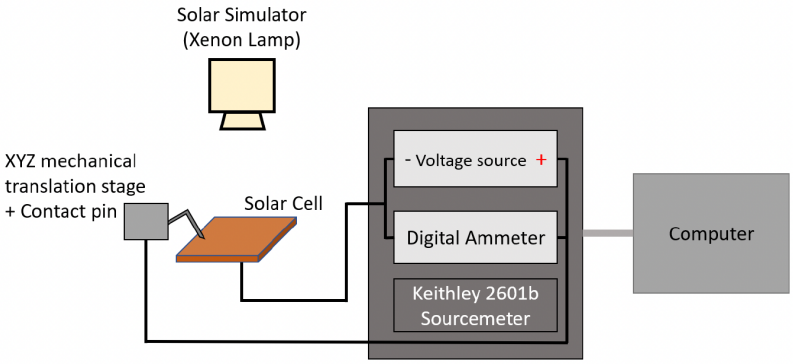

Figure 3.2: Schematic of the solar simulator for I-V measurements. Solar cells are illuminated by one sun-intensity solar simulator (Xenon arc lamp). The source meter applies bias and measures cell current for I-V curve.

I V curves under different excitation setup

The experimental configuration for measuring different excitation powers is similar to the Solar Simulator Setup previously described. However, in this case, the illumination is provided by a continuous wave laser operating at a wavelength of 532 nm. The laser light passes through a neutral density filter, which is then measured using a movable power meter. Once the power measurement is obtained, the power meter is shifted out of the light path, and the solar cell is illuminated using the same setup as before.

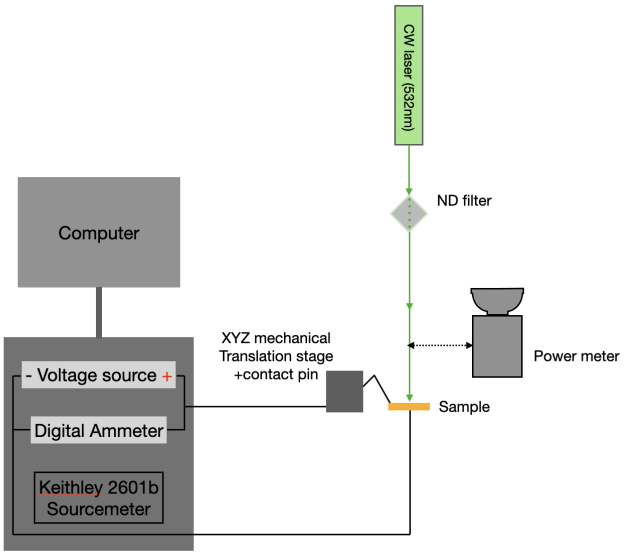

Figure 3.3: Schematic of the setup used to measure the I-V curves under changing excitation power. The solar cells are illuminated by a continuous wave laser at 532 nm. The source meter applies bias and measures cell current for I-V curve.

3.2 Fabrication

The manufacturing process, excluding the placement of micro lenses, is summarized in figure 3.4, the whole fabrication can be broadly divided into six production steps: InP Wafer Layer-Stack, Mask and Patterning, Etching, Passivation and Back Contact, Top Contact, and Micro Lenses. This section will provide a more detailed explanation of the etch fabrication step.
The boxed text provides an overview of the main steps involved in the specific fabrication step, while the text outside the box contains detailed instructions, specific information, and helpful tips and tricks related to each step of the fabrication process. To understanding the manufacturing process only the boxed text and figures 3.5, 3.6, 3.9,3.11, 3.12,3.14 needs to be understood.

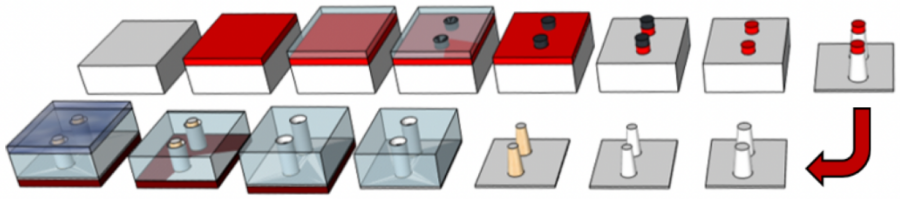

Figure 3.4: Schematic overview of the fabrication process without microlenses. Fabrication steps in order represented are 1. SiN mask deposition 2. EBL resist deposition 3. EBL exposure 4. Developing resist 5. Etching SiN mask 6. Resist removal 7. Etching of nanowires 8. Mask removal 9. Digital etching 10. Surface passivation 11. BCB deposition 12. Back-contact deposition 13. Etching of BCB layer 14. Front contact deposition.

3.2.1 InP Wafer Layer-Stack

The fabrication process of InP nanowire solar cells begins with a clean 2-inch InP wafer. Doped layers are grown on top of the wafer using the metal-organic vapor phase epitaxy (MOVPE) technique. The layer stack for solar cell fabrication starts with a Zn p-doped wafer with a thickness of $300\mu m$. An InGaAs layer is grown on the back side of the wafer to ensure an ohmic contact with the p-type InP. On the top facet of the wafer, a p^+-doped layer is grown to serve as a selective contact for holes and block minority carriers. This is followed by the growth of lower doped p- and n-type layers to form the pn-junction. The p-type layer has a thickness of $1600nm$ to enable efficient light absorption. Finally, a thin, highly doped n^+-layer is grown as a selective contact for majority carriers and to enhance conductivity with the top

contact. Figure 3.5 provides an overview of the complete layer stack while figure A.1 in the appendix displays the appearance of the wafer. After the pn-junction wafer is grown, it can be further processed to create a functional solar cell, as described in subsequent sections. The MOVPE is operated by René van Veldhoven personnel of the cleanroom.

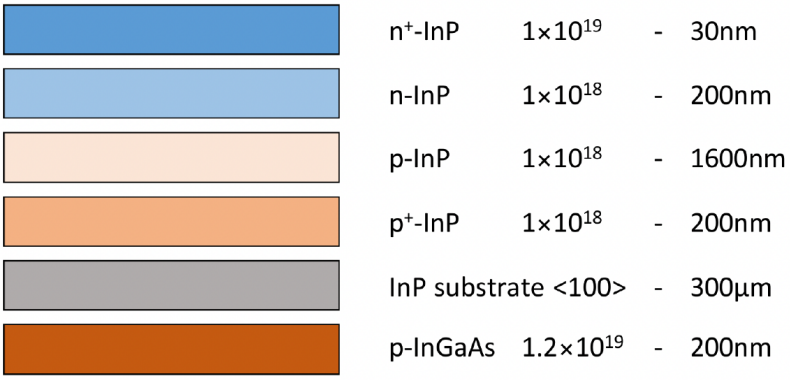

Figure 3.5: The figure provides a schematic overview of the layer stack in a pn-junction wafer used for solar cell fabrication. It shows the layer thicknesses and doping concentrations used in the structure.

3.2.2 Mask and Patterning

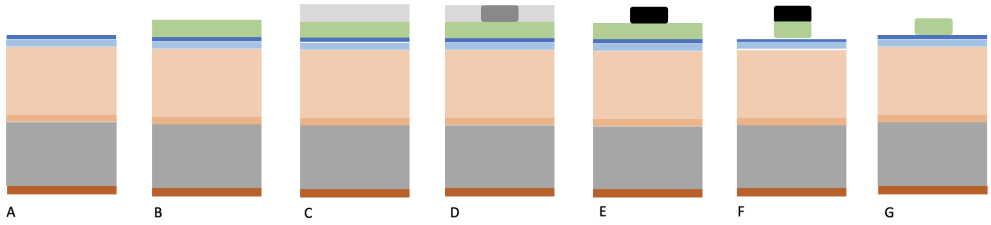

Figure 3.6: Overview of the steps involved in Mask and Patterning. A) cleaning the substrate B) deposition of 400nm SiNx mask C) adding a layer of resist (MaN-2403) D) pattering with EBL E) development F) mask etching G) resist removal. (note that steps 1.h and 1.i are also implemented in subfigure G)

1.a) Clean the InP wafer layer stack with a 2-minute bath in 1:10 diluted H3PO4.

The first step in the process involves cleaning the (100) InP wafer by immersing it in a 1:10 diluted Phosphoric acid (H3PO4) (85%) solution for 2 minutes to remove any native oxides on the surface. This is done in the wet bench; Acids. In a glass beaker, 100 milliliters of ultra-pure water is added which is measured in a graduated cylinder by its meniscus. The H3PO4 container is equipped with a pump that allows for adjustable dispensing of the 10 milliliters of H3PO4. Once the oxide layer is removed, the sample is immersed in an ultra-pure water bath until its resistivity reaches the desired level of $8 M\Omega.cm$. Subsequently, the sample is carefully transferred onto cleanroom paper and dried using Nitrogen gas. It is crucial to direct the airflow perpendicular to the sample surface and avoid using excessive blowing force to prevent the sample from being blown away. It is important to note that the sample should never be placed frontside down to avoid any potential damage and contamination. The backside of the sample can be cautiously dried by gently lifting the wafer with tweezers and applying low blow pressure to dry the back surface.

1.b) The process begins with depositing a 400nm thick layer of Silicon Nitride (SiNx) using Plasma Enhanced Chemical Vapor Deposition (PECVD). The SiNx layer acts as a protective shield for the underlying material. In the following steps, the SiNx layer is patterned and selectively removed, leaving behind the desired pattern in the form of SiNx.
Subsequently, the sample undergoes an etching process, where the SiNx mask acts as a protective barrier, safeguarding the area underneath. This ensures that only the InP (Indium Phosphide) material without the SiNx pattern is etched away, resulting in the creation of nanowires with the desired pattern.

In PECVD, a mixture of reactive gases, typically silane (SiH4) and ammonia (NH3), is introduced into a vacuum chamber. A (high) radio frequency (RF) plasma is then applied to the gas mixture, creating a highly energetic plasma. The plasma breaks down the gases into reactive species, such as radicals and ions, which react on the substrate surface. The silicon and nitrogen species combine to form SiNx, which deposits as a thin film on the substrate. The deposition rate, film properties, and stoichiometry of the SiNx film can be controlled by adjusting the gas flow rates, chamber pressure, and RF power. In preparation for depositing a 400 nm SiNx mask using OPT PECVD, several steps are taken. Firstly, the deposition rate of SiNx needs to be determined, and the reactor and carrier are preheated to account for any variations in deposition rate. A preconditioning process is performed to preheat the carrier; a 6-inch silicon wafer with a recess etched in the center to securely hold the sample. Different carriers are available for oxide and nitride depositions, as well as spare carriers. During the preconditioning, a small piece of silicon is placed on the Nitride carrier in the PECVD chamber, and the Nitride recipe is run for 5 minutes (A.3). Following the preconditioning, the thickness of the deposited SiNx on the small piece of silicon is measured using a reflectometer with the "SiNx (ICP_PECVD)" recipe. This measurement allows for the determination of the deposition rate, which is used to adjust the recipe to deposit a 400 nm SiNx layer on the InP layer stack. After the deposition, the wafer should have changed color from grey to greenish 3.7.

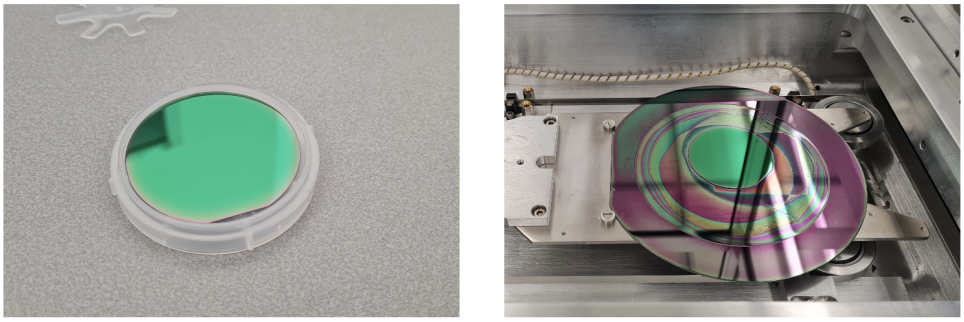

Figure 3.7: InP layer-stack after the deposition of 400nm SiNx with the PECVD.

1.c) Spin coat MaN-2403 resist on the sample with a speed speed of 3000 rpm for 30 seconds, hereafter, bake the resist for 50 seconds on a hotplate at 90°C. The resist is patterned in the electron beam lithography step.

The resist is applied using the spinner for lithography. The sample is positioned on the right mouthpiece of the spinner, which is slightly smaller than the 4-inch wafer, and a splash ring is utilized A.4. The appropriate recipe is selected. The wafer is carefully centered on the mouthpiece. Subsequently, the resist is dispensed onto the wafer using a pipette, and the recipe is executed, resulting in an approximate thickness of $0.3\mu m$ of resist on the sample. Immediately following the spinning process, the resist is subjected to a baking step on a hotplate A.5.

1.d) After loading the sample into the Raith EBPG5150, the pre-made recipe can be executed. The EBL process employs a focused electron beam to selectively expose a substrate coated with resist. The electron beam's precise control allows for custom patterns to be written onto the resist. Subsequently, the exposed resist is developed, revealing the desired pattern. The specific pattern used is explained in section 2.5 and here below.

The sample is now prepared for exposure using the Raith EBPG5150 (Electron Beam Lithography)

system. Prior to exposure, a design must be created using software programs like GDSII or Oasis. The design is then transferred to the CAD server, where the Beamer software allows for importing the design and exporting it as a GPF file. During this step, various modifications can be made, such as removing overlays, extracting specific layers or areas, and correcting proximity effects. Connection to the servers is established through "University Labaccess".
Next, the GPF file is transferred to the EBPG server, where Cjob software is used to import or export the GPF file. In Cjob, specific parameters such as the design location, current settings, beam diameter, and dose can be selected. Once the recipe is finalized, the sample is loaded into the machine. Holder 3 or 4 is typically used for sample loading during the current manufacturing process, allowing for easier leveling, rotation, and potential skipping of certain alignment steps.
Before running the recipe on the InP layer stack, it is crucial to check the dose, which plays a significant role in defining the features on the sample. Markers are utilized as reference points for the EBL system during overlay exposures. A dose test can be performed using a dummy wafer, where markers are placed at different doses. For instance, in previous fabrication in 2022, a dose of $500\mu C/cm^2$ was used, while in 2023, a dose of $50\mu C/cm^2$ was employed due to a build in multiplier in the software. Figure 3.8 illustrates an example of a dose test, showing Scanning Electron Microscope (SEM) images of markers with varying doses. Achieving the right dose is critical for proper overlay alignment during exposure. Ensuring the EBL system recognizes the hole in the marker.
In the current recipe, the design consists of a 3x3 array of 250nm circles, covering an area of $500 \times 500\mu m$. The pitch between the nanowires is 500nm, while the pitch between the 3x3 arrays is $6\mu m$ 3.10.

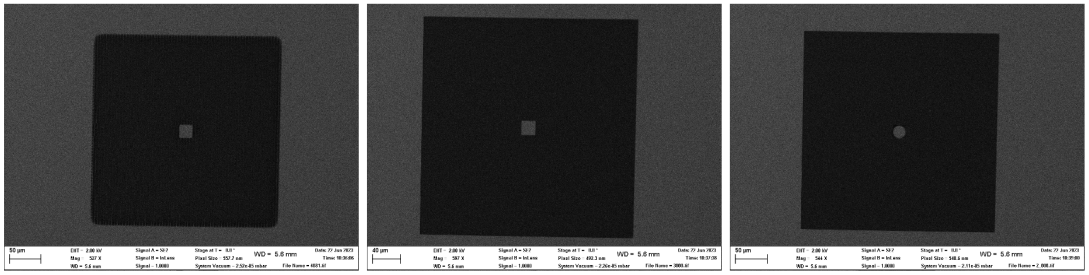

Figure 3.8: SEM images of a dose test: on the left, a dose of $50\mu C/cm^2$, in the middle a dose of $100\mu C/cm^2$ and on the right a dose of $150\mu C/cm^2$.

1.e) After exposure, the resist is developed in a beaker with MaD-532/s for 45 seconds and rinsed with Ultra Pure Water (UPW) for 10 minutes.

The time during development is important, a deviation of only 1 second can significantly change the feature size, the removal from the developer to the water bath should be done fast and can be done using a clamp holder. After the water bath, the sample is dried with Nitrogen. The pattern created with the EBL should be visible.

1.f) After the development process, the mask undergoes an etching step to transfer the pattern onto the SiNx mask. This etching process takes place in a parallel plate reactor (NRIE). The etchant gas used in this step is CHF3 (recipe: "pure CHF3 spoelen"). The etching duration is set to 28 minutes, which removes all the SiNx mask except underneath the developed resist pattern.

The NRIE works by using a combination of reactive ions and neutral radicals to etch a substrate. The substrate is placed between two parallel electrodes, and a plasma is created in the reactor using a mixture of reactive gases. The ions and radicals from the plasma chemically react with the substrate, removing the surface material. The specific etching time ensures sufficient time to etch through the mask and optimizing pattern transfer onto the SiNx mask. Shorter time results in a SiNx residue which changes the ICP etch and a longer etch starts to attack the InP surface. The color of the sample should be changed back to grey.

1.g) To remove any remaining resist on the etched SiNx nanopillars, the wafer is submerged in acetone for a duration of 24 hours.

Since acetone evaporates rapidly at room temperature, it is crucial to place the wafer in a beaker without a pouring spout and securely seal the beaker with a glass lid. This ensures minimal evaporation of the acetone. After the soaking process, the wafer is rinsed with isopropanol and then blow-dried.

1.h) The resist is then completely removed using an oxygen plasma stripping recipe in the Sentech ICP reactor, with two cycles of 10 minutes each, performed at low and high pressure. Specifically recipe "Plasma Clean Dual Pressure" with temperate input of 75°C and a cycle time of 600 seconds.

1.i) The NRIE etching process can lead to a rough SiNx mask due to the roughness of the resist. To achieve the optimal starting point for the nanowires, it is necessary to smoothen the SiNx mask. This is accomplished by immersing the mask in a 0.1% HF bath for a duration of 1 minute. Not only does this step smoothen the mask, but it also removes any oxide buildup from the previous fabrication step, ensuring a clean surface for subsequent processes.

3.2.3 Etching

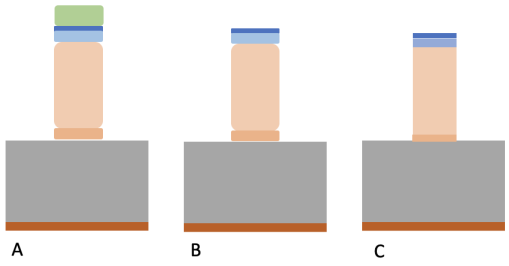

Figure 3.9: Overview of the steps involved in Etching. A) InP etching B) oxygen cleaning and removal of SiNx mask C) digital etching.

2.a) The InP around the SiNx nanopillar is etched away in the Sentech ICP reactor, with the standard recipe of 42 cycles. The SiNx protects the InP material underneath such that only InP material without the mask on top is removed, thus leaving behind InP nanowires with the SiNx mask at the top.

To fabricate the nanowire arrays, the Sentech ICP reactor is used. The substrate is placed in a vacuum chamber, where radiofrequency power is used to generate a high-density plasma. The inductively coupled plasma produces a strong electromagnetic field that efficiently ionizes the reactive gases. The ions and radicals in the plasma chemically react with the substrate, allowing for controlled and precise etching. The standard recipe uses methane-hydrogen chemistry and alternating oxygen cleaning cycles. It is crucial to maintain a constant amount of available material to achieve consistent etch rates. In cases where a full wafer is not being processed, quarter sections of a dummy InP wafer can be employed to supplement the sample, ensuring complete wafer coverage before initiating the etch.
For the current manufacturing process, the standard ICP etch with 42 cycles (recipe: "ICP etch standard") is employed. This recipe yields nanowires with a height of 1950 nm and a tapering angle of 3.9°. To account for potential variations during the etching process, it is important to conduct an etch test on a dummy wafer or include a small piece of a dummy wafer (together with the sample) in the reactor. Following the etching step, the exact height and shape of the nanowires can be verified using SEM imaging on the dummy wafer. Precise knowledge of the nanowire height is essential for subsequent manufacturing steps.
The optimization of this step was carried out by a previous master's student [29]. He modified the parameters of the etching recipe to achieve the optimal shape for the nanowires. However, during the recent maintenance week in the cleanroom, the Sentech reactor was replaced, leading to changes in the specific conditions required for the optimal recipe. Unfortunately, due to time constraints, the recreated optimal recipe has not been developed yet.

2.b) During the etching process, polymers can be deposited on the sample, to remove them an oxygen plasma can be used. Which conveniently can be performed within the Sentech system itself. Thus, the 'Plasma clean dual pressure' recipe is utilized once again, using the same parameters with a temperature of 75°C for a cycle duration of 600 seconds. Hereafter the SiNx mask can be removed, by immersing the wafer in a 10% HF solution for 1 minute, ensuring complete removal, and subsequently soaking it in Ultra Pure Water (UPW) and blow-dried.

2.c) This step is referred to as "digital etching". The digital etching process is aimed at improving the surface smoothness and cleanliness of the nanowires. This involves a controlled oxidation of the nanowire surface (Sentech ICP), followed by the removal of the resulting oxide layer (2 minute bath in 1:10 H3PO4). The entire cycle is repeated three times to achieve optimal results.

To initiate the oxidation, the wafer is placed in the Sentech ICP reactor, utilizing the same oxygen plasma recipe as before. The reactor is set to a temperature of 75°C, and each oxidation cycle lasts for 60 seconds, totaling 7 minutes for each cycle.
After the oxidation step, the resulting oxide layer is removed through a wet-chemical etching process. Two options are available: either a 1% HF solution or a diluted 1:10 H3PO4 (85%) can be used. Each cycle removes around 2 nm of material.
The digital etching procedure is vital for mitigating surface damage caused by the previous etching process, which helps reduce non-radiative surface recombination and minimize losses. By performing three consecutive oxidization-etching steps, the desired improvements in surface quality and performance can be achieved. After all the etching steps the 3x3 nanowire solar cell array should look similar as 3.10.

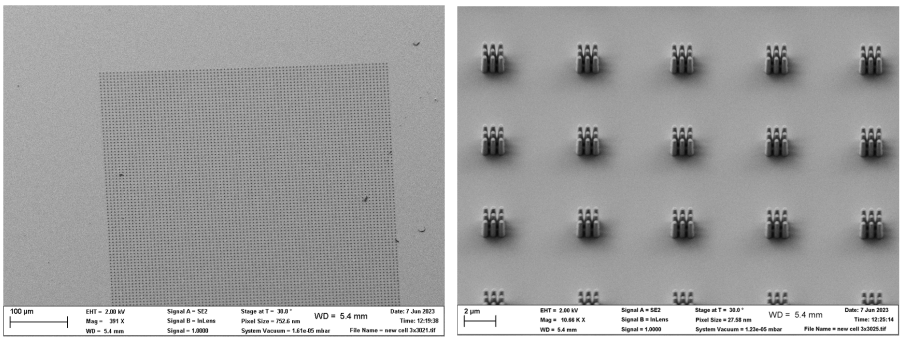

Figure 3.10: SEM image of a 3x3 nanowire solar cell array after the digital etching step 2.c.

3.2.4 Passivation and Back Contact

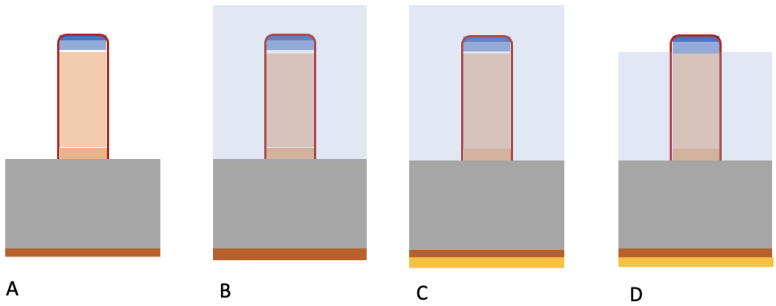

Figure 3.11: Overview of the steps involved in Passivation and Back Contact. A) Deposition of passivation layer (SiOx) B) deposition of BCB C) adding the back contact D) etch the BCB back until the top of the nanowires are free.

3.a) Following the digital etching, a surface passivation layer is applied using an electron beam evaporator to reduce surface recombination. In the current fabrication, a 20nm SiOx layer serves as a passivation layer and at the same time improves adhesion with BCB. The deposition is done in the PECVD.

Normally the passivation layer consist of a deposited 5 nm phosphor-rich POx layer, followed by a 15nm capping layer of Al2O3 to protect the passivation layer. However, due to issues during fabrication, it was chosen to use a SiOx layer as passivation. It is important to again do the preconditioning of 5 minutes and check the deposition rate of SiOx with the reflectometer. The 20 nm deposited SiOx will give the wafer a reddish color.

3.b) In order to provide protection for the nanowires, a thick transparent polymer, BCB-3022-57, is spin coated onto the wafer (4000 rpm for 30 seconds), ensuring complete coverage of the nanowire structures. Before the BCB is applied a adhesion promoter (AP 9000) is spin coated on the sample at 4000rpm for 60 seconds and subsequently baked on the hotplate for 120 seconds at 200°C.

The process begins with a thorough cleaning of the sample using acetone, followed by a rinse with Isopropyl Alcohol (IPA). Hereafter, AP 9000 is spin coated and baked onto the sample.
After the adhesion promoter step, the BCB-3022-57 polymer is applied to the sample. Due to the viscosity of the BCB material, air bubbles may be trapped within the BCB during the deposition process, which eventually leads to a non-planner BCB layer. To prevent this, it is important to keep the pipette submerged in the BCB for a few seconds while drawing it up, ensuring that any air bubbles are not transferred to the pipette and wafer. In the event that air bubbles persist on the wafer surface, an additional attempt can be made to remove them by carefully drawing them up using the pipette.
Before initiating the spinning process, the wafer should be nearly fully covered with the BCB material to achieve the most planar result. By adjusting the spin speed based on the spin curve, it is possible to control the thickness of the resulting layer. For example, spinning the sample at 4000 rpm for 30 seconds typically yields a spacer layer thickness of approximately 4 microns.
Once the spinning is complete, the sample is left undisturbed for approximately one hour. This waiting period allows for the uniform redistribution of the BCB material across the surface of the wafer.
Following the spinning process, the sample is transferred to a vacuum oven for the curing of the BCB material.
The sample is placed inside the oven and subjected to vacuum conditions for a duration of one hour at a temperature of 275°C. To prevent any strain on the sample, a controlled heating and cooling process is implemented. The oven's temperature is gradually increased at a rate of 5°C per minute, ensuring slow and uniform heating using "Luca Recipe". After the curing process, the oven is left to naturally cool down over several hours. Once the cooling process is complete, the nanowires are protected and the sample can be safely flipped and placed on the front side, ready for further processing.

3.c) For the back-contact of the solar cell, a Nickel-Germanium-Gold stack is utilized, with layer thicknesses of 25 nm, 50 nm, and 250 nm, respectively. This stack is deposited onto the sample using an electron beam evaporator, providing an Ohmic back-contact for the solar cell.

3.d) After the deposition of the back contact, the BCB needs to be etched back to achieve the desired thickness, ensuring the n^+-doped layer of the nanowire is exposed.

To determine the initial height of the nanowire, a height measurement is performed using a dummy wafer after the etching process (2.a). The exact thickness of the BCB is then determined using a reflectometer, employing the "ellipsometry BCB on InP" recipe. The recipe is specially made for BCB layers in the past year. Subsequently, the BCB is etched back to the desired thickness using polymer reactive ion etching (P-RIE) with the "50W BCB etch" recipe. This etching process occurs at an approximate rate of 40 nm per minute, the etch rate can be easily checked. It utilizes a 50-watt oxygen plasma in a chamber supplied with a 20:4 sccm O2:CHF3 gas mixture, ensuring precise control over the etching process.

3.2.5 Top Contact

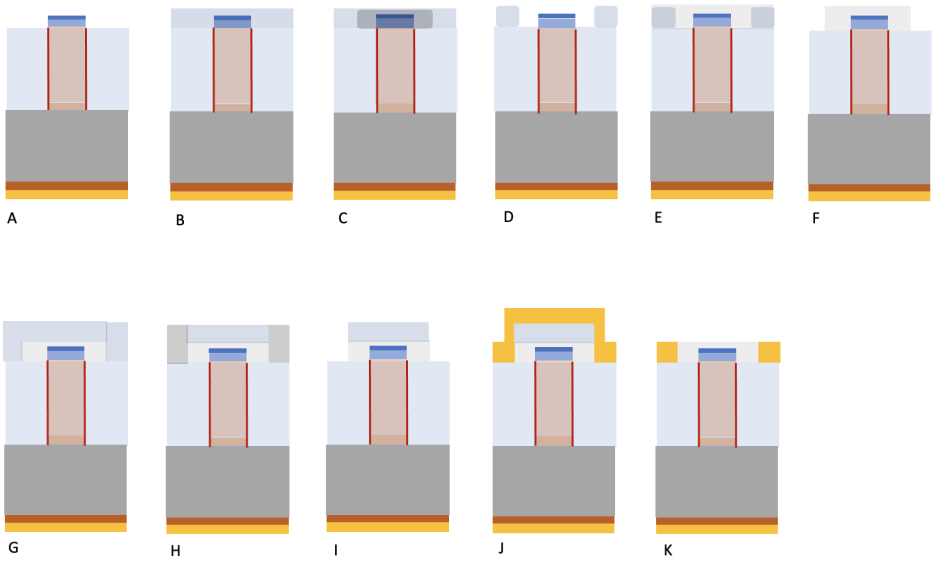

Figure 3.12: Overview of the steps involved in Top Contact A) removal of passivation layer B) adding a layer of PMMA positive resist C) pattering D) development E) ITO deposition F) lift-off of PMMA G) coating in PMMA resist H) pattering I) development J) deposition of gold contact K) lift-off of PMMA.

4.a) The passivation layer (SiOx) on the n^+ region of the nanowires needs to be removed to ensure a conductive contact. This can be achieved by immersing the sample in a 1% HF bath for 30 seconds or in a 10:1 diluted H3PO4 bath for 1 minute. Either of these chemical baths effectively etches away the passivation layer, allowing for direct electrical contact with the nanowires.

4.b) The areas where ITO needs to be deposited are defined using EBL with 950k PMMA A11 resist. The positive resist is spun with 1500 rpm for 30 seconds and baked for 6 minutes at 150°C to evaporate all the solvent. (see figure 3.12B, C)

Before initiating the exposure, it is important to mark the desired areas with markers using an optical microscope since this process involves overlay exposure. In the event of a system crash requiring the sample to be removed and stored, it should be carefully wrapped in aluminum foil to prevent any interaction with the light outside the controlled environment of the cleanroom (outside the "yellow room"). When the markers fail in the normal system, the so-called "Joy" markers can be used. During exposure, the markers can be manually found using the SEM inside the Raith EBPG5150.

4.c) Following exposure, the resist is developed in a 1:3 solution of MIBK:IPA (Methyl isobutyl ketone:isopropyl alcohol) for 35 seconds and then rinsed sequentially in IPA for an additional 35 seconds. Finally, the sample is blow-dried using nitrogen gas 3.12D.

4.d) Subsequently, the top contact layer is deposited, consisting of a 300 nm sputtered Indium Tin Oxide (ITO) layer(3.12E). This is currently done by "Nick Schipper" from the chemical department. Hereafter the PMMA is removed with acetone vapor in a process called "lift-off".

When the ITO layer is in place the sample is placed in acetone vapor, to remove the PMMA resist underneath the ITO, thus creating a patter in the ITO layer. The sample is placed in a holder inside a beaker with a small amount of acetone. The beaker is closed such that the acetone vapor stays inside the beaker. After a 2 hour acetone vapor bath the sample is rinsed in acetone and IPA. During the rinsing pressure needs to be applied on the sample with the acetone and IPA stream. This pressure method effectively removes the PMMA flakes 3.12F.

4.e) To establish contact with the ITO layer, a Nickel-Germanium-Gold (25/50/250 nm) contact border is deposited on top using electron beam evaporation. The same optical lithography procedure employed for the gold contacting layer is utilized for this step. (3.12G-K).

4.f) Following the deposition of the top-contact layer, a rapid thermal annealing process is conducted at 250°C. Once this step is completed, the fabrication of the solar cell is concluded. Figure 3.13 visually represents the final outcome of the fabrication process.

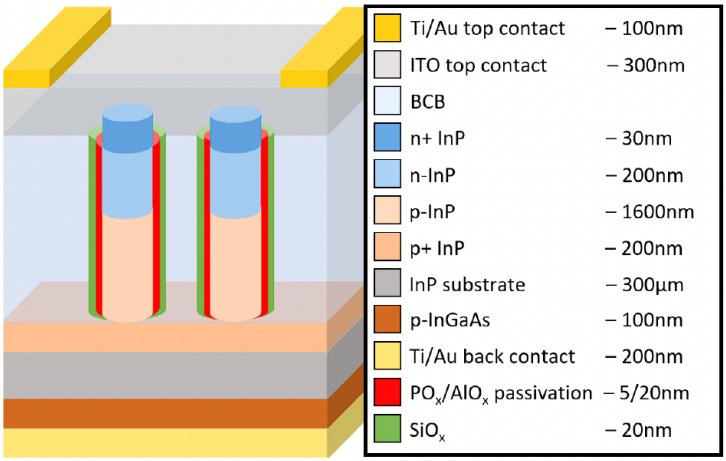

Figure 3.13: Schematic depiction of a fully assembled nanowire solar cell, illustrating the individual layers along with their corresponding thicknesses.

3.2.6 Micro lenses

This particular step has been optimized by a previous master student [12].

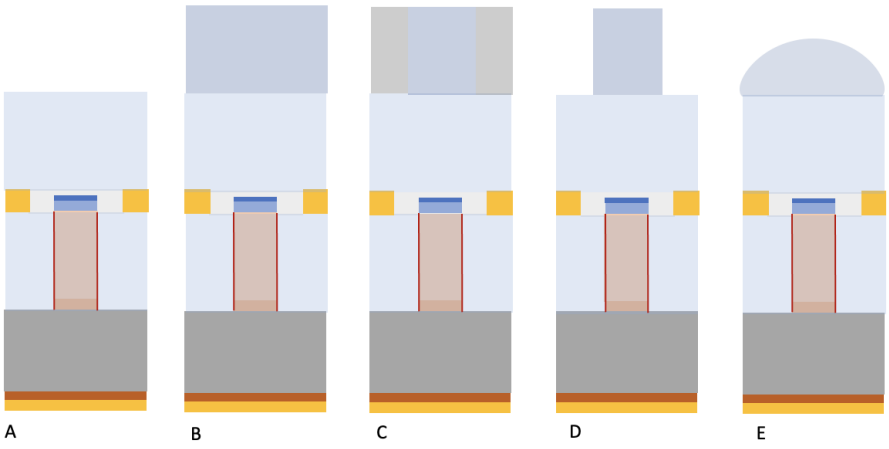

Figure 3.14: Overview of the step taken in Micro Lenses. A) Adding BCB spacing layer B) PMMA resist layer C) pattering D) development E) thermal reflow.

5.a) The solar cell undergoes a cleaning process by rinsing it with IPA, hereafter the cell is coated with an adhesion promoter AP9000 which is applied with a spin speed of 4000 rpm for 60 seconds and baked for 120 seconds at a temperature of 200°C. The BCB spacing layer is thereafter applied, which is spun at 3000rpm for 60 seconds. The layer acts as a spacing layer to ensure proper alignment of the micro lenses with the top surface of the nanowires.

Before curing the BCB in the vacuum oven, the sample should rest for a minimum of an hour, to ensure an even distribution of BCB material which results in a more planner spacing layer.
The spacing layer ensures proper alignment of the micro lenses focuses point with the top surface of the nanowires. To get the necessary height the BCB height needs to be measured and if needed to be etched back, it was shown previously [12] that for 6-micron lenses, a 3-micron thick spacing layer is needed.

5.b) Spin coat the resist 950K PMMA A11 onto the sample at a speed of 1500 rpm for 30 seconds. The resist is then baked for 6 minutes at 150°C

5.c) After baking, the sample is placed inside the RAITH EBPG 5150 machine for the electron beam lithography step. During exposure, a $100kV$ electron beam is used to expose the sample with a dose of approximately $900\frac{\mu C}{cm^2}$.

Cylindrical pillars are created to form the lenses, and the resist that needs to be removed is exposed due to the positive nature of the resist. It is important to do a dose check before doing the real exposure. The alignment in this step is crucial and needs to be done with care. When the system fails to detect the markers, Joy markers can be utilized and the markers can be found manually.

5.d) Following exposure, the resist undergoes development using a 1:3 mixture of MIBK and IPA for 35 seconds. Subsequently, it is rinsed in IPA for an additional 35 seconds. Finally, the sample is dried using nitrogen gas.

5.e) The lenses are generated by thermally reflowing the remaining cylindrical resist pillars. To create 6-micron diameter lenses, the sample is slowly heated from 20°C to 125°C over around 15 minutes at 40% power of the hotplate. This gradual heating ensures even melting of the resist. Afterward, the sample is held at 125°C for 3 minutes and 45 seconds to achieve spherical micro lenses.

Chapter 4

Results

4.1 Solar Simulator

Two different samples are measured with the solar simulator setup. A sample consists of an array of 7x7 smaller cells, where the cells are labeled as seen in figure 4.1. The smaller cells have an area of 1000x1000μm. To create an ohmic contact, thin, fully reflective Nickel-Germanium-Gold layers (also referred to as the gold contact) are deposited on the outer edge of the solar cells, leaving only an active solar cell area of 500x500μm. The first solar cell that was measured was a full array nanowire solar cell named "SG02". The second solar cell that was measured was a 3x3 array solar cell called "SQ03". Both cells were measured before lens placement, due to time contain it was not possible to measure cell SQ03 with lenses on top. After the submission of the report, the fabrication continues such that also measurements can be performed with micro lenses on top.

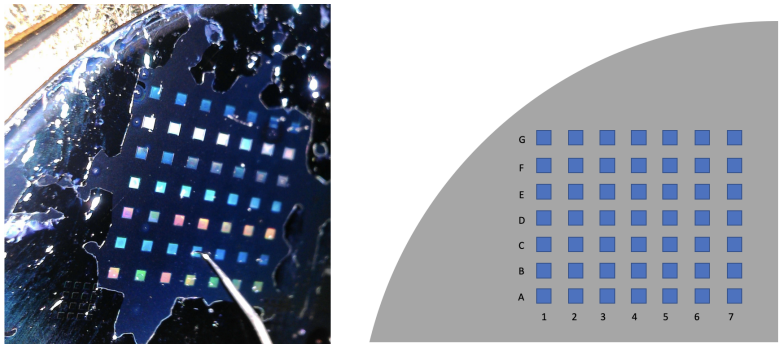

Figure 4.1: Labeling of the solar cells.

4.1.1 I-V Curves

The I-V curves for cell SG02 full array solar cell are shown in figure 4.2 and the corresponding short circuit current density and open circuit voltage can be seen in the table 4.1. In the next section, a more in-depth review is given of this cell related to different excitation power. This measurement can be used to roughly identify the excitation power from the laser which corresponds with 1 sun by matching the V_{oc}. It is worth mentioning that during the I-V curve measurements, the contact pin is pressing on the top contact, slightly damaging the top contact of the cell and casting a small shadow on the active area, thus reducing the measured values and the reproducibility of the experiment itself.

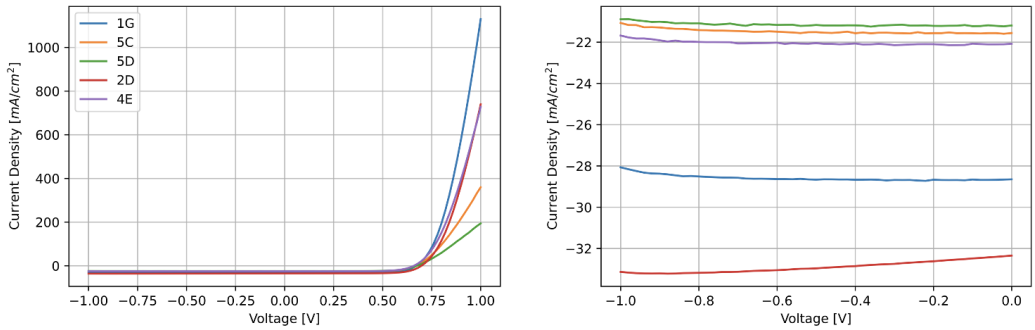

Figure 4.2: I-V curves of different full array cells (SG02), measured in the solar simulator setup.

Cell	J_{sc} $[mA/cm^2]$	V_{oc} [V]
1G	28.32	0.672
2D	32.61	0.697
4E	21.85	0.658
5C	21.24	0.668
5D	21.01	0.675

Table 4.1: The measured short circuit current and open circuit voltage of fully array nanowire solar cells (SG02).

As expected the 3x3 array has a lower current as the full array. This is because no lenses are present on top of the nanowires. There are gaps between the nanowires that are not actively converting the sunlight into current. The effective area of the solar cell is lower than in the full array case. The pitch between the nanowires is $500nm$ and the diameter is 200nm, while the pitch between the 3x3 arrays is $6\mu m$. The total area of the nanowires is thus $(3*200nm+2*500nm)^2 = 1.6\mu m^2$ while the corresponding area of the full array is $6\mu m^2$. This gives an approximate ratio of $6^2/1.6^2 \approx 14$. However, we can not immediately say that the effective area is decreased by this ratio, because the nanowires have a larger effective absorption area than their real dimensions, due to the antenna effect of the wires. Nonetheless, it provides an estimation. It should also be noted that the shape and dimensions of the nanowires themselves are different for both solar cells.

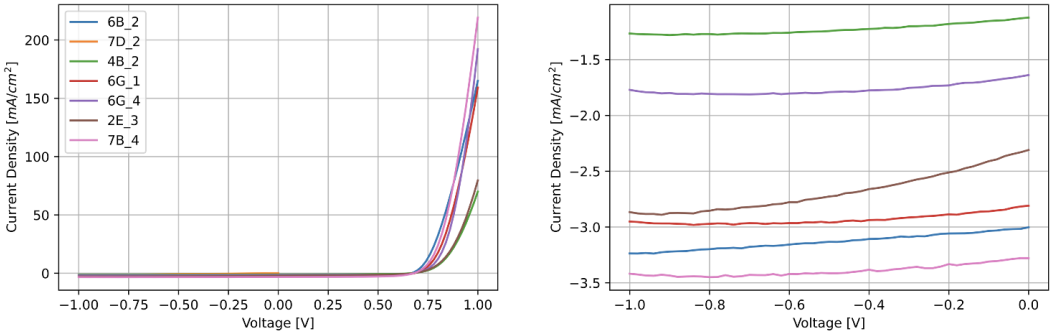

Figure 4.3: I-V curves of different 3x3 array cells (SQ03), measured in the solar simulator setup.

Cell	J_{sc} $[mA/cm^2]$	V_{oc} [V]
6G_1	2.79	0.681
4B_2	1.11	0.668
6B_2	2.99	0.670
7D_2	1.57	0.672
2E_3	2.46	0.676
6G_4	1.62	0.674
7B_4	3.25	0.678

Table 4.2: The measured short circuit current and open circuit voltage of fully array nanowire solar cells (SG02).

4.2 Excitation Power Dependence

4.2.1 I-V Curves

To further investigate the nanowire solar cells the I-V curves were measured at different excitation and the corresponding ideality factor and dark saturation current were fitted through the data. Furthermore, the fill factor and the efficiency were plotted against excitation.
Different cells were excited with the 532nm continuous wave laser at different excitation powers and the I-V curves were measured. In plot 4.4 the I-V curves measured at different excitation are shown for full array cell 2D, with the corresponding fit. Note that the current is measured negatively due to the experimental setup. For the fit through the data, the following function was used:

$$I = I_{ph} - I_0(e^{\frac{qV}{nk_bT}} - 1)$$

In this equation are two unknowns which are calculated with the fit through the data.

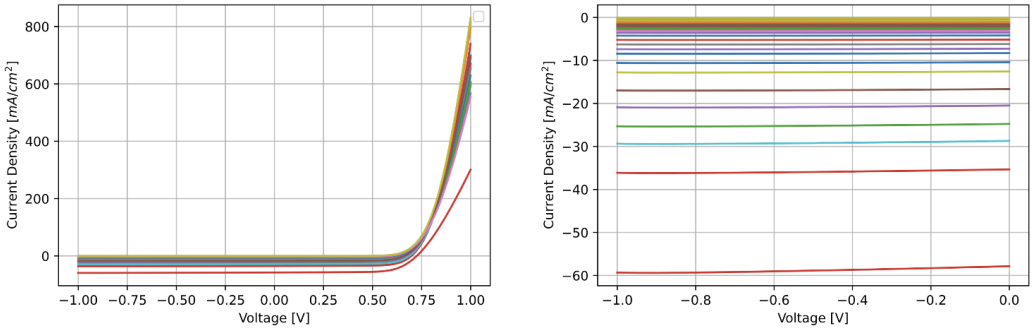

Figure 4.4: I-V curves for cell SG02-2D measured at different excitation powers, ranging from 10 to 1400 μW.

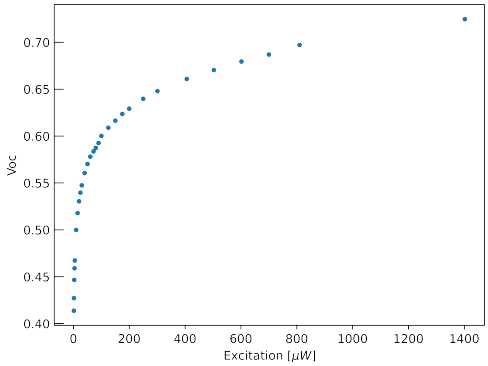

Figure 4.5: Measured open circuit voltage at different excitation powers for cell SG02-2D.

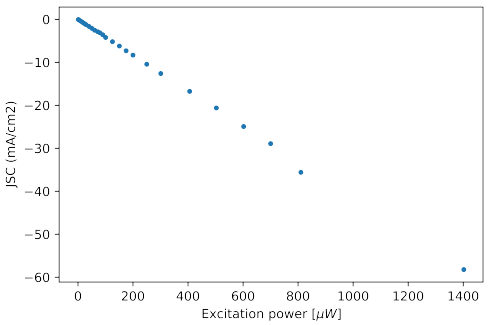

Figure 4.6: Measured short circuit current at different excitation powers for cell SG02-2D.

The measured open circuit voltage increases logarithmically at increasing excitation power, as expected from the thermodynamic analysis on open circuit voltage. In the next section the photoluminescence efficiency is extracted from this data. The short circuit current increases linearly with higher excitation power.
It was observed that the ideality factor and the dark saturation current had the same shape for the different cells when measured at different excitation powers. It was also observed that the ideality and dark saturation current for the different cells had different shapes, as can be seen from figures 4.7 and 4.8. In the literature, similar graphs are found as 4.7[66] for silicon solar cells. At low excitation (corresponding to low voltage across the cell), the ideality factor is governed by shunt paths across the p-n junction. At intermediate voltages, the ideality factor is "stable", and at high voltages (irradiance levels), it is governed by series resistances. Where the linear increasing ideality factor at low excitation is governed by shunt resistance and hereafter stabilizes and slowly increases with increasing excitation power. It is worth noting that the ideality factor is high compared to conventional solar cells. This is probably due to no optimal connection between the nanowire solar cell array and the contacts, increasing the series resistance. Most likely the connection issue is between the top of the nanowire and the conductive ITO layer as this has been seen before in the AND group. The similar shape of the dark saturation current and ideality factor suggests that both parameters are influenced by a common underlying factor or mechanism that varies with excitation power.

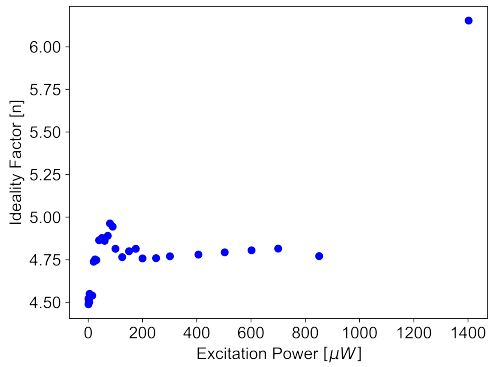

Figure 4.7: Ideality factor calculated for different excitation powers for cell SG02-2D.

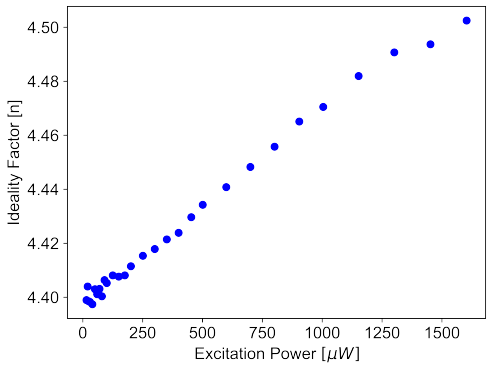

Figure 4.8: Ideality factor calculated for different excitation powers for cell SG02-4E.

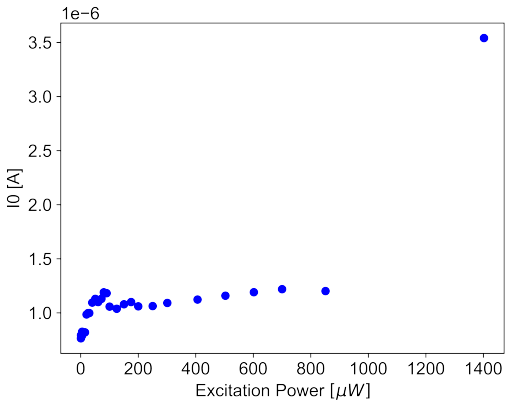

Figure 4.9: Dark saturation current calculated for different excitation powers for cell SG02-2D.

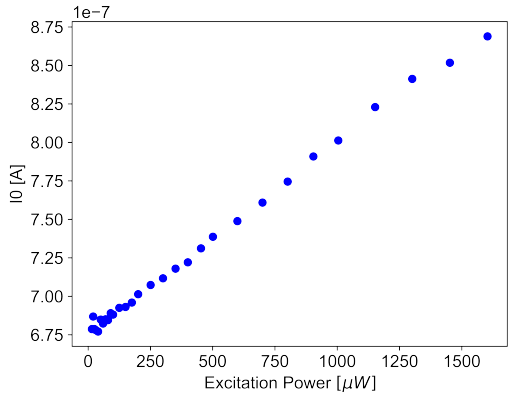

Figure 4.10: Dark saturation current calculated for different excitation powers for cell SG02-4E.

When the fill factor and maximum power point efficiency are plotted against excitation we see a logarithmic increase 4.11, 4.12. This comes from the logarithmic increase of the V_{oc} and linearly increasing I_{sc} with excitation. However, as mentioned before in section 2.1.3 the fill factor and thus the maximum power point also depends on the shunt and series resistance. At different excitation, the voltage and current increase, and thus the resistances change accordingly. The logarithmic increase is thus not fully

determined by the logarithmic increase in open circuit voltage due to other factors at play (e.g. different recombination mechanisms, diode quality, contacts, etc).

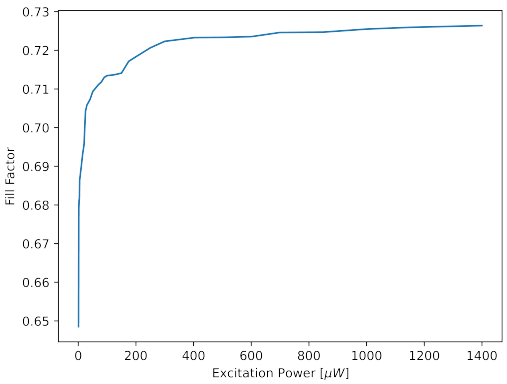

Figure 4.11: Fill factor measured at different excitation power for cell SG02-4E.

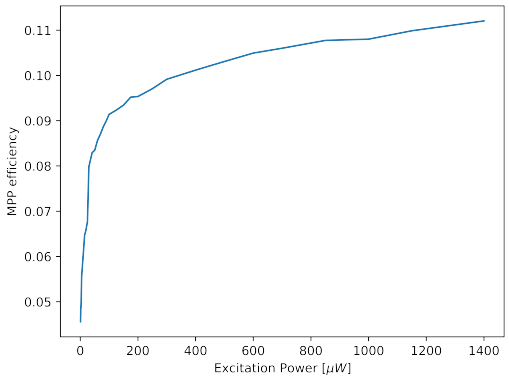

Figure 4.12: Maximum power point efficiency measured at different excitation power for cell SG02-4E.

4.2.2 Photoluminescence Measurement

The principle of photoluminescence (PL) was discussed in section 2.4, here it was argued that at high excitation power, the radiative limit is reached ($\eta_{ext}^{PL} = 1$), this means that in equation 2.26, the entropy loss term related to photoluminescence efficiency will be zero, increasing the V_{oc}. According to the derivation from the power law relation in 2.4 the beta factor should be between $1 \leq \beta \leq 2$, indicating how the PL efficiency increases due to excitation.
To examine this, a series of samples with full nanowire arrays were tested. The samples were excited using a power range of 10 to 1600μW with a 532nm continuous wave laser, corresponding to an illumination intensity of approximately 0.2 to 2.5 suns. In figure 4.15 the integrated photoluminescence (PL) of cell "2D" is shown which is measured against excitation power. The integrated PL spectrum was measured in a spectrometer, first, the PL counts of a dark measurement were subtracted per wavelength, hereafter the wavelengths below 800nm and above 1000nm were removed, it is expected to have a PL peak around 920nm which corresponds with the bandgap of InP.
The actual PL spectrum is higher than the measured PL spectrum due to the limitations of the numerical aperture (NA) of the collecting lens as can be seen in figure 4.13. Due to this, the actual PL efficiency can only be estimated when correcting for the NA. In the experiment, no NA correction is done. However, it is still observed how the PL efficiency increases against excitation power, assuming the PL increases the same for each emitted photon angle from the nanowire.

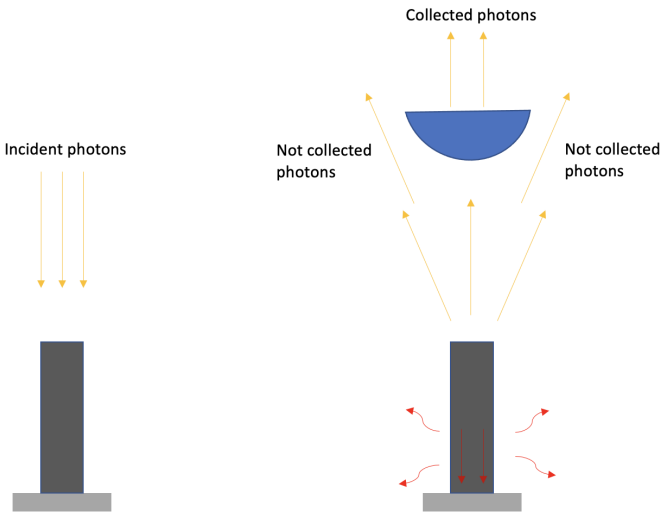

Figure 4.13: Schematic picture of the PL setup, where it can be seen that not all emitted photons are collected.

The data was fitted with equation 2.11 for several cells and gave the power law relation as shown in the table 4.3. Where the power-law relation is given as ax^{β}, with a an experimental constant.

Cell	Power Law	β
1G	$154.5x^{1.083}$	1.083
2D	$80.4x^{1.371}$	1.371
4E	$106.3x^{1.113}$	1.113
5D	$124.2x^{1.079}$	1.079

Table 4.3: Power law and β values for different cells, determined by measuring under different excitation powers.

The β factor, suggests that the solar cell is in the radiative limit, however, this is not the case. It is expected to see a β factor around 2 for low-intensity powers. The mismatch between the expected and measured power law indicates other phenomena at play such that the observed increment of radiative recombination is linear while the apparent increment of radiative recombination is higher. A possible explanation is that the recombination of charge carriers happens mostly in the n-doped or p-doped regions before being separated by the built-in electric field [67], the P-N junction is not yet enough forward-biased. In other words, the bands of the junction are not yet flat enough to properly emit light, and see the clear distinction between radiative and non-radiative recombination. This observation/model is not yet implemented and should be investigated further.
Experimental findings revealed that the photoluminescence (PL) of the material surrounding the solar cells exhibited a higher integrated PL spectrum. When the solar cell was excited with the laser it was observed that the laser spot was slightly larger than the solar cell itself, thus also illuminating the surrounding areas. As a result, the measurement captured the PL of the surrounding material as well, leading to an apparent increase in the measured PL efficiency. During the experiment, the cells were manually moved, resulting in variations in their orientations during measurements. As a consequence, each cell was measured with a slightly different configuration, leading to varying levels of error in the measured PL arising from the surrounding material. However, these inaccuracies are expected to be small, due to a small illuminated area around the cell itself.

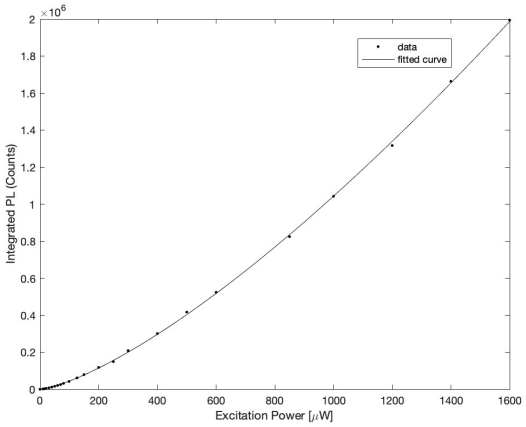

Figure 4.14: Measured integrated PL intensity at varying excitation powers.

4.2.3 Photoluminescence Efficiency

The IV curves of the same cells were measured against excitation power. Equation 2.10, was rewritten in the following form:

$$V_{oc}(x) = 1.037 - \frac{k_b T_0}{q} \left| \ln \left(\eta_{ext}^{PL}(x) \right) \right| \tag{4.1}$$

Where the constant $V_{oc}^{rad} = 1.037V$ is used for InP solar cells[8] [68]. The excitation was done with a laser of 532nm. The measured V_{oc} can be linked with the V_{oc} measured at the solar simulator experiment, this can be used to estimate the laser excitation corresponding to 1 sun excitation. The η_{ext}^{PL} is calculated as:

$$\eta_{ext}^{PL} = e^{-\frac{1.037 - V_{oc}}{V_t}} \tag{4.2}$$

With $V_t = \frac{k_b T_0}{q} \approx 25.69mV$. The $-$ sign in the exponent comes from the absolute brackets and makes sure that the efficiency is between 0 and 1. In table 4.4 the exponent from the power law relation of the η_{ext}^{PL} is shown.

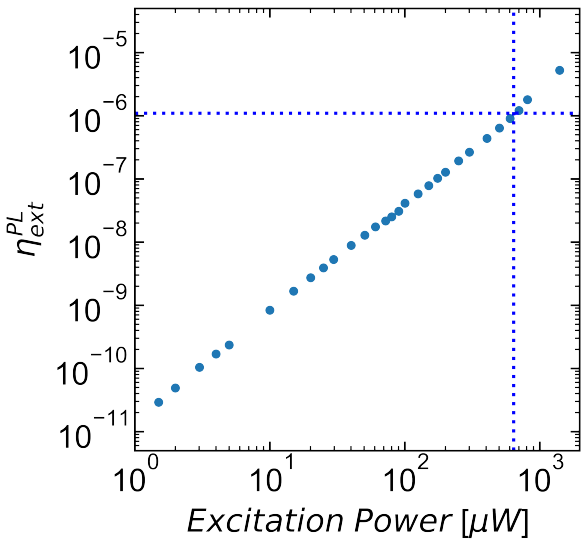

Figure 4.15: η_{ext}^{PL} calculated from the measured V_{oc}. The η_{ext}^{PL} corresponding to one sun illumination is highlighted.

Cell	$(\beta - 1)$ 4.2	β PL
1G	1.683	1.083
2D	2.006	1.371
4E	2.138	1.113
5D	1.761	1.079

Table 4.4: β values for different cells, determined by the different equations and PL.

It is interesting to see that the calculated exponent in the power law is higher than the measured one obtained with the PL experiment. The beta factor is around 3 and higher than expected when non-radiative is dominant, this can possibly be explained due to the contribution of the contact resistances in the experimental setup and/or suggesting other phenomena at play related to excitation power. This should be investigated further

Chapter 5

Cost Analysis

This chapter examines the cost analysis of large-scale production of 4-inch nanowire solar cells with micro lenses. Each nanowire is positioned beneath a microlens measuring 6x6 microns. The cost analysis follows NREL's bottom-up approach and utilizes data from previous NREL research [69][70][71][72], as well as input from suppliers and cleanroom personnel (CRP) including Marc Sellschopp (Oxford Instruments), Robert Eichinger-Heue (EVG Group), Patrick Bax (CRP), Erik Jan Geluk (CRP), and Frank Dirne (CRP). The specific data obtained during interviews were mostly given as an indication or a range of values and not as one specific value. In this analysis, the most conservative values were used that were obtained during the interviews. To calculations are performed in Excel and can be found in the supplementary of the thesis.
The analysis considers three production volumes: a small-scale production of 250,000 solar cells per year, a large-scale production of 1,000,000 solar cells per year in a self-owned facility, and an additional production of 1,500 solar cells per year in an external facility with an efficiency of 33%. The calculated cost is expressed in €/W where the total produced Watt is calculated by multiplying the efficiency by STC and the total effective area of the produced solar cells. The analysis incorporates certain simplifications and assumptions, such as assuming full capacity utilization, the purchase of new equipment and facilities without depreciation, and already obtained licenses.
First, a possible production method is explained. Hereafter, the cost components are divided into Capital Expenditure (CAPEX) and Operational Expenditure (OPEX). The situation where production is located in an external facility is described separately. Lastly, a balance of system (BOS) is added to estimate the Levelized Cost of Energy (LCOE).

5.1 Production Method

The production process consists of two distinct manufacturing stages. The first stage involves the production of nanowire solar cells, which are subsequently topped with micro lenses. Figures 5.1 and 5.2 illustrate a potential manufacturing flow for InP nanowire solar cells on a Cz-Si substrate and micro lenses. The production method is designed with the goal of achieving larger-scale production and is based on literature sources from NREL and existing production methods. However, it has not been demonstrated that this production method yields high-quality nanowire solar cells. The production process is assumed to be optimized.

Nanowire Solar Cell

Substrate Preparation and Cleaning
To remove the native oxide and clean the substrate, the wafer is placed in a bath of 10 % diluted H_3PO_4 for 4 minutes and rinsed in water. Hereafter a deposition of $400nm$ thick silicon nitride (SiNx) is placed on top to further prevent oxide formation on the substrate. This layer serves as a hard mask during the subsequent patterning steps. Deposition methods for SiNx include plasma-enhanced chemical vapor deposition (PECVD) in a PlasmaPro 800 PECVD machine. This manufacturing step is represented in step 1 in figure 5.1.

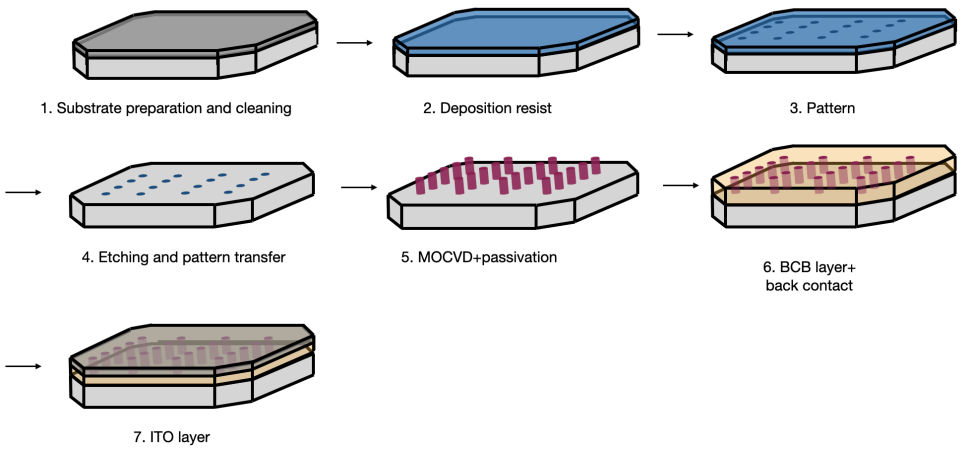

Figure 5.1: Process flow for the production of InP nanowire solar cell on a Cz-Si substrate.

Patterning
After the SiNx layer, the resist is deposited onto the substrate (step 2). The resist-coated substrate is then brought into contact with a template or mold that has the desired nanowire pattern. The template is typically made of a hard material such as quartz or silicon and is coated with a release layer to prevent sticking. The template is pressed gently into the resist layer, causing it to flow and conform to the pattern of the template. Once the resist has been imprinted with the desired pattern, the template is separated from the substrate. The resist pattern is then cured or hardened, typically by exposure to UV light, to make it more durable and resistant to subsequent processing steps. This step is known as the hard imprint (step 3). Steps 2 and 3 are done in the HERCULES NIL system where a production rate is scaleable to 300 wafers per hour. (It is also possible to do it in a cheaper system EVG7300 where the maximum production rate is 80 wafers per hour, however, spin coating needs to be done manually).

Etching and pattern transfer
The resist and SiNx layer is then etched using the PlasmaPro 100 Cobra ICP RIE Etch and a wet etching/cleaning process (acetone bath) to transfer the resist pattern onto the underlying silicon substrate in step 4. The pattern in the form of trenches is left behind on the substrate that will act as the starting point for the growth of the InP nanowires.

Nanowire growth and passivation layer
The patterned substrate is then ready for the growth of InP nanowires. This can be accomplished using a variety of techniques, such as metalorganic chemical vapor deposition (MOCVD) or molecular beam epitaxy (MBE), which can use vapor-liquid-solid (VLS) growth. In this production, MOCVD is chosen where the nanowires are grown with the help of droplets of a catalyst (mostly gold)[73]. When the nanowires are grown a Al_2O_3/PO_x layer is deposited using sputtering techniques, to act as a passivation layer as shown in step 5.

Spacing layer and back contact
In step 6 of the process, a BCB 3022-57 layer is spin-coated onto the sample, ensuring that only the top of the nanowires protrudes from the BCB layer. Subsequently, the sample is cured in a vacuum oven, a step carried out in the wafer track. Following this, a thermal evaporation process is employed to deposit a metal back contact consisting of aluminum, with a thickness of $300nm$.

Top contact
In step 7 the Indium tin oxide (ITO) layer is sputtered on the top of the nanowire. The ITO layer will act as the top contact.

Micro Lenses

Spacing and resist layer
The fabrication process starts with cleaning the sample using an acetone rinse followed by an IPA rinse. After cleaning, an adhesion promoter AP 9000 is spun onto the sample using a spinner, and baked on a

hotplate. Then, BCB 3022-57 is spun onto the sample to create a transparent polymer spacer layer with a thickness of approximately 4 microns. The sample is baked in a vacuum oven. This curing step is done slowly to prevent the formation of strain. These steps can be automated by using the wafer track.

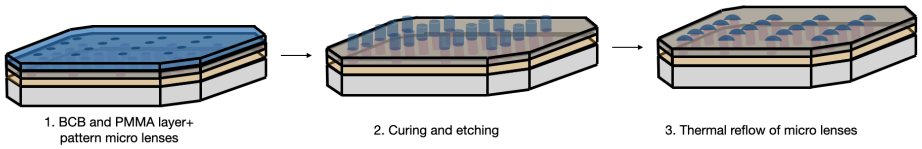

Figure 5.2: Process flow for the production of micro lenses on top of the InP nanowire solar cells.

Patterning
To create micro lenses with a diameter of approximately 6 micrometers, a 950K PMMA A11 resist is spun onto the sample and cured, resulting in a resist layer thickness of around 3.4 micrometers. After baking, the pattern is made with nanoimprint such that the whole surface can be exposed at one time, which is done by the HERCULES NIL system. The sample is put in a developer (MIBK:IPA), to remove the surplus of PMMA.

Thermal reflow
After the patterning, the sample is heated slowly from 20°C to 125°C on a hotplate to ensure uniform melting of the resist to form spherical micro lenses. The thermal reflow process enables the creation of large micro lenses with a diameter of approximately 6 micrometers.

5.2 Capital Expenditure

Capital Expenditure (CAPEX) is a crucial aspect of financial planning and investment for businesses. It represents the funds allocated to acquiring, upgrading, or expanding physical assets such as property, equipment, and infrastructure. CAPEX investments are typically long-term and aim to enhance a company's capabilities, support growth, and generate future benefits. These expenditures are recorded as assets on the balance sheet and depreciated over time. Evaluating CAPEX projects involves analyzing financial metrics to assess their profitability and aligning expenditures with the company's overall strategy. Effective management of CAPEX is vital for companies to maintain competitiveness, optimize operations, and drive sustainable growth.

Machine Cost

The depreciation cost is assumed to be a straight-line depreciation. When no scrap value is found it is assumed to be €0. In the case of producing in an external facility, no machines are bought. The same machines are bought for both production volumes, however, the total number of machines differs and is calculated with the production rate of each machine. It should be noted that the market offers a wide array of machines. For the purpose of this cost analysis, the machines recommended by EVG Group and Oxford Instruments have been selected. Nevertheless, it is worth mentioning that alternative setups and machines are available.

MOCVD
As of November 2008, the cost of an MOCVD (Metalorganic Chemical Vapor Deposition) tool, including shipment and installation, was approximately 2.8 million dollars [70]. By April 2023, the net present value of the same tool increased to 3.1 million euros. The estimated scrap value of the tool is around €500 000, and its expected lifetime is 10 years. The MOCVD tool has a capacity of 25 4-inch wafers per batch, with a total operational time per batch of 35 minutes, where there is a total loading and unloading time of 10 minutes, 10 minutes annealing step, and 8 minutes cooling step before the wafers enter the growth reactor [74][75]. Only one machine is required for both production volumes. The annealing and cooling are done in a wafer track such that the MOCVD can be optimally used.

RF DC Sputtering
This machine cost around €460 000. The lifespan is around 15 years, no scrap value has been found and is assumed to be zero. There are cheaper variants for sale, however, it has to coop with the production volume, for the small production volume only one machine is necessary whereas for the large production volume 2 machines are needed. The capacity is 25 wafers per batch with an operational time per batch of 15 minutes. The data was obtained from the interviews (Oxford Instruments).

Wafer track
Typically, a wafer track consists of a series of interconnected modules or stations that perform specific tasks. The wafers are loaded onto cassettes or carriers and are transported through the track using a combination of robotic arms, conveyors, and advanced handling mechanisms. The system ensures precise positioning and alignment of wafers during each process step. The HERCULES NIL has also a build in wafer track that can spin coat and cure the resist for the nanoimprint steps. However, two additional wafer tracks are needed, one for adding the back contact, BCB, and ITO layer and one for the annealing and cooling step in the MOCVD. Additionally, two more wafer tracks can be added for the wafer preparation and one for the etching and thermal reflow to create the micro lenses. The machines used in the wafer track consist of the vacuum oven, hotplates, cooling racks, spinners, polymer etching, DC sputtering, conveyor belt, and robotic arms. The two wafers tracks are not considered to be "difficult" and Frank Dirne estimated the cost to be around €400 000, excluding the machine cost. However, the real price needs to be estimated by a professional company.

HERCULES NIL
The HERCULES NIL system from the EVG group is chosen for the nanoimprint step, which has a maximal production volume of 300 wafers/h. The price of the system depends on the features, this system would come with automatic coating, plasma oxygen cleaning, solvent processes, and resin curing inside, as well as cassette-to-cassette handling. The machine would require two masters (molds) one for the nanowires and one for the micro lenses. After contact with the EVG group, a price of 2.8 million euros was estimated including shipping and installation. The lifetime and scrap value are estimated to be 12 years and €400 000, respectively. Only one machine is needed for both production volumes.

PlasmaPro 100 Cobra ICP RIE Etch
The price was established after contact with the company Oxford Instruments to be between €150 000-€200 000 per machine with a capacity of 20 wafers per batch and a production rate of 40 minutes per batch. No scrap value and a lifetime of 7 years were found. For small-scale production, 1 machine is necessary, whereas 4 are necessary for large-scale production volume.

FlexAL ALD
The price was set at €150 000 by Oxford Instruments, it was advised to get 1 machine for the small production and 3 machines for the larger production chain with a capacity of 25 wafers per batch and a production rate of 34 minutes per batch. The lifetime was estimated to be 10 years.

PlasmaPro 800 PECVD
The price was estimated to be €250 000. No rest value has been found. the lifetime is around 8 years and 1 is needed for the small production while 3 are needed for the large production volume. The capacity is 25 wafers per batch with a production rate of 28 minutes per batch.

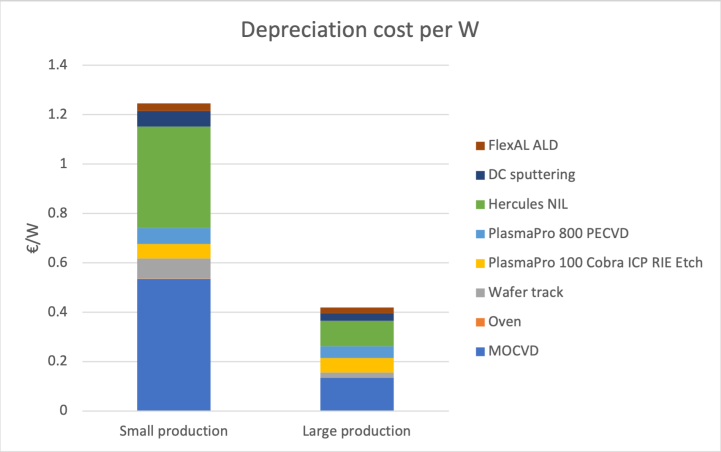

Figure 5.3: Depreciation cost for small and large production volumes in self owned facility.

The total depreciation cost for the two different production volumes is shown in figure 5.3. The large difference comes from the cost of the MOCVD and the HERCULES NIL. These machines are essential for production. There is a possibility of buying cheaper alternatives for the low production volumes, however, no reliable information on the pricing of the alternatives was found.

Cleanroom

The price for building a cleanroom can vary depending on the type of cleanroom needed. For the production of the nanowire solar cells, a type 2 (ISO 5) cleanroom is chosen. The price is estimated to be €$3000/m^2$ [76]. This price is the average price per $/m^2$ as built by the company Mecart. The price can differ depending on what the specific needs are. For the small production volume $500m^2$ is needed whereas the large production volume needs an area of $800m^2$. The lab needs to be filled with the basic lab components. The cost for this was estimated to be €300 000 and €500 000 for the small and large production volumes, respectively. The basic lab components include wet benches, clothing, beakers, pipets, etc. This price was estimated on previously build cleanrooms. The total cost of the cleanroom and basic lab equipment is around 9% of the total CAPEX cost.

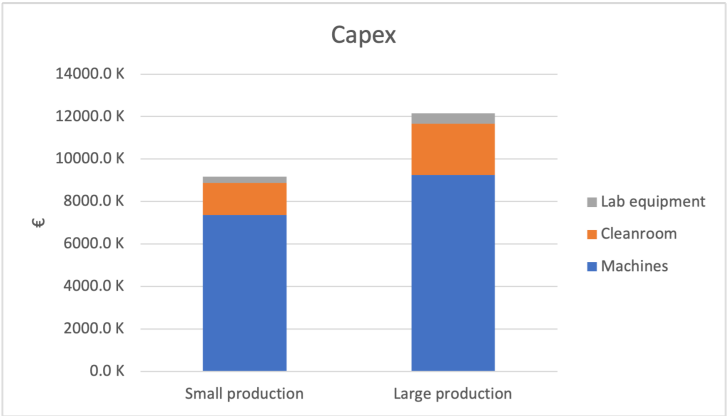

Figure 5.4: Different CAPEX components.

In figure 5.4 the different CAPEX components can be seen. The majority of the CAPEX is made up of the total machine cost. As can be seen from the figure €9 176 000 and €12 160 000 is needed to get the small and large production running, respectively.

5.3 Operating Expenditure

Operating Expenditure (OPEX) represents the day-to-day expenses incurred by a business to maintain its ongoing operations. These expenses include costs related to salaries, utilities, rent, maintenance,

marketing, and administrative activities. Unlike CAPEX, which focuses on long-term investments in physical assets, OPEX is recurring and necessary for the regular functioning of the business. OPEX is recorded as expenses on the income statement and directly impacts the company's profitability. Effective management of OPEX involves optimizing costs, improving efficiency, and maintaining a balance between operational needs and financial sustainability. Understanding and controlling OPEX is vital for businesses to maintain profitability, support ongoing operations, and allocate resources efficiently. The OPEX is expressed as €/W.

Labor Cost

The total labor time is calculated for each of the processes considering the machine loading time. For both processes, it is assumed that 1 more full-time employee (40h per week) is needed for administrative purposes. This gives an approximation for the total labor time, however, now we are ignoring other labor consuming work around the fabrication. When using more wafer tracks less labor time is needed. For the small production, 5 full-time employees are needed whereas, for the large scale production, 14 employees are needed. It is assumed that some of the employees are able to perform maintenance and repairs on the machines. The employees are getting paid €36 000 gross per year. An employer in the Netherlands also needs to consider vacation money, insurances, and income-related contribution (ZVW) [77]. For the sector of semiconductor and solar cell production, the total cost for the company per employee is €47 207 per year.

Consumables

For the production certain chemicals are needed, which are not part of the solar cell itself. Such as Phosphoric Acid (H3PO4) used for removing oxidation, Ultrapure water to rinse the cell, or resist materials for the nanoimprint step. The consumables are listed in figure 5.5. Here it is assumed that the same chemicals are used as in the current production process. The majority of the cost comes from ultra-pure water and H3PO4.

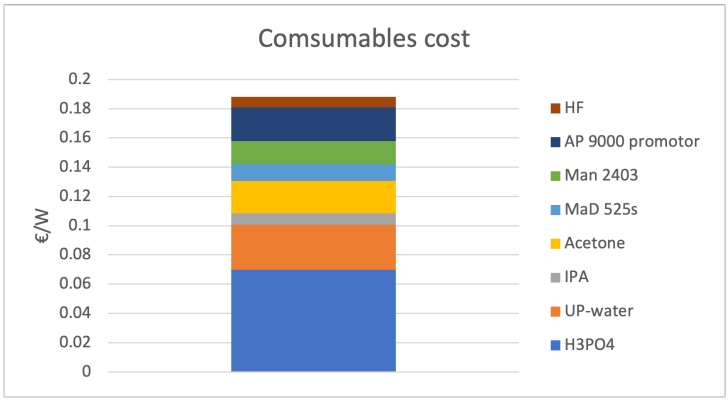

Figure 5.5: OPEX for chemicals used in the production of nanowire solar cells.

Materials

The materials used for the solar cell consist of trimethylindium (TMLn) and Phosphine (PH3) for the InP nanowire growth, ITO for the front contact, Aluminium oxide (AL2O3) and Phosphorus oxide (POx) for the passivation layer, Aluminium (Al) for the back contact, PMMA for the micro lenses, Benzocyclobutene (BCB 3022-57) as a spacing layer and Cz-Si as the wafer.
For the growth of InP nanowires, the MOCVD makes use of the reaction: TMIn+PH3→InP+byproducts. The total usage of input parameters can be calculated taking into account a V/III material ratio of 30 (specific growth condition), a material utilization rate of 60 %, a nanowire diameter is 200nm, and a height of 2030 nm.
The ITO usage is calculated with a material efficiency of 60% for a uniform thin layer of 300nm thick.
The passivation layer is calculated considering an added layer of 20nm of Al2O3 and POx on top of each nanowire and its cone with a material efficiency of 80%.
The back contact is a 300nm thick layer of Al, which is placed with a material efficiency of 80%.

In figure 5.6 the different material cost components are shown. The main cost component is the Cs-Si wafer followed by the back contact. The cost for the InP growth is relatively low due to the minimal material usage in nanowires. The recycling cost of materials that are left behind in the machines is assumed to be the same as the intrinsic value of these materials, thus not generating any extra cost or revenue.

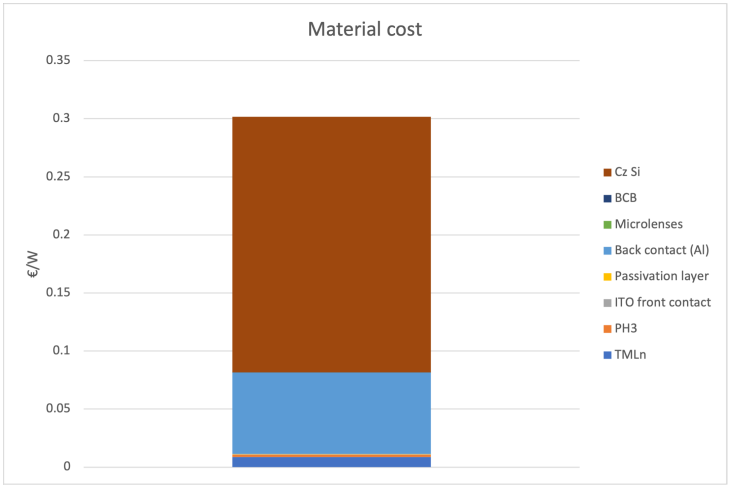

Figure 5.6: OPEX for the different materials used in the production.

Building

The OPEX of the building includes electricity consumption, rent and utilities, and daily lab equipment.

Electricity
There are three different electricity-consuming parts, the machines, the cleanroom, and the utility of the office space. The average electricity consumption of each machine was estimated based on interviews with Oxford Instruments and the EVG Group and on NREL literature. The total uptime of each machine was determined and the total energy consumption is calculated. It has to be mentioned here the values here give an indication and not an exact value due to the uncertainty of the values obtained. During the interviews with Oxford Instruments and EVG Group it was mentioned that the interviewer could only roughly guess the electricity consumption of the machines. The cleanroom energy consumption is based on the average energy consumption of a type 2 cleanroom [78] [79]. Lastly, the electricity consumption of the office space is considered, which is significantly less than the cleanroom and machine energy usage. The electricity price is based on the large consuming companies according to the Centraal Bureau voor de Statistiek (CBS, statistical data for the Netherlands) and is €0.202 for large consumers in April 2023.

Rent and utilities
The rent is based on an average rent rate in Eindhoven for office space in April 2023. For the small production a total area of $200m^2$ is rented for €42 000 per year and for the large production an area of $270m^2$ is rented for €51 000 per year. The average utility rate is assumed to be €35 per m^2 of office space. Note that the cleanroom area is larger than the rented space because the cleanroom can be on multiple floors.

Daily lab equipment
Daily lab equipment includes gloves, laundry for clothes, specialized cleaning, etc. This cost is estimated to be around €3.5 per person per day, according to Patrick Bax.

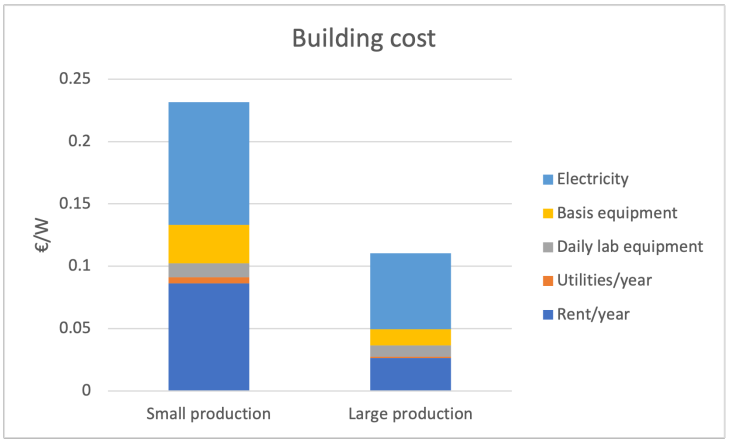

Figure 5.7: Total OPEX cost which includes all components related to the building and cleanroom.

In figure 5.8 the total OPEX can be seen. As expected the OPEX cost for the materials and consumables does not change for the two different production volumes. Labor cost is a large component of OPEX, which indicates that automatization of production can reduce OPEX. This can be accomplished by using more wafers tracks or (sorting) robots.

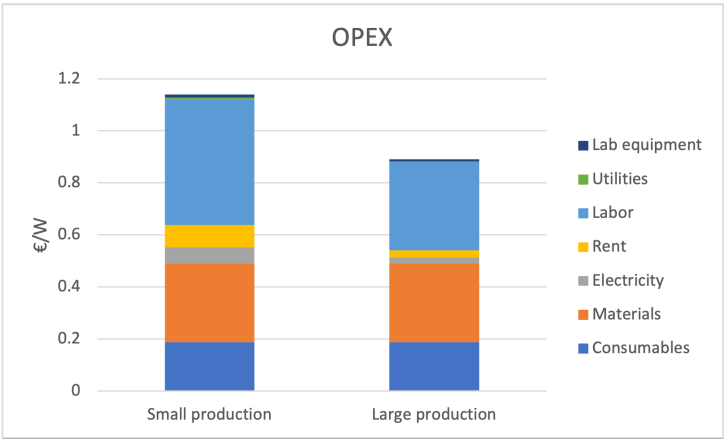

Figure 5.8: Total OPEX cost for the production of nanowire solar cells.

5.4 Total Production Cost

The total production cost or the gate price of nanowire solar cells is determined by combining the operational expenses (OPEX) and capital expenses (CAPEX) in units of €/W. To account for unforeseen risks, changes, or uncertainties, an additional 10% contingency amount is included in the cost analysis. The total cost per Watt, as shown in Figure 5.9, is predominantly influenced by the depreciation cost of the acquired machines. Specifically, the cost per watt is €2.83 for small-scale production and €1.54 for large-scale production.

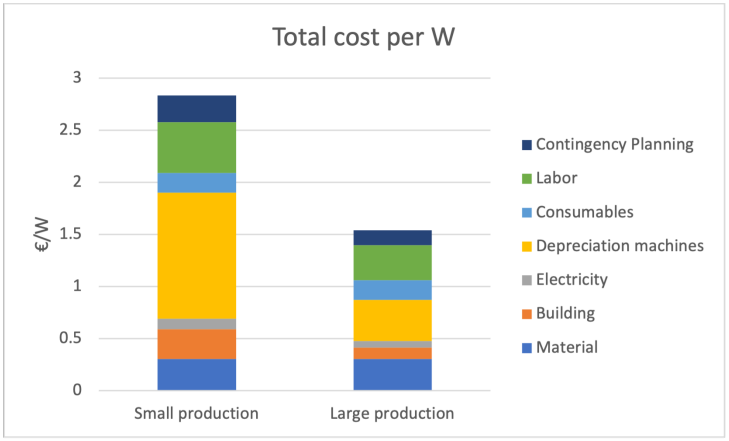

Figure 5.9: Total cost per Watt for a 4-inch nanowire solar cell.

5.4.1 Sensitivity Analysis

A sensitivity analysis is conducted on two variables. Firstly, the impact of a 20% increase in the different cost components is examined. Subsequently, different efficiencies are assumed to determine the resulting effect on the cost per watt.
The smaller production volume is more sensitive to a price change as compared to the larger production volume due to the relatively large CAPEX cost. The total CAPEX differs €2 984 000 between the two production volumes, which is around 32.5% of the CAPEX for the small production. This 32.5% difference in CAPEX gives 4 times more production. The OPEX cost, already expressed in €/W decreases 23% for the large production compared to the small production.
As expected the depreciation cost will have the largest effect on the price.

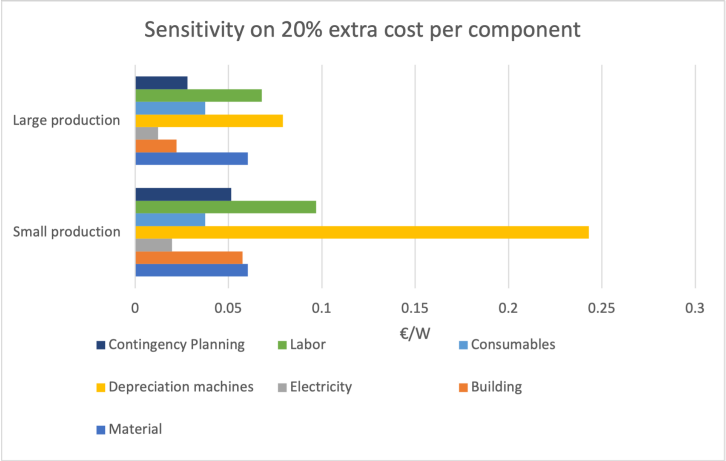

Figure 5.10: Sensitivity analysis on different cost components.

The efficiency has also a large impact on the price of solar cells. The cost per Watt is calculated for three different efficiencies as shown in figure 5.11. The most optimistic case where we have large production with ultimate efficiency of 46%, the cost per Watt drops down to almost €1.10/W, where as in the most conservative case with small production and an efficiency of 20% it is almost €4.67/W

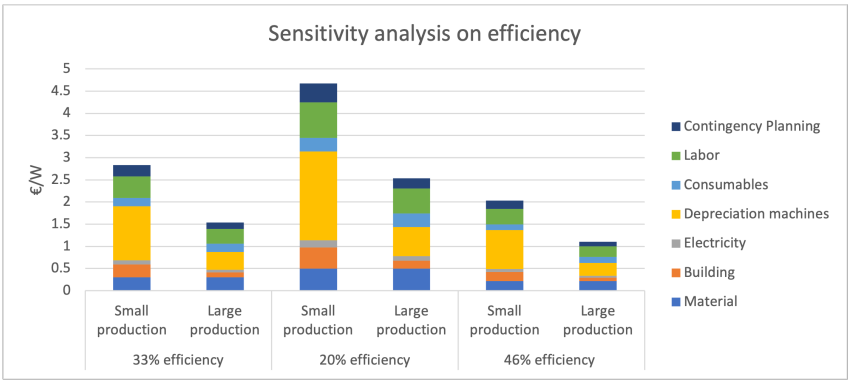

Figure 5.11: Sensitivity analysis on different efficiencies.

5.4.2 Levelized Cost of Energy

To estimate the levelized cost of energy (LCOE), it is necessary to consider the balance of the system (BOS). The BOS for solar cells is assumed to be similar to conventional ones. According to NREL research [72], the total cost of a conventional solar cell is approximately €1.85/W, while the gate price of the solar cell itself is €0.35/W. For this estimation, the gate price is replaced by the gate price estimated by the total cost. To maximize the yield, a 2D axis tracker is added, which has place for 11 panels of an area of 2.26 m^2, each containing 306 4-inch solar cells. The average Direct Normal Irradiance (DNI) in Eindhoven, is 913 $kWh/m/day$ [80]. The system's lifetime is assumed to be 20 years.
The calculated LCOE values can be seen in table 5.1. These results demonstrate that efficiency has a significant impact on the LCOE, while the price of the cells is less influential, as evident from the difference between small and large production scenarios.

Efficiency	Small production	Large production
20%	€0.2679/W	€0.2593/W
33%	€0.1624/W	€0.1572/W
46%	€0.1165/W	€0.1127/W

Table 5.1: LCOE for different efficiencies.

5.4.3 Production in External Cleanroom

The production can also be outsourced to an external cleanroom, where the materials and machines necessary for production are rented. Nano lab of the TU/e (Eindhoven University of Technology) is chosen for this cost analysis. They offer a flat rate of €185/h for cleanroom usage per person, which includes the cost of materials and consumables. According to Frank Dirne, the only additional costs to consider are the starting wafer cost and labor cost.
After understanding the production process, Frank Dirne suggested that investing in a wafer track would help reduce the total time spent in the cleanroom additionally an investment in a nanoimprint machine is necessary for this specific production process. A more affordable nanoimprint machine with a lower production rate can be purchased for approximately €630 000, which includes the creation of two masters for imprinting the nanowire seeds and micro lenses, according to Frank Dirne.
When the company purchases these systems, they can rent cleanroom space for the machine at a rate of €2000/m^2/$year$. If the company uses its own purchased machines in the cleanroom, no additional fees (€185/h) need to be paid while using their own machines. The cleanroom is accessible 24/7 for the company, and maintenance is included in the price.
In this scenario, the assumption is made that a nanoimprint machine is purchased, and a rental space of 20m^2 is obtained. Due to limited space in the current cleanroom, no wafer track is acquired. The processing time for each machine, along with its capacity, is taken into account. The time spent in the cleanroom is assumed to be equal to the total processing machine time. To factor in uncertainty and wet bench work, an additional 25% is added. Based on these considerations, the total estimated time required for producing 1500 wafers is calculated to be 1410 hours. The estimation of the total cost per Watt incorporates several factors, including depreciation cost, labor cost, rent, hourly fee, and starting

wafer cost. Based on these considerations, the total cost per Watt is estimated to be €144.42/W for a 33% efficiency nanowire solar cell.

Chapter 6

Conclusion and Outlook

6.1 Conclusion

Nanowire solar cells hold promising potential for enhancing the efficiency and cost-effectiveness of future solar cell technology. By utilizing nanowires, these cells minimize the usage of costly materials and significantly improve the open circuit voltage, resulting in higher overall efficiency. While they may currently be more suitable for niche applications prioritizing efficiency over short-term costs, advancements in fabrication techniques and larger-scale production facilities are expected to eventually offer a more attractive price-to-performance ratio for broader adoption in the long term.

The theory on solar cells is mostly explained from the point of view of the detailed balance. While a more in-depth understanding of the energy flows and energy quality is mostly ignored. In order to determine fundamental losses in the solar cell it is important to understand the thermodynamics of a solar cell which teaches us its energy flows and energy quality. This thermodynamic view shows us that a solar cell (at open circuit) can be seen as a black box and can be described by the energy flow coming in and coming out in the form of light. The efficiency of the system can then be described by its reversibility, thus the solar cell also emits light and acts as a LED. The thermodynamic description is done in this thesis in two ways, the thermodynamics of a light beam and the thermodynamics of a black body.

Zooming in on the thermodynamics of the light beam reveals four main losses: Carnot loss, photon cooling, étendue loss, and photoluminescence efficiency. This analysis employs a heat engine model, treating photons as pure heat, to represent a working solar cell. To calculate the system's irreversibility, the entropy of the incoming and emitted beams is considered. The entropy depends on the beam's étendue, number of photons, temperature (and frequency), and is derived from the number of permutations in 4D phase space. The topic of photon entropy is actively debated in the research community, with ongoing discussions about the most appropriate method for its description.
Blackbody thermodynamics specifically the exergy analysis teaches us that temperature is important for the energy quality of light and that higher energy photons are also of higher quality energy compared to lower energy photons. It reveals that light energy cannot be solely considered as pure heat, but rather as a distinct form of energy (electromagnetic energy). To describe photons as heat, an infinite heat engine is introduced, incorporating the concept of equivalent temperature for monochromatic photons. This approach helps us better understand the unique characteristics of monochromatic light energy in thermodynamic terms.

To overcome some of the fundamental losses nanowire solar cells can be used. Due to its properties, the nanowires emit light under lower étendue than conventional solar cells making the system more reversible. By introducing micro lenses the system focuses the light onto a single nanowire. This increases the photoluminescence efficiency (until the radiative limit) and reduces the étendue loss. However, the presence of unilluminated nanowires keeps the dark saturation current unchanged, hindering an increase in cell efficiency. To profit from this the nonilluminated wires need to be disconnected or removed. This gives us the setup this thesis has focused on in the cleanroom. However, not a single nanowire is placed underneath the micro lens but a 3x3 array, to make it easier to align it during fabrication.
The fabrication of a 3x3 nanowire solar cell array was performed in the cleanroom where a lot of time of the thesis was spent on. However, due to setbacks in the cleanroom and broken cells, the fabrication of

a finished 3x3 cell with microlenses on top was not yet finished in time. The fabrication continues after the submission of the report.

To investigate the relation between excitation power, photoluminescence efficiency, and other solar cell parameters, a series of experiments were performed. The experiments show that the photoluminescence efficiency increases with a power law against higher excitation power. The exponent in the power law is normally between 1 and 2 where 1 corresponds with the radiative limit and 2 when non-radiative recombination is dominant. The measured photoluminescence did not follow the expected power law relation (at low excitation) and did not agree with the calculated theoretical photoluminescence efficiency, raising the possibility of unexplored phenomena not yet described in solar cell thermodynamics. The apparent/calculated radiative recombination increased faster as if non-radiative recombination is dominant while the observed radiative recombination acts as if in the radiative limit, there is a clear mismatch here between theory and experimental findings. Furthermore, the measured solar cells show a relatively large ideality factor which increases with excitation power.

Lastly, a detailed bottom-up cost analysis was performed on a potential fabrication large-scale manufacturing facility. This cost analysis divides the CAPEX and OPEX costs of the cell and estimates the LCOE. The data used in this cost analysis are from previous cost analyses and interviews. However, due to time constraints, only a few interviews were performed to obtain all the data in detail, resulting in values that are estimated by the interviewer resulting in errors. In order to get a more accurate picture more interviews need to be done. Learning from the interviews is also key to designing the most (cost) efficient production facility with the right machinery. For the large-scale production of 4-inch cells with an efficiency of 33%, the cost was estimated to be €1.54/W with an LCOE €0.1572/W.

6.2 Outlook

There are several areas in this thesis that require some revisit and extra research. The most important areas for further investigation are summarized here.

In the context of solar cell thermodynamics, there are various approaches to study the energy flows and energy quality of the system. To gain deeper insights into loss mechanisms, particularly photon cooling, further exploration of the equivalent temperature theory and its alignment with Martvart's explanation is essential. Understanding the thermal energy transfer between hot photon gas and cold valence band electrons to get a "hot" excited electron, followed by cooling to the conduction band and subsequently to the valance band, is crucial. The theory presented by Z. Zhou, highlighting the equivalent temperature of monochromatic photons and their availability, needs thorough investigation to comprehend the transformation of thermal photon energy from incident to emitted light beams, pinpointing potential losses in the solar cell. Additionally, extensive research is required to analyze I-V curves and other solar cell parameters, specifically their dependence on different excitation powers, with a special focus on photoluminescence efficiency. While the experiments in this thesis showed differences between theoretical and measured values, gathering more data from more nanowire solar cell samples is essential to understanding the underlying phenomena at play.

Throughout the year, various samples were created in the cleanroom, but only one cell was measured, highlighting the challenge of consistent fabrication. Reproducibility is crucial for reliable research outcomes. While the fabrication steps remain constant, the resulting solar cells exhibit variations, mainly influenced by machine maintenance and different users. Designing a reproducible recipe for the solar cells is challenging due to these factors. Therefore, it is essential to regularly update and check the existing optimizations, such as nanowire etching in Sentech and marker doses. Additionally, it was observed that the application of a BCB layer resulted in a non-planar surface. To address this issue, a potential solution is to introduce an extra step. Initially, an extra thick BCB layer can be applied and cured. Subsequently, the BCB layer can be etched back using a polishing machine. Finally, the remaining few hundred nanometers can be etched back using P-RIE. This additional polishing step creates a smooth and planar starting layer for the subsequent plasma etching process. The final remark on the fabrication can be done on the alignment with markers. Markers are crucial for overlay exposure, and the optimal dose should be selected. For the last two overlay exposures, alignment becomes more challenging due to sample size and manual handeling of the sample. A potential solution could be a specialized holder with precise sample rotation, offering greater reproducibility in solar cell fabrication, possibly achieved

through collaboration with Eric Jan using alignment techniques similar to holders 3 and 4.

Finally for the cost analysis gathering more data is essential. This can be achieved through additional interviews with experts in the field. Moreover, exploring various fabrication methods and machines will help identify the most optimal and cost-effective setup. Interviews with specialized individuals can serve as a valuable starting point. Additionally, to enhance the accuracy of cost analysis predictions, it is advisable to incorporate an uncertainty factor to account for future cost variations and evolving techniques.

Bibliography

[1] Sustainable Development Goals united nations. https://sdgs.un.org/goals. Accessed: 2023-08-10.

[2] Sustainable Development Goals united nations, global roadmap for accelerated sdg 7 action. https://sdgs.un.org/topics/energy. Accessed: 2023-08-11.

[3] Solar PV international energy agency - latest findings. https://www.iea.org/energy-system/renewables/solar-pv. Accessed: 2023-08-11.

[4] Kim Spanjers. Weerstand leidt tot halvering zonnepark bij blokzijl. *Stichting Achmea Rechtsbijstand*, 2019.

[5] Rob Haverkamp. 2020: het jaar van de zonneparken en windenergie. 2020.

[6] Kim Spanjers. Rechtbank: Zonnepark beeksedijk kreeg onterecht een vergunning. 2021.

[7] Sayak Bhattacharya and Sajeev John. Beyond 30% Conversion Efficiency in Silicon Solar Cells: A Numerical Demonstration. *Scientific Reports*, 9(1):12482, 2019.

[8] Jos E M Haverkort, Erik C Garnett, and Erik P A M Bakkers. Fundamentals of the nanowire solar cell: Optimization of the open circuit voltage. *Applied Physics Reviews*, 5(3):31106, sep 2018.

[9] William Shockley and Hans J. Queisser. Detailed Balance Limit of Efficiency of p-n Junction Solar Cells. *Journal of Applied Physics*, 32(3):510–519, March 1961.

[10] Erik C Garnett, Mark L Brongersma, Yi Cui, and Michael D McGehee. Nanowire Solar Cells. *Annual Review of Materials Research*, 41(1):269–295, 2011.

[11] Cui. Y. high-effciency nanowire solar cells. 2015.

[12] P.A.L.M. Koolen. Reducing entropy losses in nanowire solar cells, August 19, 2021.

[13] Solarcell working viridian solar. 4.1 the photovoltaic effect. 2020. =https://www.viridiansolar.co.uk/resources-4-1-photovoltaic-effect.html,.

[14] W. Shockley. The theory of p-n junctions in semiconductors and p-n junction transistors. *The Bell System Technical Journal*, 28(3):435–489, 1949.

[15] Martin Green. Crystalline silicon solar cells. 09 2015.

[16] Andres Cuevas. The recombination parameter j0. *Energy Procedia*, 55, 12 2014.

[17] Vítězslav Benda. 8 - Photovoltaics: The Basics. In Trevor M Letcher and Vasilis M Fthenakis, editors, *A Comprehensive Guide to Solar Energy Systems*, pages 151–179. Academic Press, 2018.

[18] Keith McIntosh. *Lumps, Humps and Bumps: Three Detrimental Effects in the Current–Voltage Curve of Silicon Solar Cells*. PhD thesis, 01 2001.

[19] Myriam Paire, Laurent Lombez, F. Donsanti, Marie Jubault, Nicolas Péré-Laperne, Stéphane Collin, Arnaud Perona, Alain Dollet, Jean-Luc Pelouard, Daniel Lincot, and Jean-François Guillemoles. Cu(in,ga)se 2 photovoltaic microcells for high efficiency and low material usage. 02 2012.

[20] Vandana Khanna, Bijoy Das, P. Singh, Vandana Panwar, and Dinesh Bisht. A three diode model for industrial solar cells and estimation of solar cell parameters using pso algorithm. *Renewable Energy*, 78:105–113, 06 2015.

[21] Kashif Ishaque, Zainal Salam, and Hamed Taheri. Simple, fast and accurate two-diode model for photovoltaic modules. *Solar Energy Materials and Solar Cells*, 95:586–594, 02 2011.

[22] Jeffrey A. Mazer. Solar cells: An introduction to crystalline photovoltaic technology. 1996.

[23] Keith McIntosh. *Lumps, Humps and Bumps: Three Detrimental Effects in the Current–Voltage Curve of Silicon Solar Cells*. PhD thesis, 01 2001.

[24] Vítězslav Benda. 8 - Photovoltaics: The Basics. In Trevor M Letcher and Vasilis M Fthenakis, editors, *A Comprehensive Guide to Solar Energy Systems*, pages 151–179. Academic Press, 2018.

[25] Vítězslav Benda. 8 - Photovoltaics: The Basics. In Trevor M Letcher and Vasilis M Fthenakis, editors, *A Comprehensive Guide to Solar Energy Systems*, pages 151–179. Academic Press, 2018.

[26] Silke Steingrube, Otwin Breitenstein, Klaus Ramspeck, Stefan Glunz, Andreas Schenk, and Pietro Altermatt. Explanation of commonly observed shunt currents in c-si solar cells by means of recombination statistics beyond the shockley-read-hall approximation. *Journal of Applied Physics*, 110:014515–014515, 07 2011.

[27] Vítězslav Benda. 8 - Photovoltaics: The Basics. In Trevor M Letcher and Vasilis M Fthenakis, editors, *A Comprehensive Guide to Solar Energy Systems*, pages 151–179. Academic Press, 2018.

[28] Vidya Ganapati, Myles A. Steiner, and Eli Yablonovitch. The voltage boost enabled by luminescence extraction in solar cells. *IEEE Journal of Photovoltaics*, 6(4), 7 2016.

[29] F.F.C. Dubach. Improvement of the open-circuit voltage in tapered nanowire solar, November 2022.

[30] Robert T. Ross. Some Thermodynamics of Photochemical Systems. , 46(12):4590–4593, June 1967.

[31] Louise Hirst and N.J. Ekins-Daukes. Fundamental losses in solar cells. *Progress in Photovoltaics: Research and Applications*, 19:286 – 293, 05 2011.

[32] Vítězslav Benda. 8 - Photovoltaics: The Basics. In Trevor M Letcher and Vasilis M Fthenakis, editors, *A Comprehensive Guide to Solar Energy Systems*, pages 151–179. Academic Press, 2018.

[33] Uwe Rau, Ulrich Wilhelm Paetzold, Thomas Kirchartz, and Thomas Kirchartz. Thermodynamics of light management in photovoltaic devices. *Physical Review B*, 90:035211, 2014.

[34] W. Ruppel and P. Wurfel. Upper limit for the conversion of solar energy. *IEEE Transactions on Electron Devices*, 27(4):877–882, 1980.

[35] Tom Markvart. Solar cell as a heat engine: Energy-entropy analysis of photovoltaic conversion. *physica status solidi (a)*, 205:2752 – 2756, 12 2008.

[36] Ze'ev Abrams and Xiang Zhang. The concentration limit for solar cells based on entropy production. 07 2012.

[37] Tom Markvart. From steam engine to solar cells: Can thermodynamics guide the development of future generations of photovoltaics? *Wiley Interdisciplinary Reviews: Energy and Environment*, 5:n/a–n/a, 03 2016.

[38] G. Brooker. *Modern Classical Optics, Chapter 11*. Oxford Master Series in Physics. OUP Oxford, 2003.

[39] T Markvart. The thermodynamics of optical étendue. *Journal of Optics A: Pure and Applied Optics*, 10(1):15008, dec 2007.

[40] Tom Markvart. From steam engine to solar cells: Can thermodynamics guide the development of future generations of photovoltaics? *Wiley Interdisciplinary Reviews: Energy and Environment*, 5:n/a–n/a, 03 2016.

[41] Jakapan Chantana, Yu Kawano, Takahito Nishimura, Abdurashid Mavlonov, Qing Shen, Kenji Yoshino, Satoshi Iikubo, Shuzi Hayase, and Takashi Minemoto. Impact of auger recombination on performance limitation of perovskite solar cell. *Solar Energy*, 217:342–353, March 2021. Funding Information: The authors acknowledge the Japan Science and Technology Agency (JST) Mirai program for financial support. Publisher Copyright: © 2021 International Solar Energy Society.

[42] Valerio Sarritzu, Nicola Sestu, Daniela Marongiu, Xueqing Chang, Sofia Masi, Aurora Rizzo, Silvia Colella, Francesco Quochi, Michele Saba, Andrea Mura, and Giovanni Bongiovanni. Optical determination of shockley-read-hall and interface recombination currents in hybrid perovskites. *Scientific Reports*, 7:44629, 03 2017.

[43] Vítězslav Benda. 8 - Photovoltaics: The Basics. In Trevor M Letcher and Vasilis M Fthenakis, editors, *A Comprehensive Guide to Solar Energy Systems*, pages 151–179. Academic Press, 2018.

[44] Yang-Seok Yoo, Tae-Moo Roh, Jong Ho Na, Sung Son, and Yong-Hoon Cho. Simple analysis method for determining internal quantum efficiency and relative recombination ratios in light emitting diodes. *Applied Physics Letters*, 102, 05 2013.

[45] Ksenia Korzun, Gabriel W Castellanos, Dick K G de Boer, Jaime Gómez Rivas, and Jos E M Haverkort. Nanowire Solar Cell Above the Radiative Limit. *Advanced Optical Materials*, 9(2):2001636, 2021.

[46] Tom Markvart. Solar cell as a heat engine: energy–entropy analysis of photovoltaic conversion. *physica status solidi (a)*, 205(12):2752–2756, 2008.

[47] Tom Markvart. Thermodynamics of losses in photovoltaic conversion. *Applied Physics Letters*, 91(6):64102, aug 2007.

[48] T Markvart. The thermodynamics of optical étendue. *Journal of Optics A: Pure and Applied Optics*, 10(1):15008, dec 2007.

[49] S R de Groot and P Mazur. *Non-equilibrium thermodynamics*. Dover Publications, New York SE -, dover ed edition, 1984.

[50] Tom Markvart. Counting sunrays: from optics to the thermodynamics of light. In Viorel Badescu and Marius Paulescu, editors, *Physics of the Nanostructured Solar Cells*. Nova Science Publishers, December 2009.

[51] Lev Davidovic Landau and Evgenij M. Lifsic. *Statistical physics*. Pergamon Press, 1958.

[52] Ibrahim Dincer and Marc A Rosen. Chapter 2 - Exergy and energy analyses. In Ibrahim Dincer and Marc A Rosen, editors, *Exergy (Third Edition)*, pages 23–35. Elsevier, third edit edition, 2021.

[53] Zhijun Zhou, Shiquan Shan, Liping Chen, and Yanwei Zhang. Exergy of Blackbody Radiation and Monochromatic Photon. *International Journal of Thermophysics*, 38(4):57, April 2017.

[54] Ryszard Petela. *Engineering Thermodynamics of Thermal Radiation: for Solar Power Utilization*. McGraw-Hill Education, New York, 1st edition edition, 2010.

[55] Sean Wright. Comparative Analysis of the Entropy of Radiative Heat Transfer and Heat Conduction, 2007.

[56] L N M Duysens. Photosynthesis. *Progress in Biophysics and Molecular Biology*, 14:1–104, 1964.

[57] David C Fork. *Photosynthesis*, pages 347–390. Springer US, Boston, MA, 1989.

[58] S. Lems, H.J. Kooi, and J. Arons. Exergy analyses of the biochemical processes of photosynthesis. *International Journal of Exergy - INT J EXERGY*, 7, 03 2010.

[59] Davor Juretić and Pasko Zupanovic. Photosynthetic models with maximum entropy production in irreversible charge transfer steps. *Computational Biology and Chemistry*, 27:541–553, 12 2003.

[60] J Lavergne and P Joliot. Energy transduction in membranes. *by Biophysical Society*, 2000.

[61] Géza Meszéna, Hans V Westerhoff, and Oscar Somsen. Reply to comment onnon-equilibrium thermodynamics of light absorption'. *Journal of Physics A: Mathematical and General*, 33(6):1301, 2000.

[62] Chen Zeshao and Mo Songping. Effective temperature and exergy of monochromic blackbody radiation []. *Progress in Natural Science*, 17(10):1250–1254, 2007.

[63] P Baruch and J Parrott. Thermodynamic cycle for photovoltaic energy conversion. *Journal of Physics D: Applied Physics*, 23:739, 11 2000.

[64] Mei Gong and Göran Wall. Exergy analysis of the supply of energy and material resources in the swedish society. *Energies*, 9:707, 09 2016.

[65] Raphael Clady, Murad J Y Tayebjee, Pasquale Aliberti, Dirk König, Nicholas John Ekins-Daukes, Gavin J Conibeer, Timothy W Schmidt, and Martin A Green. Interplay between the hot phonon effect and intervalley scattering on the cooling rate of hot carriers in GaAs and InP. *Progress in Photovoltaics: Research and Applications*, 20(1):82–92, 2012.

[66] E L Meyer. Extraction of Saturation Current and Ideality Factor from Measuring V_{oc} and I_{sc} of Photovoltaic Modules. *International Journal of Photoenergy*, 2017:8479487, 2017.

[67] David Hill, Taylor Teitsworth, Earl Ritchie, Joanna Atkin, and James Cahoon. Interplay of surface recombination and diode geometry for the performance of axial p - i - n nanowire solar cells. *ACS Nano*, 12, 09 2018.

[68] Sven Rühle. Tabulated values of the shockley–queisser limit for single junction solar cells. *Solar Energy*, 130:139–147, 06 2016.

[69] Alan Goodrich and Michael Woodhouse. A manufacturing cost analysis relevant to single- and dual-junction photovoltaic cells fabricated with iii-vs and iii-vs grown on czochralski silicon. 1(2), 9 2013.

[70] Kelsey A. Horowitz, Timothy W. Remo, Brittany Smith, and Aaron J. Ptak. A techno-economic analysis and cost reduction roadmap for iii-v solar cells.

[71] Maxwell Zheng, Kelsey Horowitz, Michael Woodhouse, Corsin Battaglia, Rehan Kapadia, and Ali Javey. Iii-vs at scale: A pv manufacturing cost analysis of the thin film vapor-liquid-solid growth mode. *Progress in Photovoltaics: Research and Applications*, 24:n/a–n/a, 06 2016.

[72] Ran Fu, David J. Feldman, Robert M. Margolis, Michael A. Woodhouse, and Kristen B. Ardani. U.s. solar photovoltaic system cost benchmark: Q1 2017.

[73] Andrea Cattoni, Andrea Scaccabarozzi, Hung-Ling Chen, Fabrice Oehler, Chalermchai Himwas, Gilles Patriarche, Maria Tchernycheva, Jean-Christophe Harmand, and Stéphane Collin. Iii-v nanowires on silicon: a possible route to si-based tandem solar cells. page PM3A.2, 01 2017.

[74] S Bhunia, T Kawamura, S Fujikawa, K Tokushima, and Y Watanabe. Free-standing and vertically aligned InP nanowires grown by metalorganic vapor phase epitaxy. *Physica E: Low-dimensional Systems and Nanostructures*, 21(2):583–587, 2004.

[75] S Paiman, Q Gao, H H Tan, C Jagadish, X Zhang, and J Zou. Effects of growth rate on InP nanowires morphology and crystal structure. *Journal of Crystal Growth*, 383:100–105, 2013.

[76] Mecart-cleanrooms, cost of a cleanroom per square foot – how much does a modular cleanroom cost. `https://www.mecart-cleanrooms.com/learning-center/cost-cleanroom-per-square-foot/`.

[77] Ondernemen met personeel. loonkosten werkgever berekenen met behulp van een reken-module. `https://www.ondernemenmetpersoneel.nl/orienteren/personeelskosten/dit-zijn-de-kosten-van-personeel#:~:text=De%20kosten%20van%20personeel%20kun,die%20je%20met%20werknemers%20maakt.`

[78] Jiawen Yin, Xiaohua Liu, Bowen Guan, Zhiyao Ma, and Tao Zhang. Performance analysis and energy saving potential of air conditioning system in semiconductor cleanrooms. *Journal of Building Engineering*, 37:102158, 2021.

[79] T.B.J. Ludlage, Marcel G.L.C. Loomans, Harm van den Oever, Paul C.A. Molenaar, Helianthe S.M. Kort, and Paul H.J. Joosten. Aanzienlijk energiebesparingspotentieel in cleanrooms binnen handbereik: Een green deal voor cleanrooms. *TVVL Magazine*, June 2021(3):26–33, June 2021.

[80] Direct Normal Irradiance in the Netherlands, global solar atlas dni data. https://globalsolaratlas.info/.

Appendices

Appendix A

Fabrication

Figure A.1: InP layer stack

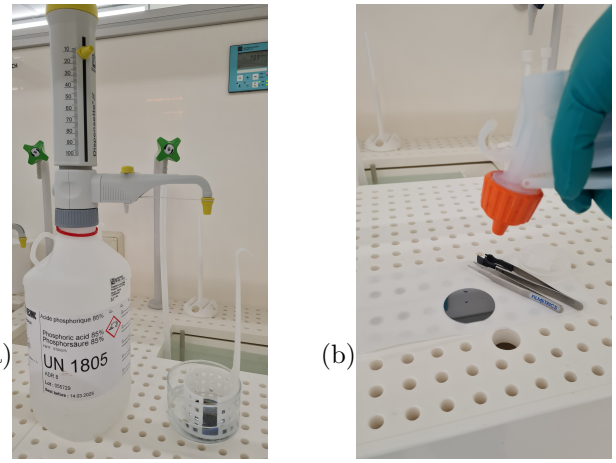

(a) (b)

Figure A.2: Cleanroom steps for 1.a) (a) H3PO4 bath for removing native oxides on the surface, and (b) blow-drying the wafer with Nitrogen gas.

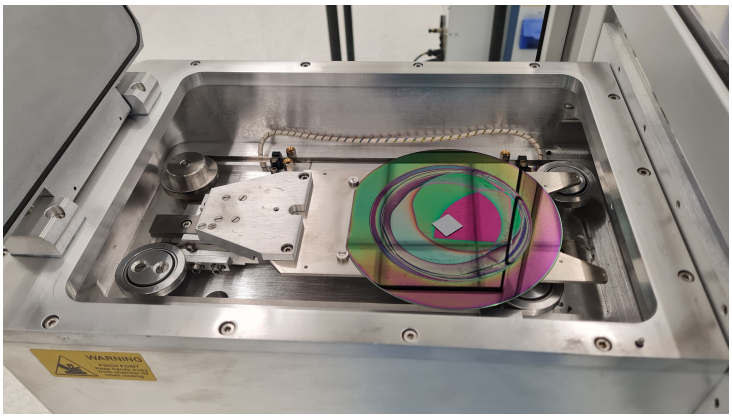

Figure A.3: Using a small piece of Silicon for the preconditioning of the SiNx deposition in the PECVD while simultaneously checking the deposition rate. step 1b)

Figure A.4: Sample is located in the spinner to spin coat the resist, step 1c)

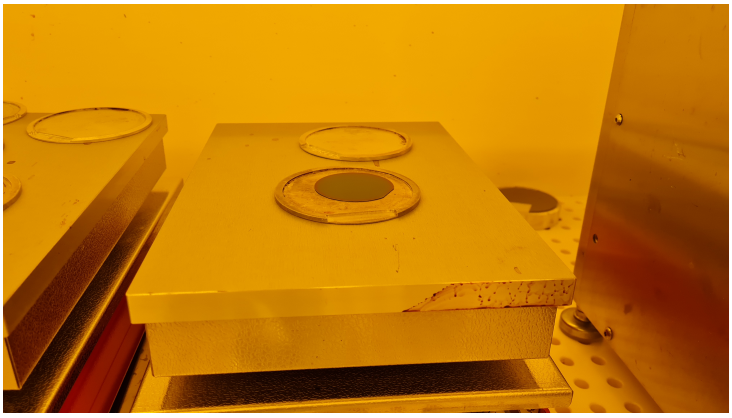

Figure A.5: Sample is baked after the spin coating of the resist. step 1c)

Appendix B

Extension on photoluminacence efficiency

Similarly for the photoluminescence intensity as in section 2.4, we can write the absorbed SRH recombination intensity I_{SRH} in terms of non-radiative recombination rate as:

$$I_{SRH} = h\nu(1 - \overline{P_{esc}})An \equiv a \cdot An$$

In which a is a new constant. Writing it in terms of the carrier concentration as:

$$n = \frac{I_{SRH}}{aA}$$

Similarly as for PL intensity, we can write in the non-radiative limit the SRH intensity in terms of solar intensity as:

$$G = xI_{sun} = \frac{AI_{SRH}}{a \cdot A} \rightarrow I_{SRH} = C_{SRH}^{nrad} I_{sun}^{1}$$

With $C_{SRH}^{nrad} = x \cdot a$. Which shows a linear relationship between the solar intensity and the SRH intensity in the nonradiative limit. And in the radiative limit:

$$G = xI_{sun} = B(\frac{I_{SRH}}{a \cdot A})^2 \rightarrow I_{SRH} = C_{SRH}^{rad} I_{sun}^{0.5}$$

With $C_{SRH}^{rad} = a \cdot A\sqrt{\frac{x}{B}}$. Indicating a square-root relation between the SRH intensity and the incoming solar radiation in the radiative limit. However, it should be noted that this is a theoretical result. in reality no SRH recombination is present in the radiative limit as we shall see.
In the arbitrary case where we the SRH intensity can we written as

$$I_{SRH} = h\nu(1 - \overline{P_{esc}})AI_{sun}^{\mu}$$

Which gives an SRH external nonradiative efficiency of

$$\eta_{ext}^{SRH} = \frac{I_{SRH}}{I_{sun}} \propto I_{sun}^{\mu-1} \propto X_{conc}^{\mu-1}$$

With $0.5 \leq \mu \leq 1$ and $\eta_{ext}^{SRH} + \eta_{ext}^{PL} = 1$. When the radiative efficiency and nonradiative efficiency is written in the radiative limit with $\beta = 1$ and $\mu = 0.5$ it can be seen that the relation is only true when the incoming light intensity approaches infinity.

$$\lim_{I_{sun} \to \infty} C_{PL}^{rad} I_{sun}^{0} + C_{SRH}^{rad} I_{sun}^{-0.5} = 1$$

Where $C_{PL}^{rad} = x \cdot b = \frac{(1-R)a_b}{h\nu} h\nu\overline{P_{esc}} = 1$ when we have perfect absorption ($a_b = 1$), no reflection ($R = 0$) and a angled average photon escape probability $\overline{P_{esc}} = 1$. As seen from here the SRH intensity will approach zero in the radiative limit.
Similar in the nonradiative limit with $\beta = 2$ and $\mu = 1$:

$$\lim_{I_{sun} \to 0} C_{PL}^{nrad} I_{sun}^{1} + C_{SRH}^{nrad} I_{sun}^{0} = 1$$

This is only true when I_{sun} approaches 0, and $C_{PL}^{nrad} = x \cdot a = \frac{(1-R)a_b}{h\nu} h\nu(1 - \overline{P_{esc}}) = 0$ (which happens with $a_b = 1$, $R = 0$,$\overline{P_{esc}} = 1$). Showing that at low excitation, nonradiative recombination is dominant, and at high excitation radiative recombination is dominant.
An energy and particle balance can also be used to establish a connection between the power law of integrated photoluminescence (PL) observed at various excitation powers and the external radiative efficiency and Shockley's and Queisser's equations governing the open-circuit voltage V_{oc}. The balance shows that at open circuit conditions, the external radiative emission efficiency can be determined with the measured PL. The power law can then be used to predict the V_{oc} at different illumination powers.

We can use the first law of thermodynamics, which states that there is a conservation of energy in the system**??**, and there is also a conservation of particles in this system. This analysis considers two types of particles, namely photons and electron-hole pairs, which can be interconverted at a 1 : 1 ratio (this assumption is made for the present analysis). Therefore, we can say:

$$E_{in} = E_{out}$$

$$N_{in} = N_{out}$$

Where E_{in} and E_{out} stand for the energy in- and out flow, respectively. N_{in} represents the total inflow of particles (photons) and N_{out} the total outflow of particles (electron-hole pairs and photons).

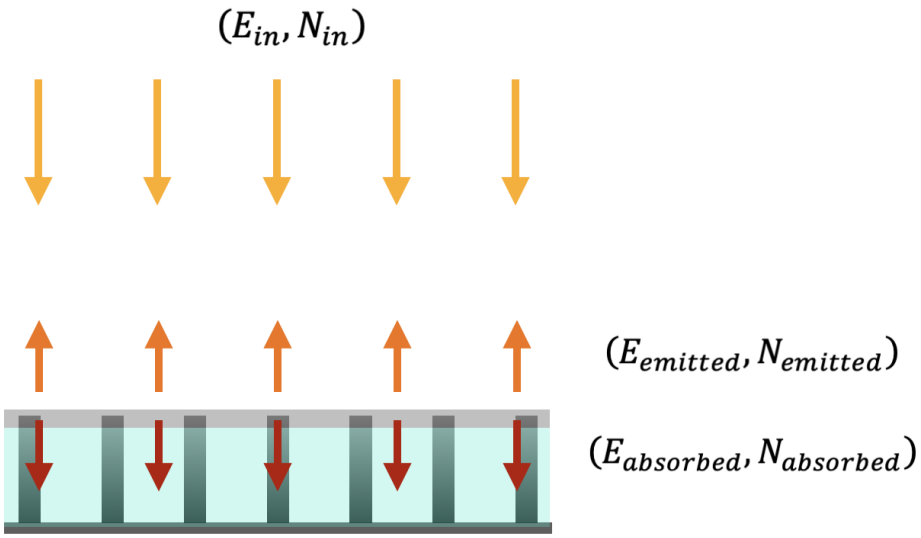

Figure B.1: Schematic representation of an energy and particle balance of a direct bandgap solar cell under open circuit conditions.

To simplify the problem it is assumed the incoming photons all have the same wavelength of $532nm$ or $E_\lambda = \frac{hc}{\lambda} = 2.33eV$. These photons have enough energy to excite electrons to the conduction band, creating electron-hole pairs. There will be no reflection and perfect absorption.
The energy and particle balance for the system becomes B.1:

$$E_{in} = E_{emitted} + E_{absorbed} \tag{B.1}$$

$$N_{in} = N_{emitted} + N_{absorbed} \tag{B.2}$$

In the particle balance, there is a number of incoming photons N_{in} (per second). All photons create an electron-hole pair because there are only photons that interact with the solar cell (or are proportional to the number of photons, reflection, absorption, etc.). After the current creation, the electron-hole pairs either radiatively recombine ($N_{emitted}$), or are lost ($N_{absorbed}$) due to non-radiative recombination and leakage current. This can be measured by a PL experiment, where the number of emitted photons is measured against excitation power ($\sim N_{in}$). The number of particles (per second) can be related to the current as $I_i = qN_i$.
In the energy balance, there is an influx of energy E_{in} (at STC $\approx 1000W/m^2$). The outflux of energy is also measured in a PL measurement ($E_{emitted} = N_{emitted} * E_{\lambda,emitted}$, with $E_{\lambda,emitted}$ the photon energy

of the emitted photons). With these two values, it is possible to calculate the energy that is absorbed by the cell $E_{absorbed}$, which correlates to the total amount of heat that is absorbed by the solar cell.
The power law is written as $y = ax^{\beta(x)}$, where y is the integrated PL (measured in counts $N_{emitted}$), x the excitation power ($x = E_{suns} = N_{in} * E_{\lambda}$), a the experimental constant and, the exponential factor $\beta(x)$ which shows the dependence of the radiative recombination rate on the excitation power.
The external radiative efficiency can be written in terms of the power law, when the power law is transformed to the number of incoming and emitted photons, with $N_{emitted} = a(N_{in} * E_{\lambda})^{\beta(x)}$. The external radiative efficiency becomes:

$$\eta_{ext}^{PL} = \frac{N_{emitted}}{N_{in}} = \frac{ax^{\beta(x)}}{N_{in}} = \frac{ax^{\beta(x)}}{x} E_{\lambda} = \alpha x^{\beta(x)-1} \tag{B.3}$$

Where α includes the experimental and transformation constant. This analysis shows that η_{ext}^{PL} depends on the excitation power and the function $\beta(x)$.
To calculate the V_{oc} at different excitation powers equation 2.7 can be used by substituting η_{ext}^{PL} with equation B.3.

Appendix C

Defining Energy, Entropy and Photon Number

The conventional way of describing the energy, entropy, and number of photons at constant volume (V) (see, for example, Landau and Lishitz, 1953) is given by multiplying the individual photon variable (s or $h\nu$) by the density of states ($D_\nu = \frac{8\pi n^3\nu^2}{c^3}$) and the equilibrium photon occupation number ($\rho_\nu = \frac{1}{e^{(h\nu-\mu)/(k_bT)}-1}$) and integrating over the full absorption spectrum:

$$S = V\int_{(v)} sD_\nu\rho_\nu = k_bV\int_{(v)} \frac{8\pi n^3\nu^2}{c^3}\left[(1+\rho_k)\ln(1-\rho_k) - \rho_k\ln\rho_k\right]d\nu$$

$$U = V\int_{(v)} h\nu D_\nu\rho_\nu = V\int_{(v)} \frac{8\pi n^3\nu^2}{c^3}h\nu\rho_\nu d\nu$$

$$N = V\int_{(v)} D_\nu\rho_\nu = V\int_{(v)} \frac{8\pi n^3\nu^2}{c^3}\rho_\nu d\nu$$

Now the thermodynamic variables can be transformed from expressions for a photon gas inside a box, or non-traveling light beams, to a traveling light beam, or convective flow. The particle flow is given as an example and similar reasoning can be applied for the entropy and energy flow.
At time t we have a photon gas with volume V and a number of photons N, all the photons are emitted in an isotropic way. The number of photons emitted from an area δA within a solid angle $\delta\Omega$ in a time interval δt. In this time, a cone with a base surface area δA and a height $\frac{c}{n}t$ is filled. The entire cone is at an angle θ with respect to the absorbing medium. We can then write the photon flux in terms of étendue as:

$$\dot{N} = \delta A\delta\Omega cos(\theta)\frac{cN}{4\pi nV} = \frac{c}{4\pi Vn^3}\delta\varepsilon N$$

We have now an equation that related the enclosed photon gas with a flux, where the prefactor $\frac{c\varepsilon}{4\pi Vn^3}$ is used. With similar reasoning for the entropy and energy, we find the same prefactor.
Rewriting the constant state to a flux we can use the prefactor. We see now that in this alternative reasoning, the density of states is transformed to a single quantum state where the volume is written in terms of étendue see 2.14.

$$\dot{S} = k_b\int_{(v)} \frac{2\nu^2}{c^2}\varepsilon\left[(1+\rho_k)\ln(1-\rho_k) - \rho_k\ln\rho_k\right]d\nu$$

$$\dot{U} = \int_{(v)} \frac{2\nu^2}{c^2}\varepsilon h\nu\rho_\nu d\nu$$

$$\dot{N} = \int_{(v)} \frac{2\nu^2}{c^2}\varepsilon\rho_\nu d\nu$$

To calculate the energy and entropy when adding or removing a photon from a beam the derivative is taken over the particle flux at constant temperature and étendue (volume):

$$u = \left(\frac{\partial \dot{U}}{\partial \dot{N}}\right)_{\varepsilon,T}$$

$$s = \left(\frac{\partial \dot{S}}{\partial \dot{N}}\right)_{\varepsilon,T}$$

To account for spectral radiation, all terms are integrated over a frequency range (ν_g, ∞) with ν_g the bandgap frequency, this gives the lower bound of the absorbed photons (photons with lower energy than $h\nu_g$ are not "absorbed"). Normally these calculations are integrated numerically, but for weak to moderate intensity, they can be calculated analytically using Mathematica to give:

$$u(T, \varepsilon, \dot{N}) = h\nu_g + k_b T^2 \frac{\gamma^{'}(T)}{\gamma(T)} \approx h\nu_g + k_b T$$

$$s(T, \varepsilon, \dot{N}) = k_b \ln \frac{\varepsilon\gamma(T)}{\dot{N}} + k_b T \frac{\gamma^{'}(T)}{\gamma(T)} \approx k_b \ln \frac{\varepsilon\gamma(T)}{\dot{N}} + 1$$

Appendix D

Derivation equivalent temperature

It is postulated that the equivalent temperature T_λ of a monochromatic radiation photon is inversely proportional to its wavelength λ and is proportional to radiation temperature T. We give an approximate expression for the equivalent temperature $T_{(\lambda)}$:

$$T_{(\lambda)}^k = \frac{fT^m}{\lambda^n}$$

If the equivalent temperature is represented in terms of frequency ν, then $T_{(\nu)}$ can be written as:

$$T_{(\nu)}^k = \frac{fT^m}{c^n}\nu^n$$

where f is a constant.
From the equations above we know:

$$T_{(\nu)} = \frac{f^{\frac{1}{k}}T^{\frac{m}{k}}}{c^{\frac{n}{k}}}\nu^{\frac{n}{k}}$$

$$\frac{T_0}{T_{(\nu)}} = \frac{T_{(\nu_0)}}{T_{(\nu)}} = \left(\frac{\nu_0}{\nu}\right)^{\frac{n}{k}}$$

Substituting this in:

$$W_u = \int_{\nu_0}^{\nu} h\left(1 - \frac{T_0}{T_{(\nu)}}\right)d\nu = h\nu - \frac{k}{k-n}h\nu^{\frac{k-n}{k}}\nu_0^{\frac{n}{k}} + \frac{n}{k-n}h\nu_0$$

The corresponding coefficient of exergy to energy η_u is $\frac{W_u}{h\nu}$

$$\eta_u = 1 - \frac{k}{k-n}\left(\frac{\nu_0}{\nu}\right)^{\frac{n}{k}} + \frac{n}{k-n}\frac{\nu_0}{\nu}$$

$$= 1 - \frac{k}{k-n}\left(\frac{\lambda}{\lambda_0}\right)^{\frac{n}{k}} + \frac{n}{k-n}\frac{\lambda}{\lambda_0}$$

$$= 1 - \frac{k}{k-n}\frac{T}{T_0} + \frac{n}{k-n}\left(\frac{T}{T_0}\right)^k$$

As mentioned in 2.6.2, Petela's formula correctly represents the exergy of blackbody radiation. Thus, considering the link between the macroscopic field and microscopic field, if the blackbody monochromatic emission intensity is multiplied by the coefficient of exergy to energy η_u as in the equation derived here above and then integrated over the full wavelength, it should be equal to the exergy of blackbody radiation, which is represented by Petela's formula. This is the monochromatic emission intensity of blackbody radiation proposed by Planck [31]:

$$i_{b,i} = \frac{c_1\lambda^{-5}}{e^{c2/\lambda T} - 1}$$

Where $c_1 = 2\pi hc^2 = 3.74 \cdot 10^{-16} W \cdot m^2$, $c_2 = hc/k = 1.4388 \cdot 10^{-2} m \cdot K$. $c1$ is the first radiative constant and c_2 the second radiative constant. Therefore the following relation exists:

$$\int_0^\infty i_{b,i} \left[1 - \frac{k}{k-n} \frac{T}{T_0} + \frac{n}{k-n} \left(\frac{T}{T_0} \right)^k \right] d\lambda = \sigma T^4 \left[1 - \frac{3}{4} \frac{T_0}{T} + \frac{1}{3} \left(\frac{T_0}{T} \right)^4 \right] \tag{D.1}$$

The expression of equivalent temperature can be obtained through this formula. The left-hand side of can be expressed as:

$$\int_0^\infty i_{b,i} \left[1 - \frac{k}{k-n} \frac{T}{T_0} + \frac{n}{k-n} \left(\frac{T}{T_0} \right)^k \right] d\lambda = \int_0^\infty \frac{c_1 \lambda^{-5}}{e^{c2/\lambda T} - 1} \left[1 - \frac{k}{k-n} \frac{T}{T_0} + \frac{n}{k-n} \left(\frac{T}{T_0} \right)^k \right] d\lambda$$

Where we obtain three terms:

$$= \sigma T^4 - \frac{k}{k-n} \frac{c_1 T_0}{f^{\frac{n}{k}} T^{\frac{m}{k}}} \int_0^\infty \frac{c_1 \lambda^{-5+n/k}}{e^{c2/\lambda T} - 1} d\lambda + \frac{n}{k-n} \frac{c_1 T_0^k}{f T^m} \int_0^\infty \frac{c_1 \lambda^{-5+n}}{e^{c2/\lambda T} - 1} d\lambda$$

Setting $x = c_2/\lambda T$ and $dx = -\frac{c_2}{\lambda^2 T} d\lambda$. The second term can be expressed as:

$$\frac{k}{k-n} \frac{c_1 T_0}{f^{\frac{n}{k}} T^{\frac{m}{k}}} \int_0^\infty \frac{c_1 \lambda^{-5+n/k}}{e^{c2/\lambda T} - 1} d\lambda = \frac{k}{k-n} \frac{c_1 T_0 T^{4-\frac{n}{k}-\frac{m}{k}}}{f^{\frac{n}{k}} - c_2^{4-\frac{n}{k}}} \int_0^\infty \frac{x^{3-\frac{n}{k}}}{e^x - 1} dx$$

and the last term:

$$\frac{n}{k-n} \frac{c_1 T_0^k}{f T^m} \int_0^\infty \frac{c_1 \lambda^{-5+n}}{e^{c2/\lambda T} - 1} d\lambda = \frac{n}{k-n} \frac{c_1 T_0^k T^{4-n-m}}{f c_2^{4-n}} \int_0^\infty \frac{x^{3-n}}{e^x - 1} dx$$

Set $a = \int_0^\infty \frac{x^{3-\frac{n}{k}}}{e^x - 1} dx$ and $b = \int_0^\infty \frac{x^{3-n}}{e^x - 1} dx$. We can write D.1 as:

$$\sigma T^4 - \frac{k}{k-n} \frac{c_1 T_0 T^{4-\frac{n}{k}-\frac{m}{k}}}{f^{\frac{n}{k}} - c_2^{4-\frac{n}{k}}} a + \frac{n}{k-n} \frac{c_1 T_0^k T^{4-n-m}}{f c_2^{4-n}} b = \sigma T^4 - \frac{3}{4} \sigma T_0 T^3 + \frac{1}{3} \sigma T_0^4$$

According to the theory of dimensional analysis, we have:

$$[T_0 T^3] = [T_0 T^{4-\frac{n}{k}-\frac{m}{k}}]$$

and

$$[T_0^4] = [T_0^k T^{4-n-m}]$$

Therefore we obtain $k = 4$, $m = 3$ and $n = 1$. Filling in the equation that was postulated gives the equivalent temperature:

$$T_{(\lambda)}^4 = \frac{f T^3}{\lambda}$$

The corresponding coefficient of exergy to energy η_u:

$$\eta_u = 1 - \frac{3}{4} \frac{T_0}{T_{(\lambda)}} + \frac{1}{3} \left(\frac{T_0}{T_{(\lambda)}} \right)^4$$

D.1 Carrier Temperature

In the literature, time-resolved photoluminescence experiments reveal the carrier effective temperature by fitting a Boltzmann curve through obtained PL data at a certain timeD.1 [65].

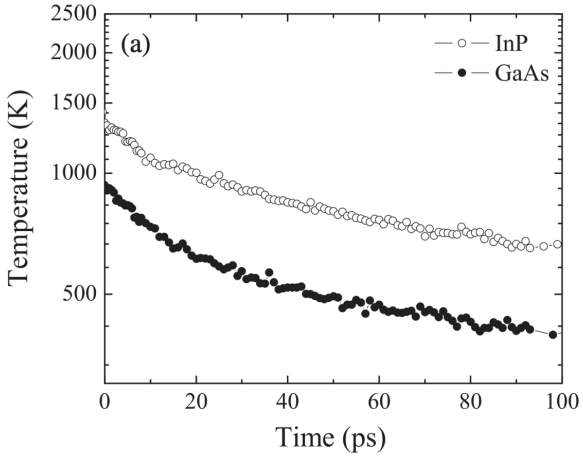

Figure D.1: Carrier temperatures as a function of time after excitation, excited with a 730nm continuous wave laser[65].

Comparing the measured carrier temperature in the figure and the calculated one reveals a higher measured carrier temperature for InP and a lower one for GaAs, showing that the equivalent temperature can not yet fully explain the effective carrier temperatures from the Boltzmann distribution considering different materials. In the experiment performed from figure D.1 the excitation is done with a 720nm continuous wave laser, which excited electrons higher than the bottom of the conduction band (potentially increasing the local ambient temperature). A detailed model can be implemented to calculate the local temperatures due to the locations of the excited electrons in the different energy bands and considering potential different thermalization losses (phonons), however, this is outside the scope of this thesis and can be researched further in the future. The surplus in thermal energy can also be attributed to increased movement of the electrons increasing the resistance in the material.